La investigación reportada en esta tesis es parte de los programas de investigación del CICESE (Centro de Investigación Científica y de Educación Superior de Ensenada, Baja California).
La investigación fue financiada por el CONAHCYT (Consejo Nacional de Humanidades, Ciencias y Tecnologías).

Centro de Investigación Científica y de Educación Superior de Ensenada, Baja California

Doctor of Science in Electronics and Telecommunications with orientation in Instrumentation and Control

Consensus and control of nonlinear systems using fractional calculus and control Lyapunov functions

Thesis

to partially cover the requirements necessary to obtain the degree of

Doctor of Science

Presented by:

Carlos Alberto Rodríguez Martínez

Ensenada, Baja California, México

2024

Tesis defendida por

Carlos Alberto Rodríguez Martínez

y aprobada por el siguiente Comité

Dr. Joaquín Álvarez Gallegos
Director de tesis

Dr. Luis Alejandro Márquez Martínez

Dr. Yury Orlov

Dr. Jonatán Peña Ramírez

Dr. Rafael Castro Linares

Dr. YangQuan Chen

Dra. María del Carmen Maya Sánchez
Coordinadora del Posgrado en Electrónica y Telecomunicaciones

Dra. Ana Denise Re Araujo
Directora de Estudios de Posgrado

Resumen de la tesis que presenta Carlos Alberto Rodríguez Martínez como requisito parcial para la obtención del grado de Doctor en Ciencias en Electrónica y Telecomunicaciones con orientación en Instrumentación y Control.

Consenso y control de sistemas no lineales mediante cálculo fraccionario y funciones de control de Lyapunov

Resumen aprobado por:

Dr. Joaquín Álvarez Gallegos

Director de tesis

Esta tesis presenta un estudio exhaustivo sobre el diseño y la aplicación de estrategias de control avanzadas para diversas aplicaciones. Los objetivos principales abarcan la mejora de las regiones de sincronización para sistemas no lineales de orden fraccionario, la uniformidad de la temperatura superficial mediante el diseño y el control de plataformas térmicas, y el desarrollo de un esquema de control de adaptación de impedancias con un tiempo de convergencia mejorado y una potencia reflejada reducida. Se introduce una novedosa técnica de acoplamiento dinámico de orden fraccionario en dinámica no lineal. Este mecanismo de acoplamiento se analiza rigurosamente para ampliar la región de sincronización de osciladores caóticos de orden fraccionario, permitiendo así una sincronización robusta y mejorada en sistemas complejos conectados en red. Se ha construido una plataforma térmica específica para hacer frente a los problemas de falta de uniformidad de la temperatura superficial. Se ha diseñado un controlador para regular eficazmente la distribución de la temperatura superficial, garantizando la uniformidad en toda la plataforma. La integración de algoritmos de control avanzados en la plataforma térmica mejora la gestión térmica y el rendimiento en diversos escenarios prácticos. Además, la tesis propone una innovadora estrategia de control de la adaptación de impedancias. Este novedoso enfoque de control se centra en lograr una adaptación óptima de la impedancia en distintas condiciones de impedancia de la carga. El diseño hace hincapié tanto en el tiempo de convergencia rápida como en la mitigación de la potencia reflejada. El esquema de control de adaptación de impedancias resultante demuestra un rendimiento superior en términos de velocidad de convergencia y reducción de la potencia reflejada, lo que lo hace adecuado para diversas aplicaciones en electrónica y telecomunicaciones. Las aportaciones de esta tesis ofrecen valiosas perspectivas en el ámbito de la dinámica no lineal, el control térmico y la adaptación de impedancias. Las metodologías propuestas amplían las capacidades de sincronización y control en sistemas complejos y presentan soluciones prácticas para los retos de regulación térmica y adaptación de impedancias. Los resultados de esta investigación tienen potencial para diversas aplicaciones en el mundo real, contribuyendo al avance de la teoría de control y su aplicación en dominios interdisciplinarios.

Palabras clave: Derivadas Fraccionales, Sistemas No Lineales, Sincronización, Gemelos Digitales, Ajuste de Impedancia, Función de Control de Lyapunov

Abstract of the thesis presented by Carlos Alberto Rodríguez Martínez as a partial requirement to obtain the Doctor of Science degree in Electronics and Telecommunications with orientation in Instrumentation and Control.

Consensus and control of nonlinear systems using fractional calculus and control Lyapunov functions

Abstract approved by:

Dr. Joaquín Álvarez Gallegos
Thesis Director

This thesis presents a comprehensive study on designing and implementing advanced control strategies for diverse applications. The primary objectives encompassed enhancing synchronization regions for fractional-order nonlinear systems, making surface temperature uniformity through thermal platform design and control, and developing an impedance-matching control scheme with improved convergence time and reduced reflected power. A novel fractional-order dynamic coupling technique is introduced in nonlinear dynamics. This coupling mechanism is rigorously analyzed to expand the synchronization region of fractional order chaotic oscillators, thereby enabling robust and enhanced synchronization in complex networked systems. A dedicated thermal platform has been constructed to address surface temperature non-uniformity challenges. A controller is designed to efficiently regulate the surface temperature distribution efficiently, ensuring uniformity across the platform. Integrating advanced control algorithms into the thermal platform results in improved thermal management and enhanced performance across various practical scenarios. Furthermore, the thesis proposes an innovative impedance-matching control strategy. This novel control approach focuses on achieving optimal impedance matching across various load impedance conditions. The design emphasizes both rapid convergence time and the mitigation of reflected power. The resultant impedance-matching control scheme demonstrates superior performance in terms of convergence rate and reduced reflected power, making it suitable for various applications in electronics and telecommunications. The contributions of this thesis offer valuable insights into the domain of nonlinear dynamics, thermal control, and impedance matching. The proposed methodologies expand the capabilities of synchronization and control in complex systems and present practical solutions for temperature regulation and impedance matching challenges. The outcomes of this research hold potential for various real-world applications, contributing to the advancement of control theory and its application in interdisciplinary domains.

Keywords: Fractional derivatives, Nonlinear Systems, Synchronization, Digital Twins, Impedance Matching, Control Lyapunov Functions

Dedication

To my parents, Luis, Renecito, and Carlos.

Acknowledgment

The Ensenada Center for Scientific Research and Higher Education, Baja California for opening the doors of the doctoral program in Electronics and Telecommunications to me. Thanks to the National Council for the Humanities, Sciences, and Technologies (CONAHCyT) for giving me financial support to complete my doctoral studies under scholarship number 487088 and to the MESA Lab group of UC Merced. Thanks to my advisor, Professor Joaquín Álvarez Gallegos, and a special mention to Professor Dr. YangQuan Chen. I thank them infinitely for their outstanding dedication, guidance, patience, knowledge, and wisdom all these years and for sharing their passion for the investigation with me. Thanks to professors Luis Alejandro Márquez Martínez, Yury Orlov, Jonatán Peña Ramírez, and Rafael Castro Linares for their suggestions and recommendations during my Ph.D. program. To all members of the MESA Lab, especially Dr. Jairo Viola and Dr. Derek Hollenbeck, who collaborated and helped me during my research stay at UC Merced, to the CICESE administrative staff that made it possible for my stay in the center, and to my Cuban friends in Ensenada, for all the good moments shared. To my parents, whose unwavering belief in me has been the foundation upon which I have built my dreams. Your sacrifices and dedication have shaped me into the person I am today. Your guidance and unconditional love have propelled me through every challenge, and I am eternally grateful for that. To my brothers, for being my partners in laughter, companions in mischief, and a constant source of strength. To my beloved grandmother, for always sharing your smile and happiness no matter what. To my wife, who has always believed in me and has accompanied me all these years, I want to express my deep gratitude for being my unwavering life partner. I have taken every step on this journey with the certainty that you are there. Lastly, to my grandfather and uncles who are not with us, I remember you all the time, and I carry your wisdom and good vibes as a premise in my life.

"The chances you take... the people you meet... the people you love... the faith that you have - that's what's going to define your life. DW"

Contents

Contents

List of figures

Figure | Page

List of figures

List of figures

List of tables

Chapter 1. Introduction to challenging problems on nonlinear systems

Due to their complex interconnections and the difficulty of analyzing them using traditional methods, nonlinear systems present fascinating obstacles in scientific investigation. This research examines some of the intricacies of nonlinear dynamics, in which chaos, thermal diffusion, and stability challenge our comprehension of these systems.

The analysis starts expanding the possibilities of synchronizing fractional-order nonlinear chaotic oscillators, showing a new way to synchronize them by using fractional-order differential equations and their advantage in modeling and improving the dynamic behavior of complex systems. Using a fractional-order system also extends to modeling thermal systems, helping better characterize the physical phenomenon and its control to regulate temperature uniformity. As a final topic, a new methodology to design radio-frequency impedance control systems using Control Lyapunov Functions is presented due to their wide application in telecommunications and semiconductor fabs. The design of these controllers is very complex because of the system's high nonlinear behavior and the need to ensure the required specifications. These require presenting a minimum convergence time and instantaneously reducing the reflected power of the source. This chapter will briefly introduce the study object of this dissertation. First, a review of the state-of-the-art, a thesis overview, and the objective of this research will be presented. Continuously, the publications resulted from the research and, finally, the document outline.

1.1 State of the art

Various interconnection methods have been applied to synchronize dynamical systems, such as linear coupling, where the dynamical systems are interconnected using linear functions, and the coupling term is proportional to the difference in states or some combination of the connected system states. In adaptive coupling, the strength of the interconnection between dynamical systems is adjusted based on the system's states or other system-specific parameters, time-delayed coupling, nonlinear coupling, and others. Although these approaches are effective, they have limitations in specific applications. For example, there are cases where these methods only achieve a synchronous response within narrow ranges or lack robustness to maintain stability in the presence of external disturbances.

Conversely, dynamic interconnections have emerged as an alternative to traditional static approaches. In this scenario, the interaction of the system occurs indirectly through a carefully designed dynamical system Peña Ramirez et al. (2018); Peña Ramirez et al. (2020). This type of synchronization has demonstrated superior performance compared to static couplings, which have proven inadequate. Dynamic interconnection expands the range of coupling strengths for stable synchronous states, enabling systems synchronization that would be challenging with static couplings (Peña Ramirez et al., 2018).

While the study and characterization of synchronization typically involve integer-order operators, there has been growing interest in fractional-order operators in recent years. These fractional-order operators have made significant contributions to the analysis, design, and characterization of synchronization schemes for fractional-order systems (Wang & Wang, 2007; Wang et al., 2018; Muñoz-Pacheco et al., 2020; Yang et al., 2021; Xiong et al., 2021; Wu et al., 2021). The advantage of fractional calculus lies in its ability to model hereditary and memory properties that integer-order modeling cannot fully capture.

Fractional calculus has been extensively explored in nonlinear systems, leading to preliminary insights into fractional systems. Specifically, the use of fractional operators alters the frequency of the system. However, it is essential to note that there are integration-order boundaries beyond which the employing fractional-order derivatives could destabilize the dynamics of a system (Wang & Wang, 2007; Bhalekar & Patil, 2018). Fractional operators fundamentally modify the global behavior of the oscillator, causing alterations in the vector field (Echenausía-Monroy et al., 2021).

Performing precise temperature control is one of the main objectives in the industry due to its relevance in many manufacturing processes such as oil refining (Zhang et al., 2016), food production (Alvino et al., 2018), agriculture (Dik et al., 2018), semiconductors manufacturing (Du et al., 2019) among others. In many cases, thermal processes are multivariable with complex dynamics, challenging their modeling and control. Therefore, its study and analysis are mandatory subjects during the control engineer education process. Part of the control research is focused on developing portable temperature processes as a training platform that represents real industrial temperature control systems.

For this reason, different temperature control training rigs can be used in academia and industry (Viola et al., 2020). These training platforms are not open hardware and software, which limits the possibility of implementing advanced control strategies beyond PI or PID and incorporating additional sensors or control elements for further research and behavior assessment. In addition, most current temperature training platforms are limited to SISO control loops or MIMO systems. This means there is no possibility of working with high-order MIMO systems with coupling and interaction among their control loops.

In the case of multivariate thermal systems, their control is carried out using PID, predictive models, and nonlinear strategies, among others (Su et al., 2020; Chen & Bai, 2021). Similarly, modeling and identifying multivariate thermal systems employ techniques such as spectral analysis, linear models, or machine learning (Pittino et al., 2020; Deng & Li, 2005). Note that in most of the control and identification techniques presented above, the dimensions of the system are used as 2×2 or 3×3. However, an accurate system representation based on the input-output data streams is required for higher-order multivariate thermal systems with more complex analytical models.

Impedance matching is the design of the input impedance of an electrical load or the output impedance of its corresponding signal source to maximize power transfer and minimize the reflected energy of the load. There are two main impedance-matching techniques utilized in the semiconductor industry. One is called an automatic matching network, where physical components, such as passive 'lossless' electrical elements (capacitors and inductors), are used. The second technique is the generator frequency tuning, where the RF frequency at the generator end is varied to reduce the reflected power back to the generator. There are cases where both techniques are used together to obtain a larger window of the tuning space (Zhang & Ordóñez, 2012).

The matching network can be designed using different configurations. The most used architectures are the L (van Bezooijen et al., 2010), Π, and T networks. In the case of the L network, it can provide a unique solution using only two variables: a series capacitor and a shunt capacitor. Therefore, the network can be easily tuned for any feasible load impedance (Thompson & Fidler, 2004).

From 1993, work using different control strategies to solve the impedance matching problem using neural networks, genetic algorithms, deterministic tuning with lookup tables and adaptive systems, and nonlinear control systems (Bacelli. et al., 2007). The matching conditions do not affect the load impedance in these cases. In (Bacelli. et al., 2007), a hierarchical structure controller is composed of a coarser higher-level controller that drives the system close to the matching point and a lower-level feedback controller for fine-tuning. In addition, Firrao (Firrao et al., 2008) used two steps. First, the imaginary part of the load impedance is tuned to (almost) zero using a series (or shunt) reactance; then, the resulting real part is transformed to the target real value with a tunable transformer. Hirose in (Hirose et al., 2009) used a Seek + Follow control for robust behavior using the phase and amplitude of the impedance as reference variables. Adaptive impedance matching is proposed by (van Bezooijen et al., 2010) and presents an overview of adaptive controlled matching networks. Ishida (Ishida et al., 2011) gave the same idea as Hirose but with different conditions and assumed that it knows the exact value of the network components. The results showed a controllable region but did not analyze the impedance region corresponding to the series and shunt capacitor values. A tracking controller is demonstrated in (Li et al., 2019) with initial conditions close to the desired value.

The extremum control is also applied to solve this problem in (Zhang & Ordóñez, 2012). Furthermore, a centralized controller that uses feedback compensation to regulate power and feedforward correction for impairments in the transmission of RF power is presented in (Coumou, 2012, 2013). Finally, the binary search is applied with significant improvement in the convergence time but does not guarantee a monotonic decrease in the reflected power over time (Xiong & Hofmann, 2016; Xiong et al., 2020).

1.2 Thesis overview

The presence of nonlinear systems is everywhere; they are ubiquitous. Consequently, its study is growing and deeply in its knowledge to reveal all its potential in countless applications. Similarly, over the years, the research community has helped find numerous modeling and control tools to achieve better performance every time and solve new challenges. However, at the time of this investigation, some problems, such as fractional-order bidirectional coupling synchronization, consensus of high-order thermal system, and Lyapunov stability analysis of radio-frequency impedance matching, have not yet been solved. The main goal of this research is to provide appropriate solutions to the problems mentioned above.

Synchronization is an emerging physical phenomenon caused by the interaction of two or more dynamic entities that permeate the natural world. For the case of integer-order systems, there exists a vast and mature literature where we can find different interconnection schemes for synchronizing dynamic systems, for example, master-slave synchronization scheme, adaptive synchronization, synchronization based on state observers, and so on. Although each of these strategies is effective, there are limitations in their applications; e.g., there are cases where these schemes have marginal ranges for which the synchronous response is achieved, or they exhibit poor robustness to maintain a stable synchronous state under the influence of external disturbances. This is one of the reasons why dynamic interconnections have emerged as an alternative to classical static schemes. In this case, the agent interaction is achieved indirectly through a suitably designed dynamic coupling. In particular, dynamic coupling increases the intervals of coupling strength values for which it is possible to achieve a synchronized behavior, and it may also be possible to synchronize systems that cannot be done with static coupling. Moreover, fractional calculus has been studied extensively in nonlinear systems, with notable contributions related to synchronization in fractional-order systems. However, so far, the use of dynamic couplings in the context of fractional-order systems seems to be unexplored.

In another topic, thermal processes are one of the most common systems in the industry, making their understanding a mandatory skill for control engineers. Therefore, multiple efforts are focused on developing low-cost and portable experimental training rigs recreating the thermal process dynamics and controls, usually limited to Single-Input Single-Output (SISO) or low-order 2x2 Multiple-Input Multiple-Output (MIMO) systems. However, many of these platforms are expensive, require laboratory arrangements, and have more prolonged heating and cooling response times, which is inefficient for teaching and training. The Peltier module, which operates based on the Peltier effect, emerges as a solution to reduce these slow cycles and delivers a precise temperature. In addition, its durability and low cost make the Peltier module a suitable solution in systems where temperature control is crucial. Consequently, the number of researchers modeling these modules is increasing faster to improve their efficiency and expand their applications. They can be used, for example, to transport anything that requires strict temperature control, to generate electricity from heat transfer, etc.

Combined with the mentioned scenarios, power efficiency is one of the most critical challenges in the 21st century. Since the repercussions of oil derivatives on climate change, big industries are pushing the boundaries of efficiency and migration to a more electric world. That requires optimal power transfer to reduce losses and optimize electricity use. To guarantee this process, impedance matching is the key to helping transfer the greatest amount of power from the source to the load. Today, many strategies emerge to solve the impedance matching control efficiently and fast enough to minimize the reflected power produced as a consequence of mismatching in the networks on a large scale. There are numerous applications, from the antenna adjustment of smartphones to the plasma etching or deposition process where the chips are made. However, according to industry experts and researchers, there are still problems to solve, such as desirable behavior in the reflected power, the optimal path of the capacitors used to compensate for the mismatches in the network, and the robustness against parameter variation. Some of them are analyzed in this work, and several solutions are presented.

1.3 Objective

The primary objective of this thesis is to investigate and demonstrate the efficacy of employing fractional-order systems and control Lyapunov functions to address nonlinear system problems. Specifically, the research will focus on developing a novel methodology for a radio frequency impedance matching controller, marking a before and after. The objective includes analyzing, designing, and implementing controllers to provide robust and efficient solutions for various nonlinear systems, thus providing insights that facilitate the development of innovative control strategies capable of handling complex nonlinear dynamics in engineering applications.

1.3.1 Specific objectives

- Design a fractional-order dynamic coupling for representative nonlinear systems.
- Conduct numerical simulations to validate the effectiveness of the proposed controllers in stabilizing and controlling nonlinear systems.
- Investigate the impact of a fractional-order model and a data-driven identification technique on modeling a Peltier thermal platform.
- Develop a theoretical framework for modeling and controlling RF impedance matching networks based on Control Lyapunov functions.
- Design a benchmark for study and design impedance matching controllers for plasma processes.

1.4 Publications

Journals

- Carlos Rodriguez, Jairo Viola, YangQuan Chen, Joaquin Alvarez, "Modeling and control of L-type network impedance matching for semiconductor plasma etch", J. Vac. Sci. Technol. B, March 2024, 42 (2): 022212. `https://doi.org/10.1116/6.0003444`
- J. L. Echenausía-Monroy, C. A. Rodríguez-Martínez, L. J. Ontañón-García, J. Alvarez, J. Pena Ramirez, "Synchronization in Dynamically Coupled Fractional-Order Chaotic Systems: Studying the Effects of Fractional Derivatives", Complexity, vol. 2021, Article ID 7242253, 12 pages, 2021. `https://doi.org/10.1155/2021/7242253`

Book Chapter

- Viola, Jairo, Rodriguez, Carlos, Hollenbeck, Derek and Chen, YangQuan, "13 A radio frequency impedance matching control benchmark and optimal fractional-order stochastic extremum seeking method", Outliers in Control Engineering: Fractional Calculus Perspective, edited by Paweł D. Domański, YangQuan Chen and Maciej Ławryńczuk, Berlin, Boston: De Gruyter, 2022, pp. 237-258. `https://doi.org/10.1515/9783110729122-013`

Proceedings

- C. Rodriguez, J. Viola, J. Alvarez and Y. Chen, “Global Monotonic Radio-Frequency Impedance Matching Via Control Lyapunov Function Under Safety Constraints,” 2022 IEEE 61st Conference on Decision and Control (CDC), Cancun, Mexico, 2022, pp. 511-517. `https://doi.org/10.1109/CDC51059.2022.9992500`

- C. Rodriguez, J. Viola, J. Alvarez and Y. Chen, “Radio Frequency Impedance Matching Based on Control Lyapunov Function,” 2022 American Control Conference (ACC), Atlanta, GA, USA, 2022, pp. 2253-2258. `https://doi.org/10.23919/ACC53348.2022.9867175`

- C. Rodriguez, J. Viola, Y. Chen, "Data-Driven Modeling for a High-Order Multivariable Thermal System and Control," IFAC-PapersOnLine 54 (20), 753–758. `https://doi.org/10.1016/j.ifacol.2021.11.262`

- J. Viola, D. Hollenbeck, C. Rodriguez and Y. Chen, “Fractional-Order Stochastic Extremum Seeking Control with Dithering Noise for Plasma Impedance Matching,” 2021 IEEE Conference on Control Technology and Applications (CCTA), San Diego, CA, USA, 2021, pp. 247-252. `https://doi.org/10.1109/CCTA48906.2021.9658616`

- Rodríguez, CA, Viola, J, Chen, Y. “An Radio Frequency Impedance Matching Control Benchmark System for Advanced Control Strategies Evaluation,” Proceedings of the ASME 2021 International Design Engineering Technical Conferences and Computers and Information in Engineering Conference. Volume 7: 17th IEEE/ASME International Conference on Mechatronic and Embedded Systems and Applications (MESA). Virtual, Online. August 17–19, 2021. V007T07A004. ASME. `https://doi.org/10.1115/DETC2021-70211`

- J. Viola, C. Rodriguez and Y. Chen, “PHELP: Pixel Heating Experiment Learning Platform for Education and Research on IAI-based Smart Control Engineering,” 2020 2nd International Conference on Industrial Artificial Intelligence (IAI), Shenyang, China, 2020, pp. 1-6. `https://doi.org/10.1109/IAI50351.2020.9262160`

Awards

- Best Outstanding Student paper award at CCTA 2021 on the paper, "Fractional-order stochastic extremum seeking control with dithering noise for plasma impedance matching."

- 10th Nomination at Topcoder: EdgeX Foundry(TM) Ideation Challenge, 2020 edition, "PHELP: Peltier Heating Experimental Learning Platform. An Edge Computing IoT system for Control Systems education."

1.5 Organization of the thesis

This thesis work is organized as follows: Chapter 2 introduces the synchronization of nonlinear systems with a fractional-order coupling design. Chapter 3 presents a novel multi-input, multi-output thermal system, covering its design, modeling, and control. Chapter 4 addresses impedance matching challenges and outlines control strategies to improve previously identified issues. Finally, Chapter 5 summarizes the main conclusions drawn from the thesis, providing insight and discussing potential directions for future research.

Chapter 2. Synchronization of fractional order nonlinear systems

2.1 Introduction

Synchronization is a topic widely studied by the research community since this phenomenon was observed and described as early as the seventeenth century by Christiaan Huygens, (Pikovsky et al., 2001). Years later, with the boom of fractional calculus in the control systems field, the analysis of this phenomenon was extended to fractional-order (FO) nonlinear systems. This new approach brings more advantages to the control and stability of nonlinear systems. In this chapter, the state-of-the-art and some results are presented to demonstrate the superiority of fractional-order differential equations in the synchronization of nonlinear systems.

2.2 Synchronization of nonlinear systems

The study of nonlinear dynamics has been an active area of research since the 1960s. Since most natural processes are nonlinear, it is no wonder that nonlinear differential equations arise abundantly in theoretical descriptions of physical, chemical, biological, and engineering problems and population dynamics, economics, and social dynamics (Lakshmanan, 2005).

There are "essentially nonlinear phenomena" that can take place only in the presence of nonlinearity. Some examples are as follows:

- Finite escape time;
- Multiple isolated equilibria;
- Limit cycles;
- Subharmonic, harmonic, or almost-periodic oscillations;
- Chaos;
- Multiple modes of behavior.

This chapter will focus on systems with the presence of chaos. The limit cycle is the oscillation of fixed amplitude and frequency of nonlinear systems irrespective of the initial conditions, and the chaos is the presence of more complicated steady-state behavior that is not equilibrium, periodic oscillation, or almost-periodic oscillation. Some of these chaotic motions exhibit randomness despite the deterministic nature of the system.

The notion of self-sustained oscillators was introduced by Andronov in 1937. In the 1930s, only periodic self-oscillations were known. Nowadays, irregular or chaotic self-sustained oscillators are also studied. One of the most significant achievements of nonlinear dynamics within the last few decades was the discovery of complex, chaotic motion in relatively simple oscillators. The term "chaotic" means that the long-term behavior of a dynamical system cannot be predicted even if there are no natural fluctuations in the system parameters or the influence of a noisy environment.

For the self-sustained oscillator, H. Poincaré introduced the notion of the limit cycle, Figure 1, which is a consequence of a simple attractor in the dynamical system. Examples are the Van der Pol oscillator, the negative resistance oscillator, and the Wien-bridge oscillator.

Complex structures with chaotic behavior are called strange attractors, Figure 2 (in contrast to limit cycles that are simple attractors). The Lorenz, Rössler, and Chua oscillators are some of them.

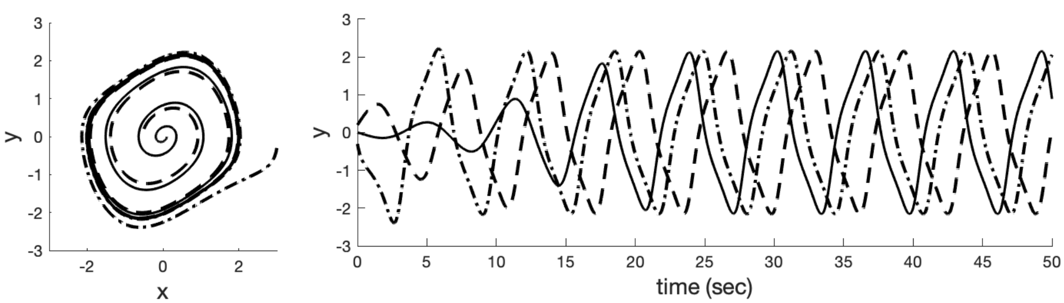

Figure 1. Dynamic of a self-sustained oscillator.

The dynamics of a chaotic system are sensitive to small perturbations of initial conditions. If we take two close but different points in the phase space and follow their evolution, we see that the two-phase trajectories starting from these points eventually diverge. Even if we know the state of a chaotic oscillator with a very high but finite precision, we can predict its future only for a finite time interval, depending on the precision, and we cannot predict its state for longer times. The sensitivity pertains to any point of the trajectory. This means that all motions on the strange attractor are unstable. Quantitatively, the instability is measured with the largest Lyapunov exponent,

$$\lambda \simeq \frac{1}{t} \ln \frac{|\delta x(t)|}{|\delta x(0)|}, \tag{1}$$

and the inverse of this exponent is the characteristic time of instability.

Synchronization among self-excited oscillators has long been studied. A search of the publications on this topic revealed an amount of over 900 papers since 1952, with an average of 721.53 citations per year. Besides several publications, some issues remain unresolved, especially in synchronizing chaotic oscillators.

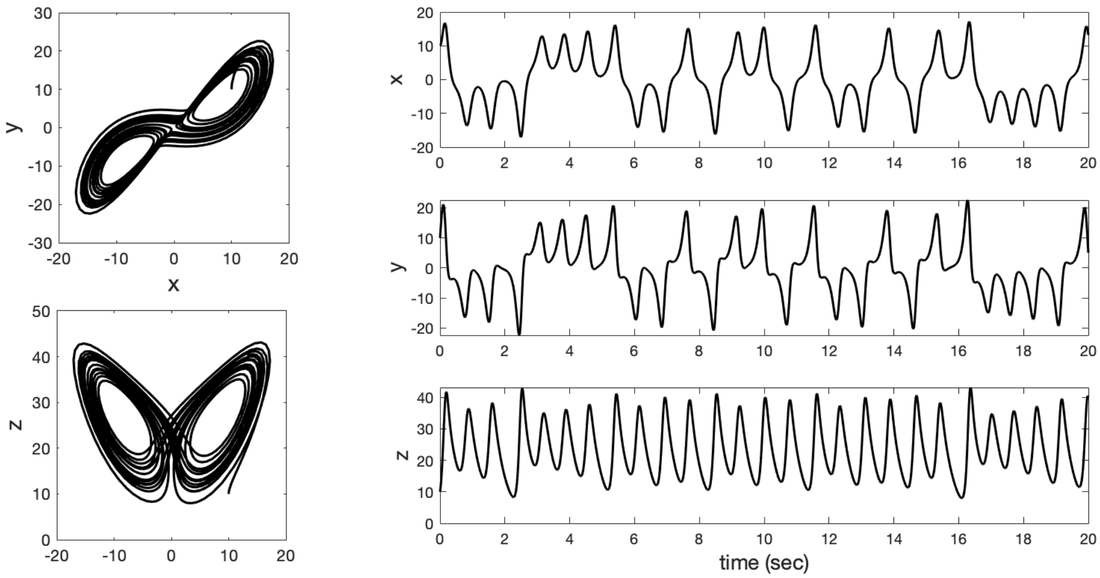

Figure 2. Dynamic of a chaotic self-sustained oscillator.

Synchronization can be understood as adjusting the rhythms of oscillating objects due to their weak interaction. In physics, oscillatory objects are denoted self-sustained oscillators. This oscillator is an active system with an internal energy source transformed into oscillatory movement.

According to (Blekhman et al., 1997), a more general definition is that synchronization may be defined as the mutual time conformity of two or more processes. This conformity can be characterized by the appearance of certain relations between some functionals or functions depending on the processes. Furthermore, based on the type of interconnections (interactions) in the system, different kinds of synchronization can be defined:

- In the case of disconnected systems that present synchronous behavior, this is referred to as *natural synchronization*, e.g., all precise clocks are synchronized in the frequency domain. The synchronization surges exponentially by a natural interaction between the systems, not by an action or force.
- When proper interconnections in the systems achieve synchronization, that is, without any artificially introduced external action, the system is referred to as *self-synchronized*. A classic example

of self-synchronization is the pair of pendulum clocks hanging from a lightweight beam reported by (Huygens, 1673).

- When external actions (input controls) and/or artificial interconnections exist, the system is called *controlled-synchronized*. Examples of this case are most practical applications of synchronization theory, such as transmitter-receiver systems.

Depending on the formulation of the controlled synchronization problem, a distinction should be made between internal (mutual) synchronization and external synchronization. In the first and most general case, all synchronized objects occur on equal terms in the unified multi-composed system. Therefore, the synchronous motion occurs because of the interaction of all system elements. This configuration corresponds to the well-known bidirectional coupling.

In the second case (unidirectional coupling), one object in the multicomposed system is supposed to be more powerful than the others, and its motion can be considered independent of the motion of the others. Thus, this dominant separate system predetermined the resulting synchronous motion, e.g., master-slave systems.

From the control point of view, the controlled synchronization problem is the most interesting: how to design a controller and/or interconnections that guarantee synchronization of the multicomposed system concerning a specific desired functional.

In (Pecora & Carroll, 1990), they presented the synchronization in chaotic systems, setting the starting point of this exciting research topic. Then (Brown et al., 1994) analyzed the effect of additive noise and drift in synchronizing these systems. Years later, (Pecora et al., 1997) presented the fundamentals of synchronization in chaotic systems and applications, highlighted the role of this system for secure communications, and (Nijmeijer, 2001) addressed the synchronization problem from a control theory perspective. Besides existing nonlinear self-sustained oscillators, chaotic oscillators have gained more attention in the literature due to their applications and capabilities in the communications field. The number of control strategies applied to the synchronization of a chaotic system is vast, starting from **Adaptive Control** (Pogromsky, 2002; Feki, 2003; Yu & Zhang, 2004; Park, 2005; Adloo & Roopaei, 2011; Jeong et al., 2013), **Sliding Mode Control** (Zhang et al., 2006; Chen et al., 2017; Kharabian & Mirinejad, 2021), **Active Control** (Yassen, 2005; Liu, 2008; Zheng & Zhang, 2018), **PID Control** (Femat & Solis-Perales, 2008; Martínez-Guerra et al., 2015), to mention a few.

With the applications of fractional calculus to physics and engineering, most of the chaotic dynamical systems based on integer-order calculus have been extended to the fractional-order domain to fit the experimental data much more precisely than integer-order modeling. Many authors have begun to investigate the chaotic dynamics of fractional-order dynamical systems (Razminia et al., 2011; Petráš, 2006; He & Chen, 2017; Deng et al., 2009; Azar et al., 2017; Alomari, 2011; Tavazoei & Haeri, 2008a; Martínez-Guerra et al., 2015; Lu, 2006). Results have shown that the fractional-order Chua's system of order as low as 2.7 can produce a chaotic attractor, a nonautonomous Duffing system of the order less than two can still behave chaotically, chaos and hyperchaos in the fractional-order Rössler with the order as low as 2.4, hyperchaos exists with order as low as 3.8, and chaotic behavior and its control in the fractional-order Chen system.

In consequence, the synchronization of fractional-order chaotic systems started to be studied. The first work appears to be (Li et al., 2003), looking at the master-slave synchronization of fractional-order Chua's and Rösler chaotic oscillators with a static coupling. Later, other works continue the research on synchronization in a fractional-order system; some of them are (Lu, 2005; Xin Gao & Juebang Yu, 2005; Tarasov & Zaslavsky, 2006; Peng, 2007; Tavazoei & Haeri, 2008b; Odibat et al., 2010; Ping et al., 2010; Martínez-Martínez et al., 2011; Rajagopal et al., 2017; Martínez-Guerra & Pérez-Pinacho, 2018; Edelman et al., 2018).

However, the use of dynamic couplings in the context of fractional-order systems seems to have been unexplored so far. Consequently, we present a fractional-order synchronization scheme based on dynamic coupling in the next section.

2.3 Synchronization of fractional order chaotic oscillators with dynamic coupling

The chaotic dynamics of fractional-order systems attracted the scientific community's interest years ago, associated with advances in numerical methods to solve fractional-order systems and their electronic implementations (Caponetto et al., 2010). Therefore, most chaotic dynamical systems based on integer-order calculus have been extended into the fractional-order domain to fit the experimental data more precisely than the integer-order modeling (Azar et al., 2017).

The most important types of synchronization are Complete, Phase, Lag, and Generalized synchronization. Complete synchronization occurs if the states of both systems coincide and vary chaotically in time. This is achieved by coupling both systems with the differences of the states in the corresponding dynamics.

Phase synchronization means that, in some way, the oscillator phase becomes modified to follow the phase of a force. The general way to see this is as explained below. Assume the dynamics

$$\dot{x} = f(x) + p(t) \tag{2}$$

where $f(x)$ contains the dynamics of the chaotic oscillator, and $p(t)$ is a periodic oscillator. The idea is that the complete system remains chaotic. Still, its dynamics become modified so that the phase of the chaotic attractor meets that of the applied force (periodic oscillator).

It has been demonstrated that there exists a regime of Lag synchronization in which the states of two oscillators are nearly identical, but one system lags in time behind the other. For intermediate coupling strengths, the states of two interacting systems almost coincide if one is shifted in time $x_1(t) \approx x_2(t-\tau)$. With a further increase in coupling, the time shift decreases, and the regime tends to complete synchronization.

Generalized synchronization (GS) can be interpreted as suppression of the driving system's dynamics by the driving one so that the slave system follows its master. Consider two nonlinear systems in a master-slave configuration through which the master system is given by

$$\begin{aligned} \dot{x}_m &= F_m\left(x_m\right)) \\ y_m &= h_m(x_m) \end{aligned} \tag{3}$$

and the slave by

$$\begin{aligned} \dot{x}_s &= F_s\left(x_s, u_s\left(x_s, y_m\right)\right) \\ y_s &= h_s(x_s) \end{aligned} \tag{4}$$

where $x_s = (x_{1_s}, \ldots, x_{n_s}) \in \mathbb{R}^{n_s}, x_m = (x_{1_m}, \ldots, x_{n_m}) \in \mathbb{R}^{n_m}, h_s : \mathbb{R}^{n_s} \to \mathbb{R},\ h_m : \mathbb{R}^{n_m} \to \mathbb{R}, u_m = (u_{1_m}, \ldots, u_{m_m}) \in \mathbb{R}^{m_m}, u_s : \mathbb{R}^{n_s} \times \mathbb{R} \to \mathbb{R}, y_m, y_s \in \mathbb{R}, F_s,\ F_m, h_s, h_m$ are assumed to be polynomial in their arguments.

Definition 2.1 ((Martínez-Guerra et al., 2015)) *Slave and master systems are said to be in the GS state if there exists a differential primitive element that generates a transformation $H_{m_s} : \mathbb{R}^{n_s} \to \mathbb{R}^{n_m}$ with $H_{m_s} = \Phi_m^{-1} \circ \Phi_s$ and an algebraic manifold $M = \left\{(x_s, x_m) \mid x_m = H_{m_s(x_s)}\right\}$ together with a compact set $B \subset \mathbb{R}^{n_m} \times \mathbb{R}^{n_s}$ with $M \subset B$ such that their trajectories with initial conditions in B approach M as $t \to \infty$.*

Following, we analyze the type of bidirectional synchronization of a dynamically coupled classical fractional-order chaotic system, Table 1. The synchronization in unidirectional coupled mode was presented by (Echenausía-Monroy et al., 2021).

2.3.1 Fractional calculus

Fractional calculus is a branch of mathematical analysis that explores differentiation and integration with non-integer orders, as defined by (Castillo, 2010). Similarly to many other mathematical fields, its origins lie in the generalization or extension of existing concepts. This extension involves considering the meaning of $\frac{d^n}{dx^n}$ when n is fractional, irrational, or complex, or the corresponding integration n times. The inception of fractional calculus dates back to September 30th, 1695; later in the 18th century, Euler referenced it while investigating the interpolation of derivatives with integer orders, followed by Lagrange in 1772. Subsequently, Liouville and Riemann developed formulas for integrals and derivatives of arbitrary order by extending a Taylor series.

Table 1. Equations of the systems and attractor diagrams

Chua's system	Rössler system	Lorenz system
$\mathcal{D}^{q_1}x = \alpha\left(y - x - h(x)\right)$	$\mathcal{D}^{q_1}x = -(y+z)$	$\mathcal{D}^{q_1}x = \sigma\left(y - x\right)$
$\mathcal{D}^{q_2}y = x - y + z$	$\mathcal{D}^{q_2}y = x + ay$	$\mathcal{D}^{q_2}y = \gamma x - xz - y$
$\mathcal{D}^{q_3}z = -\beta y - \gamma z$	$\mathcal{D}^{q_3}z = z\left(x - c\right) + b$	$\mathcal{D}^{q_3}z = xy - \beta z$
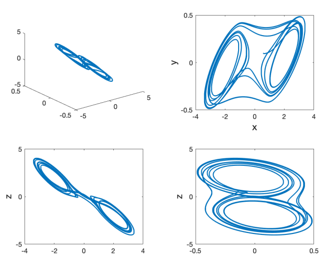	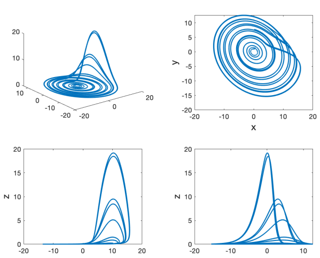	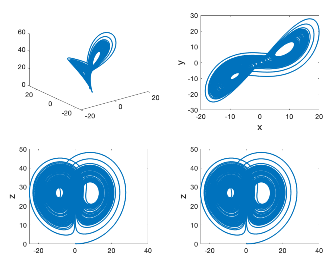

with $h(x) = bx + 0.5(a-b)\left[|x+1| - |x-1|\right]$

These formulations were combined into what is now known as the Riemann-Liouville fractional integral formula. Once the integral was established, the fractional derivative was derived through sequential operations. In 1867, (Grünwald, 1867) introduced a novel approximation for the fractional derivative, later proved by (Letnikov, 1868). This formula is recognized today as the Grünwald-Letnikov fractional derivative formula. The resulting expression is valuable for approximating fractional integrals, allowing negative values of the operation order. During the twentieth century, alternative definitions of fractional integrals and derivatives have emerged, the Caputo formulation being the most widely used (Caputo, 1967). The Caputo fractional derivative has recently gained significance in control theory compared to the Grünwald-Letnikov definition since the latter's Laplace transform introduces initial conditions lacking physical interpretation (Castillo, 2010). However, (Khalil et al., 2014) proposed a new definition for the fractional derivative to extend the properties of integer order derivatives, such as product, quotient, and chain rule, among others.

2.3.1.1 Definitions

Currently, there exist more than ten different definitions for fractional-order integrals and differentiations Miller & Ross (1993). For the convenience of the readers, a few frequently used definitions are briefly outlined here. More information can be found in (Magin, 2006).

1. **Riemann-Liouville definition of FO integration**

   The Riemann-Liouville (R-L) definition of fractional-order integration is:

$$
{}_0D_t^{-\alpha} f(t) = \frac{1}{\Gamma(\alpha)} \int_0^t \frac{f(\tau)}{(t-\tau)^{1-\alpha}} d\tau, \tag{5}
$$

   where $0 < \alpha < 1$, and $\Gamma(x)$ is the Gamma function $\Gamma(x) = \int_0^\infty e^{-u} u^{x-1} du$.

2. **Riemann-Liouville definition of FO differentiation**

   The R-L definition of fractional-order differentiation is based on the fractional integral and ordinary derivatives: ${}_0D_t^{\alpha} f(t) = \frac{d}{dt}\left[{}_0D_t^{-(1-\alpha)} f(t)\right]$. More specifically, there are left R-L and right R-L definitions for FO differentiation by distinguishing the lower and upper limits of the integration,

$$
{}_aD_t^{\alpha} f(t) = \frac{1}{\Gamma(n-\alpha)} \left(\frac{d}{dt}\right)^n \int_a^t (t-\tau)^{n-\alpha-1} f(\tau) d\tau \tag{6}
$$

$$
{}_tD_b^{\alpha} f(t) = \frac{1}{\Gamma(n-\alpha)} \left(-\frac{d}{dt}\right)^n \int_t^b (t-\tau)^{n-\alpha-1} f(\tau) d\tau \tag{7}
$$

3. **Caputo definition of FO differentiation**

   The Caputo definition of fractional-order differentiation takes the integer order differentiation of the function first and then takes a fractional-order integration:

$$
{}_0^C D_t^{\alpha} f(t) = \frac{1}{\Gamma(1-\alpha)} \int_0^t \frac{f'(\tau)}{(t-\tau)^{\alpha}} d\tau. \tag{8}
$$

4. **Grünwald-Letnikov definition**

   The Grünwald-Letnikov (G-L) definition defines the fractional integration and differentiations in a unified way:

$$ {}_aD_t^{\alpha} f(t) = \lim_{h \to 0} \frac{1}{h^{\alpha}} \sum_{j=0}^{[(t-a)/h]} (-1)^j \begin{pmatrix} \alpha \\ j \end{pmatrix} f(t - jh) \tag{9} $$

2.3.1.2 Fractional order differential equations

Fractional order differential equations (FODEs) form the basis for characterizing fractional-order dynamic systems. All analyses of fractional-order systems, whether in the time domain, s-domain, or complex frequency domain, rely on FODEs as their fundamental framework. Fractional versions of typical differential equations are linear,

$$ \begin{aligned} & a_1 D^{\alpha_1} y(t) + a_2 D^{\alpha_2} y(t) + \cdots + a_n D^{\alpha_n} y(t) \\ =& b_1 D^{\beta_1} u(t) + b_2 D^{\beta_2} u(t) + \cdots + b_m D^{\beta_m} u(t), \end{aligned} \tag{10} $$

where the orders, α_i , $\beta_j (i, j = 1, 2, \dots)$, can be arbitrary real numbers, i.e., α_i , $\beta_j \in \mathbb{R}$. If α_i and β_j are integer multiples of a common factor, the equation has a commensurate order and is non-commensurate if no common factor exists. Generally, it considers the following incommensurate fractional-order nonlinear system in the form:

$$ \begin{aligned} {}_0D_t^{q_i} x_i(t) &= f_i \left(x_1(t), x_2(t), \dots, x_n(t), t \right) \\ x_i(0) &= c_i, \quad i = 1, 2, \dots, n, \end{aligned} \tag{11} $$

where c_i are initial conditions, or in its vector representation:

$$ D^q x = f(x), \tag{12} $$

where $q = [q_1, q_2, \dots, q_n]^T$ for $0 < q_i < 2$, $(i = 1, 2, \dots, n)$ and $x \in \mathbb{R}^n$, and finally fractional-order partial differential equations as the generalized anomalous diffusion equation

$$ {}_tD_*^{\beta} u(x, t) = {}_x D_{\theta}^{\alpha} u(x, t), \qquad -\infty < x < +\infty, \qquad t \geq 0, \tag{13} $$

where ${}_xD_{\theta}^{\alpha}$ is the Riesz-Feller fractional derivative, $0 < \alpha < 2$, $\beta = 1$ refers to the strictly space fractional diffusion, $\alpha = 2$, $0 < \beta < 1$ refers to the strictly time fractional diffusion, and $0 < \alpha < 2$, $0 < \beta < 1$ refers to the strictly space-time fractional diffusion.

Numerous contemporary control ideas and techniques remain relevant for dynamic systems that exhibit FO behaviors. The state-space (S-S) representation is a potent tool in this regard. When a system with commensurate order is considered, it can typically be represented by the definition of suitable state variables.

$$
\begin{aligned}
{}_0D_t^{\alpha}x(t) &= f(x,u,t) \\
y(t) &= g(x)
\end{aligned} \tag{14}
$$

where $x \in \mathbb{R}$ n is the state vector of dimension n, and $0 < \alpha < 2$ is the common factor of the differentiation orders. For linear FODEs, the above equation can be expressed as

$$
\begin{aligned}
{}_0D_t^{\alpha}x(t) &= Ax(t) + Bu(t) \\
y(t) &= Cx(t)
\end{aligned} \tag{15}
$$

where A, B, and C are system, input, and output matrices, respectively.

The synchronization of nonlinear fractional-order chaotic systems under bidirectional coupling will be carried out in the next section, and the stability criteria will be used to ensure the general synchronization performance.

2.3.2 Synchronization under bidirectional coupling

The bidirectional coupled of two fractional-order systems is described by the set of equations

$$
\begin{aligned}
\mathcal{D}^q x_m &= F(x_m) + B_1 h, \\
\mathcal{D}^q x_s &= F(x_s) - B_2 h, \\
\mathcal{D}^q h &= Gh - kB_3(x_m - x_s),
\end{aligned} \tag{16}
$$

where $x_m, x_s \in \mathbb{R}^n$ represent the state vectors of both the master and slave systems, $h = (h_1, h_2)^T$ for $h_i \in \mathbb{R}, i = 1, 2$ are the state variables of the dynamic coupling, see Figure 3. The vector field F is assumed to be smooth enough, linear or nonlinear, and the coupling force between the systems is denoted by k. Otherwise, the design of a dynamic coupling involves two coupling matrices, denoted $B_1, B_2 \in \mathbb{R}^{n\times 2}$ and $B_3 \in \mathbb{R}^{2\times n}$. These matrices are generated under the premise that only one of the elements of each of these matrices is equal to 1, and the other entries are zero, which means that the coupling is applied only in one state variable of the slave system and that the coupling considers only one measured variable.

The matrix G from (16) is given by

$$
G = \begin{pmatrix} -\alpha_c & 1 \\ -\gamma_1 & -\gamma_2 \end{pmatrix}, \tag{17}
$$

where γ_1, γ_2 and α_c are design parameters of the dynamical coupling. The following definition is given to address asymptotic synchronization.

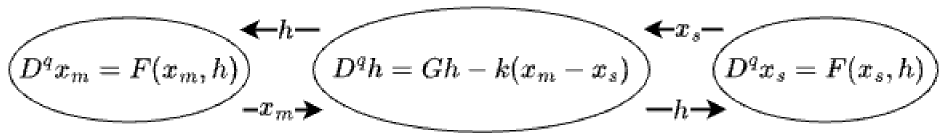

Figure 3. Schematic representation of bidirectional coupled fractional-order systems interacting via fractional-order dynamic coupling

Definition 2.2 *The coupled systems* (16) *are said to be asymptotically synchronized if*

$$\lim_{t\to\infty} |x_m - x_s| = 0, \quad \lim_{t\to\infty} h = 0. \tag{18}$$

2.3.2.1 Local stability analysis

Definition 2.3 *Let us consider the general fractional-order system of n dimensions given by* (19)*, in which the roots of $f(X) = 0$ are the equilibrium points. In this case, $D^q(X) = (D^q x_1, D^q x_2, \ldots, D^q x_n)^T$, $X = (x_1, x_2, \ldots, x_n)^T \in \mathrm{R}^n$.*

$$D^q(X) = f(X) \tag{19}$$

Theorem 2.1 *A commensurable fractional-order system modeled by three state variables $n = 3$ is asymptotically stable at the equilibrium point equal to 0, if and only if $|\arg(\lambda_i(J))| > q\pi/2$, $i = 1, 2, 3$. In this case J denotes the Jacobian matrix of $f(X)$, and λ_i are the eigenvalues of J, (Podlubny, 1999).*

Theorem 2.2 *The equilibrium point O of a dynamical system described by* (19) *is unstable if and only if the order of q satisfies the condition imposed by* (20)*, for at least one eigenvalue, where $\mathrm{Re}(\lambda)$ and $\mathrm{Im}(\lambda)$ denote the real and imaginary parts of λ.*

$$q > \frac{2}{\pi} \arctan \frac{|\,\mathrm{Im}(\lambda)\,|}{|\,\mathrm{Re}(\lambda)|} \tag{20}$$

Theorem 2.3 *For $n = 3$, if one of the eigenvalues $\lambda_1 < 0$ and the other two complex conjugated $|\arg(\lambda_2)| = |\arg(\lambda_3)| < q\pi/2$, then the equilibrium point O is called the saddle point of index 2. If one of the eigenvalues $\lambda_1 > 0$ and the other two complex conjugated $|\arg(\lambda_2)| = |\arg(\lambda_3)| > q\pi/2$, then the equilibrium point O is called the saddle point of index 1, (Deng & Lü, 2007).*

To analyze the stability of the synchronous solution defined at (18), it is assumed that the function F in (16) can be written as the sum of linear and nonlinear components,

$$F(x_i) = Px_i + E(x_i) \tag{21}$$

where $P \in \mathbb{R}^{n\times n}$ is a constant matrix and $E(x_i) \in \mathbb{R}^n$ is a vector containing nonlinear terms.

The synchronization error is $e_p := (x_m - x_s, h)^T$. The state h of the dynamic coupling is included in the error definition because the parameters of the dynamic coupling should be chosen so that, when the system synchronizes, the coupling vanishes. Then, replacing (21) with (16) and computing the corresponding dynamics of the synchronization error, we obtain the following.

$$\mathcal{D}^q e_p = \tilde{A} e_p + g_p(t, e_p), \tag{22}$$

where

$$\tilde{A} = \begin{bmatrix} P & B_2 + B_1 \\ -kB_3 & G \end{bmatrix}, \quad g_p(t, e_p) = \begin{bmatrix} E(x_m) - E(x_s) \\ \mathcal{O} \end{bmatrix}, \tag{23}$$

where $\mathcal{O} = (0, 0)^T$. Furthermore, note that the term $g_p(t, e_p)$ is a vanishing perturbation (Khalil, 2015) because $g_p(t, 0) = 0$. Then, the stability properties of the system (22) are fully determined by the eigenvalues of matrix $\tilde{A}$. Then, by the stability analysis of commensurate fractional-order time-invariant systems, we see that the synchronization error dynamics (22) is locally asymptotically stable if

$$|\arg(\lambda_j)| > \frac{q\pi}{2}\ ,\ \forall j = 1, 2, \ldots, n. \tag{24}$$

Thus, if it is possible to find values of k, γ_1, γ_2, and α_c such that the above condition is satisfied, then the coupled systems described by (16) will achieve complete synchronization, according to the definition (2.2).

In the case of a commensurate fractional-order system, (24) is satisfied. However, if the order of the fractional-order system is non-commensurate, the stability condition is

$$|\arg(\lambda_j)| > \frac{\pi}{2M}\ ,\ \forall j = 1, 2, \ldots, n. \tag{25}$$

where $q_1 \neq q_2 \neq \ldots \neq q_n$, with $q_i = n_i/d_i$ and gcd$(n_i, d_i) = 1$. Let M be the lowest common multiple of the denominators d_i's.

The algorithm used in this thesis to approach the solution of fractional-order chaotic oscillators is given in Algorithm 1, for the predictor-corrector Adams-Bashforth-Moulton method. This numerical method was implemented by (Garrappa, 2018) and is available at Matlab File Exchange to simulate the dynamics of the fractional-order systems with commensurate fractional-order.

Algorithm 1 Predictor-Corrector Adams-Bashforth-Moulton Algorithm

Require: f, q, y_0, T, T_0 and h
Output Variables
y an array of $m \times N + 1$ real numbers that contain the approximate solutions
t an array of $N + 1$ real numbers that contain the solution from $T_0 \rightarrow T$ with an increase of h
Internal Variables
m the number of initial conditions
N the number of time steps that the algorithm is to consider
i, j variables used as indexes
a, b arrays of $m \times N + 1$ real numbers that contain the values of the corrector and predictor, respectively
p the predicted value
$N = floor\left(\left(T - T_0\right)/h\right)$
$m = length(y)$
$y = zeros(m, N)$
for $(j = 1 \rightarrow N)$ do
    $b[1, j] = j^q - (j-1)^\alpha$
    $a[1, j] = (j+1)^{(q+1)} - 2j^{(q+1)} + (j-1)^{(q+1)}$
end for
$y(:, 1) = y_0$
for $(i = 1 \rightarrow N)$ do
    $p = y(:, i) + \frac{h^q}{\Gamma(q+1)} \sum_i^{i=1} b[i] f(ih, y(i))$
    $y(:, i+1) = y(:, i) + \frac{h^q}{\Gamma(q+2)} \left(f(ih, p) + \left((i - 1\ + q) i^q\right) f(0, y[0]) + \sum_{k=1}^{j-1} a[i-k] f(kh, y[k]) \right)$
end for

2.3.2.2 Synchronization metrics

There is no unique way to quantify the amount of synchronization in real-time series, and a series of metrics have been proposed for this purpose. As a rough approximation, these metrics can be classified into three main groups: (i) linear, (ii) nonlinear, and (iii) spectral metrics, (Echegoyen et al., 2019).

While linear metrics, such as the Pearson correlation coefficient, are the most straightforward to calculate and less time-consuming, they assume the existence of a linear correlation between time series. This assumption is not fulfilled in most real cases. On the other hand, nonlinear metrics take a certain nonlinear coupling function f_n between a variable X and a variable Y, such as $X = f_n(Y)$.

In that sense, Echegoyen introduced Ordinary Synchronization (OS) as a new measure to quantify synchronization between dynamical systems. Ordinary Synchronization provides a fast and robust-to-noise tool to assess synchronization without any implicit assumption about the distribution of data sets nor their dynamical properties, capturing in-phase and anti-phase synchronization.

The OS and Pearson's correlation coefficient exhibit closed behavior for our study. Then, we will continue the analysis with the Pearson correlation due to its lower consumption and validate the results with the help of the LEs. The Pearson correlation, computed from the *i-th* state variable of the master and slave systems described by

$$r = \frac{\sigma_{N_{mi}} \sigma_{N_{si}}}{\sigma_{N_{mi} N_{si}}}, \tag{26}$$

where $\sigma_{N_{mi}} \sigma_{N_{si}}$ is the covariance between the data obtained from the time series of the state variables of the master and slave systems, and $\sigma_{N_{mi} N_{si}}$ is the standard deviation obtained from the *i-th* state variable of the master (slave) oscillator.

The Lyapunov exponent, which was initially developed by (Wolf et al., 1985), is based on the principle that the stabilization of unstable periodic orbits of a nonlinear system can be simplified to relatively small perturbations to a chaotic system. Therefore, this effective tool is considered a practical instrument to control chaos by quantifying the sensitive dependence on initial states, often called the "butterfly effect" We deduce from this useful tool that the dynamical system behavior is chaotic if the Lyapunov exponent is positive, the dynamical system behavior is chaotic. This implies the existence of an exponential divergence of nearby chaotic trajectories.

Lyapunov's exponent of a dynamical system can detect the presence of chaos and quantify the stability or instability of the system, and it is defined as follows:

Definition 2.4 *Let E be a finite real-dimensional vector space and $\mathcal{F}_E$ the vector space of the functions of the real variable, with values in E and defined in an interval $\mathcal{I} \subset \mathbb{R}$ of form $[t_0, +\infty[\, , t_0 > 0$. If f does not cancel in $\mathcal{I}$, the Lyapunov exponent of $f \in \mathcal{F}_E$ is defined by,*

$$\lambda_{(f)} = \lim_{t \to +\infty, t \in \mathcal{I}} \frac{\ln \|f(t)\|}{t}, \text{ and } \lambda_{(0)} = -\infty$$

where $\|.\|$ is the Euclidean norm chosen in E. If the quantity on the right side is a limit (instead of being an upper limit), then f admits the exact Lyapunov exponent $\lambda_{(f)}$.

To validate the existence of chaos, we will use the Pearson correlation and LEs indexes to evaluate the behavior of the fractional-order chaotic oscillators for different orders.

2.3.3 Numerical solutions for FO chaotic systems simulation

Solving differential equations of fractional (i.e., non-integer) order in an accurate, reliable, and efficient way is much more difficult than in the standard integer-order case; moreover, most computational tools do not provide built-in functions for this kind of problem.

The approximation of the solution of the fractional-order derivatives can be performed by applying the definitions of Riemmann-Liouville, Grünwald-Letnikov, and Caputo. Here, the time domain approximations well known as Grünwald-Letnikov, whose approximation expression is given in (27), and the predictor-corrector Adams-Bashforth-Moulton method given in (28) and (29), respectively, are used to simulate fractional-order oscillators.

$$
{}_aD_t^{\alpha} f(t) = \lim_{h \to 0} \frac{1}{h^q} \sum_{j=0}^{\left[\frac{t-a}{h}\right]} (-1)^j \begin{pmatrix} q \\ j \end{pmatrix} f(t - jh) \tag{27}
$$

$$
y_h^p\left(t_n+1\right) = \sum_{k=0}^{m-1} \frac{t_{n+1}^k}{k} y_0^{(k!)} + \frac{1}{\Gamma(q)} \sum_{k=0}^{n} b_{j,n+1} f\left(t_j, y_n\left(t_j\right)\right) \tag{28}
$$

$$
\begin{aligned}
y_h\left(t_{n+1}\right) = & \sum_{k=0}^{m-1} \frac{t_{n+1}^k}{k!} y_0^{(k)} + \frac{h^q}{\Gamma(\alpha+2)} f\left(t_{n+1}, y_h^p\left(t_{n+1}\right)\right) \\
& + \frac{h^q}{\Gamma(\alpha+2)} \sum_{j=0}^{n} a_{j,n+1} f\left(t_j, y_n\left(t_j\right)\right).
\end{aligned} \tag{29}
$$

(Garrappa, 2018) implemented the Predictor-Corrector (PECE) method of Adams-Bashforth-Moulton to solve this problem with high accuracy and is widely used to numerically simulate the solution of fractional-order systems with commensurate and non-commensurate order.

(Petráš, 2011) presented another solution derived from the Grünwald-Letnikov definition with

$$
y\left(t_k\right) = f\left(y\left(t_k\right), t_k\right) h^q - \sum_{j=v}^{k} c_j^q y\left(t_{k-j}\right) \tag{30}
$$

where q is the .fractional-order, which takes advantage of the short memory concept, and the binomial coefficients are truncated by a desired length of memory, which is suitable for hardware implementation like on a Field-Programmable Gate Array (FPGA).

The sum in (30) is associated with the algorithm's memory and can be truncated according to the short memory principle. Using this approach, the lowest index in the sum operation should be $v = 1$

for the case when $k < (L_m/h)$, and $v = k - (L_m/h)$ for the case $k > (L_m/h)$. Furthermore, without applying the short memory principle, one must set $v = 1$ for all values of k. It was evident that when performing this truncation, the error should increase, and then the solution may not converge. Furthermore, the length of memory, for example, if $f(t) \leq M$, L_m can be estimated using (31), barely including the required precision ε.

$$L \geqslant \left(\frac{M}{\varepsilon|\Gamma(1-q)|}\right)^{1/q} \tag{31}$$

The time domain Grünwald-Letnikov method is an explicit one, and as mentioned above, one can apply an implicit one, for instance, the well-known predictor-corrector Adams-Bashforth-Moulton method, (Deng & Lü, 2007). This approximation for the fractional-order derivatives of the chaotic oscillators is more exact than Grünwald-Letnikov, but requires a higher number of operations and hardware resources. The Adams-Bashforth-Moulton method is based on the fact that the fractional-order derivative of the form given in (32) is equivalent to Volterra's integral equation given in (33).

$$D_t^q y(t) = f(y(t), t), y^{(k)}(0) = y_0^{(k)}, k = 0, 1, \ldots, m-1 \tag{32}$$

$$y(t) = \sum_{k=0}^{[q]-1} y_0^{(k)} \frac{t^k}{k!} + \frac{1}{\Gamma(q)} \int_0^t (t-\tau)^{q-1} f(\tau, y(\tau)) d\tau \tag{33}$$

Both time domain numerical methods Grünwald-Letnikov (27) and Adams-Bashforth-Moulton (28)–(29) have approximately the same exactness and a good approximation of the solution of a fractional-order dynamical system, as for the chaotic oscillators.

In the following section, we analyze the chaotic behavior of the oscillators before entering the synchronization analysis. The idea is to study the more stable chaotic behavior of the oscillators against variation in the fractional-order and use it as a case study in the dynamically coupled fractional-order oscillators.

2.3.4 Application examples

The fractional-order of the Chua, Rössler and Lorenz chaotic oscillators are

$$\begin{aligned} \mathcal{D}^{q_1} x &= \alpha\left(y - x - h(x)\right), \\ \mathcal{D}^{q_2} y &= x - y + z, \\ \mathcal{D}^{q_3} z &= -\beta y - \gamma z, \end{aligned} \tag{34}$$

with $h(x) = bx + 0.5(a - b)\left[|x+1| - |x-1|\right]$,

$$\begin{aligned} \mathcal{D}^{q_1} x &= -(y+z), \\ \mathcal{D}^{q_2} y &= x + ay, \\ \mathcal{D}^{q_3} z &= z\,(x-c) + b, \end{aligned} \tag{35}$$

and,

$$\begin{aligned} \mathcal{D}^{q_1} x &= \sigma\,(y-x)\,, \\ \mathcal{D}^{q_2} y &= \gamma x - xz - y, \\ \mathcal{D}^{q_3} z &= xy - \beta z, \end{aligned} \tag{36}$$

in the same sequence. For the commensurate order system, the fractional-order is $q_1 = q_2 = q_3 = q$. The dynamic described by (34), (35) and (36) is restricted to have at least one eigenvalue in the unstable region to present a chaotic behavior, that is, condition (24) is met for at least one of its eigenvalues.

To analyze the critical order of integration when the system presents a chaotic behavior, we found the system's eigenvalues obtained by the Jacobian matrix evaluated at the equilibrium point,

$$J = \left(\partial F(\chi)/\partial \chi\right)|_{E_1}. \tag{37}$$

The parameters for the Chua oscillator are $(\alpha, \beta, a, b, \gamma) =$ (10, 14.87, -1.27, -0.68, 0.1). Substituting the parameters into the Jacobian matrix, the eigenvalues obtained by evaluating the equilibrium point $E_1 = (1.883, 0.012, -1.870)$ are $(-4.645, 0.172 \pm 3.172j)$. From the condition (24) we have the critical order

$$q_c = \frac{2}{\pi}|\min\left(\arg\left(\lambda_i\right)\right)| = 0.965. \tag{38}$$

For the Rössler system, the parameters are $(a, b, c) =$ (0.2, 0.2, 5.7) with a critical fractional-order $q_c = 0.938$ and the Lorenz oscillator presents a chaotic behavior from $q_c \geq 0.994$ with $(\sigma, \gamma, \beta) =$ (10, 28, 8/3). This analysis is validated by the bifurcation diagrams shown in Figure 4, where the local maxima in x are plotted as a function of the integration order q variation.

The simulation coincides with the analytic analysis for the critical value or the fractional-order that meets the chaotic condition of the system. Because the Rössler system presents a wide range of fractional-order under chaotic behavior, it will be taken to study the synchronization under a bidirectional dynamic fractional-order coupling.

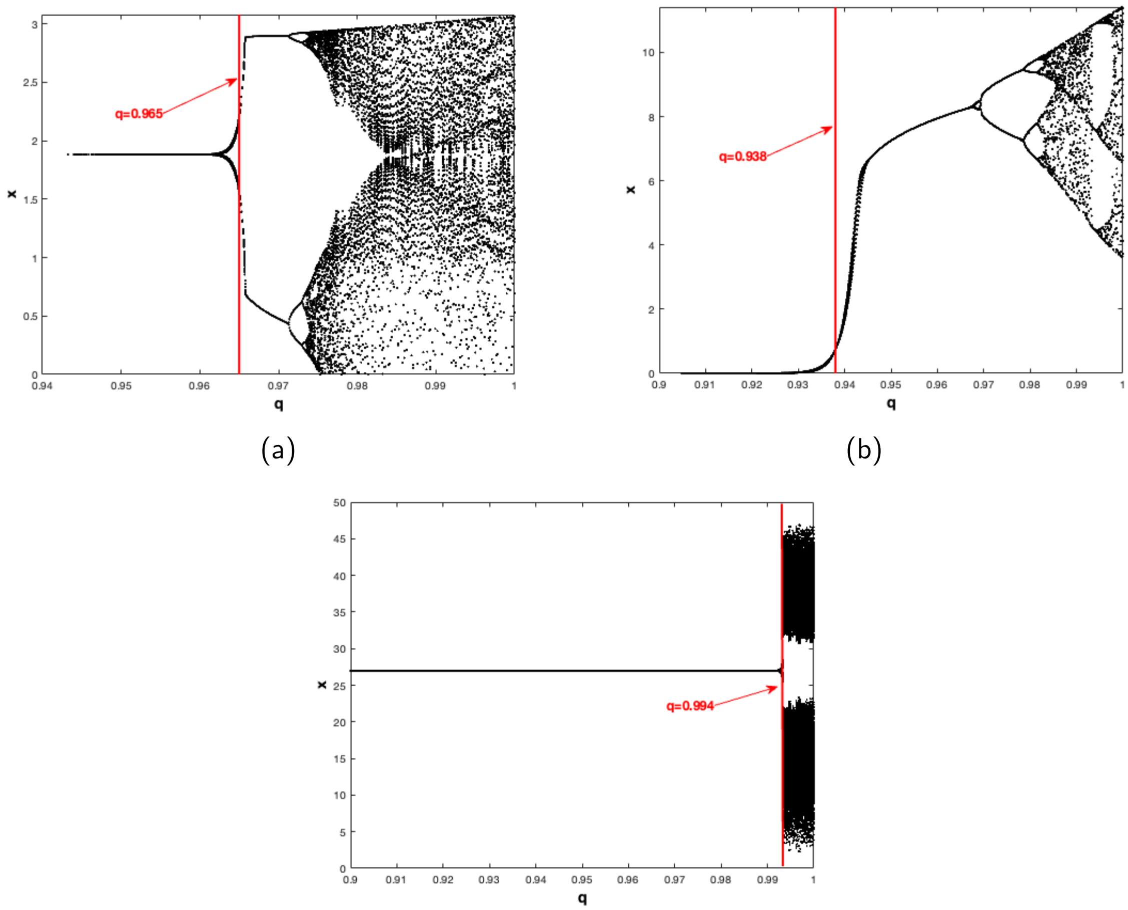

(a) (b)

(c)

Figure 4. Bifurcation of the a) Chua, b) Rössler, c) Lorenz systems for fractional-order $0.9 \leq q \leq 1$.

2.3.5 Results

Since the Rössler oscillator allows a synchronization study for a bigger fractional-order span, we present the results using the Pearson coefficient, Lyapunov exponent metrics and numerical simulations in this section.

From (16) and (23) the stability condition is

$$|\arg(\lambda_i(\tilde{A}))| > q\frac{\pi}{2} \tag{39}$$

with $q > 0.938$ for Rössler oscillator. For a simpler analysis, we assumed the following conditions,

$$B_1 = \begin{bmatrix} 1 & 0 \\ 0 & 0 \\ 0 & 0 \end{bmatrix}, \begin{bmatrix} 0 & 1 \\ 0 & 0 \\ 0 & 0 \end{bmatrix}, \begin{bmatrix} 0 & 0 \\ 1 & 0 \\ 0 & 0 \end{bmatrix}, \begin{bmatrix} 0 & 0 \\ 0 & 1 \\ 0 & 0 \end{bmatrix}, \begin{bmatrix} 0 & 0 \\ 0 & 0 \\ 1 & 0 \end{bmatrix}, \begin{bmatrix} 0 & 0 \\ 0 & 0 \\ 0 & 1 \end{bmatrix}, \tag{40}$$

$$B_3 = \begin{bmatrix} 0 & 0 & 0 \\ 1 & 0 & 0 \end{bmatrix}, \begin{bmatrix} 0 & 0 & 0 \\ 0 & 1 & 0 \end{bmatrix}, \begin{bmatrix} 0 & 0 & 0 \\ 0 & 0 & 1 \end{bmatrix} \tag{41}$$

with $k = 1$ and $B_1 \equiv B_2$. The following figures show a heatmap with all the possible configurations that ensure complete synchronization of the oscillators through a fractional-order dynamic coupling for different k values, $k = 1, 10, 20$. Figure 5 ensures a complete synchronization with any combination of B_1 and B_2 while using the error of the first state $B_3 = [0, 0, 0/1, 0, 0]$. All the other combinations can vary depending on the value of the coefficient k. Still, those cases with a value greater than 0.938 meet the condition (20), and we can confirm that the oscillators are synchronized.

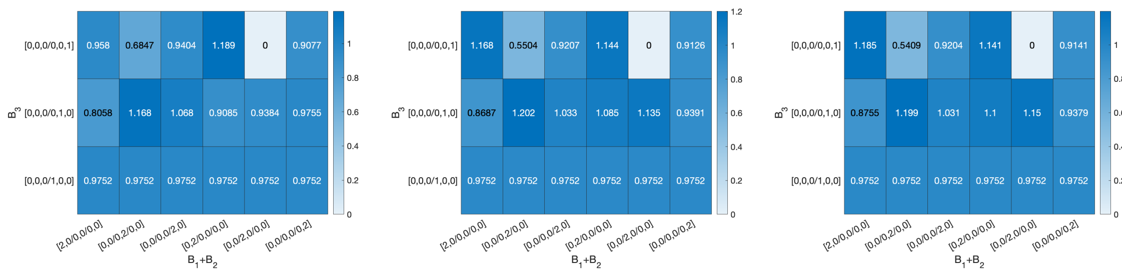

Figure 5. Heatmap of synchronization condition for Rössler oscillator.

This previous analysis allowed explorers to the synchronization scheme conditions for the Rössler oscillator under a bidirectional fractional-order dynamic coupling. Now, with the configuration

$$B_1 = B_2 = \begin{bmatrix} 1 & 0 \\ 0 & 0 \\ 0 & 0 \end{bmatrix}, B_3 = \begin{bmatrix} 0 & 0 & 0 \\ 1 & 0 & 0 \end{bmatrix}, \tag{42}$$

the synchronization is analyzed using the Pearson correlation and Lyapunov exponent metrics for $0.94 \leq q \leq 1$, and $0 \leq k \leq 20$. The Pearson correlation coefficient ρ proves a high correlation between two variables if the coefficient is close to 1. For our study, since the system order is $n = 3$, the sum of the coefficients must be close to 3 to guarantee synchronization. In Figure 6, it can be seen that the coefficient is close to 3 for all fractional-order ranges and $k > 3$, ensuring synchronization between the states of both oscillators.

Nowadays, there are two widely used definitions of LEs: via the exponential growth rates of the norms of the columns of the fundamental matrix and the exponential growth rates of the singular values of the fundamental matrix (Danca & Kuznetsov, 2018). The numerical integrations required by the LEs algorithm for fractional-order systems are performed with the Adams-Bashforth-Moulton (ABM) predictor-corrector method for fractional differential equations, proposed (Diethelm et al., 2002) which is constructed for the fully general set of equations.

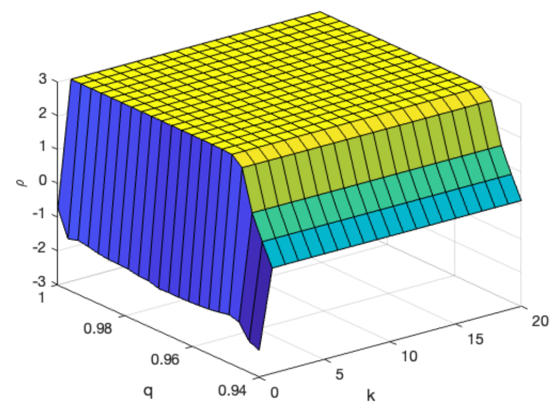

Figure 6. Pearson correlation coefficient for Rössler oscillators under bidirectional dynamic fractional-order coupling.

Figure 7 shows the analysis applying the Lyapunov exponents metric obtained by the Matlab code in (Danca & Kuznetsov, 2018), where synchronization is proven when the existence of a positive exponent is zero. The graph shows that the oscillators are synchronized for all $k > 0$. Finally, numerical simulations show the synchronization of both oscillators under a bi-directional fractional-order coupling at the first state, using first and second-state coupling errors with fractional-order $q = 0.97$, $k = 5$.

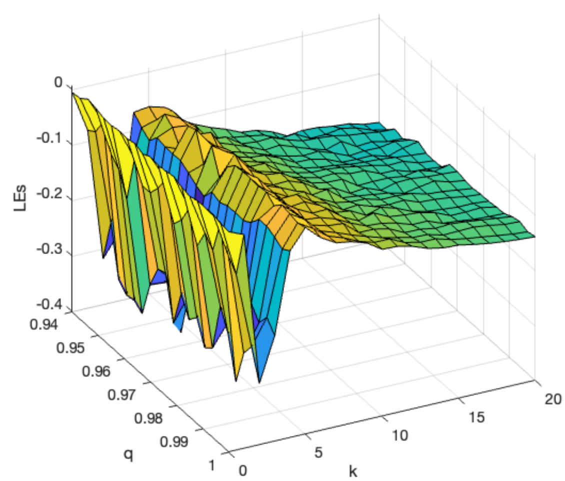

Figure 7. Lyapunov exponents for Rössler oscillators under bidirectional dynamic fractional-order coupling.

Example 1 in Figure 8 with

$$B_1 = B_2 = \begin{bmatrix} 1 & 0 \\ 0 & 0 \\ 0 & 0 \end{bmatrix}, B_3 = \begin{bmatrix} 0 & 0 & 0 \\ 1 & 0 & 0 \end{bmatrix}, \tag{43}$$

and Example 2 in Figure 9 with

$$B_1 = B_2 = \begin{bmatrix} 1 & 0 \\ 0 & 0 \\ 0 & 0 \end{bmatrix}, B_3 = \begin{bmatrix} 0 & 0 & 0 \\ 0 & 1 & 0 \end{bmatrix}. \tag{44}$$

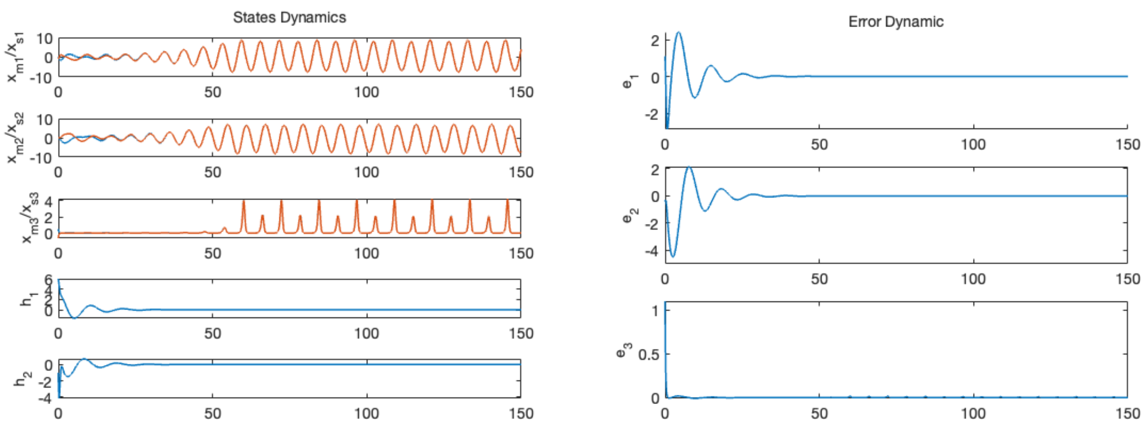

Figure 8. State and error dynamics of chaotic oscillators synchronization using first state error.

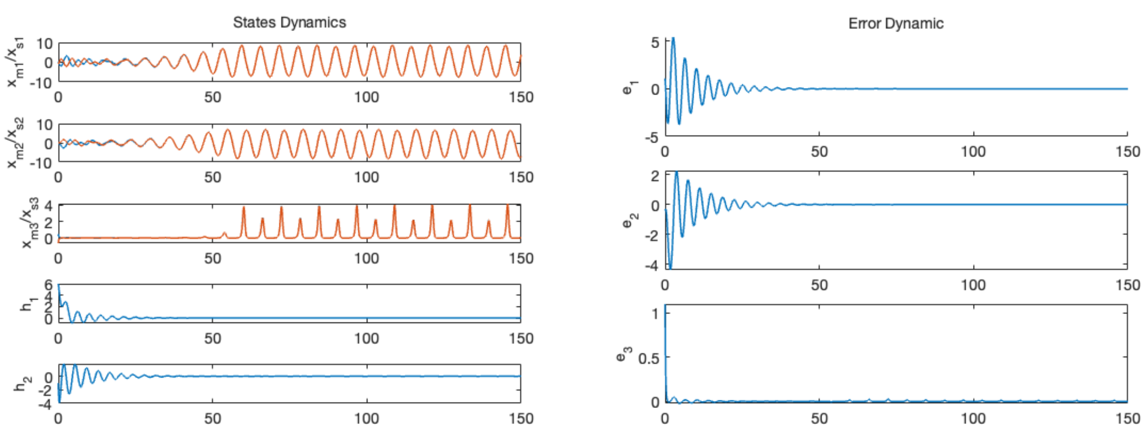

Figure 9. State and error dynamics of chaotic oscillators synchronization using second state error.

2.4 Conclusions

In this chapter, we explored how fractional-order dynamic coupling influences the synchronization of chaotic oscillators, with a specific emphasis on the Rössler oscillator. We aimed to improve the synchronization dynamics between these oscillators by introducing bidirectional fractional-order dynamic coupling, showing an improvement against fractional-order directional coupling methods (Echenausía-Monroy et al., 2021). The expanded synchronization region indicates the improved effectiveness of bidirectional fractional-order coupling in facilitating synchronization among fractional-order chaotic oscillators.

This preliminary study is a fundamental starting point for delving into this complex subject matter, setting the stage for future explorations and in-depth analyses using the same methodology.

Chapter 3. Consensus on thermal systems

3.1 Introduction

Thermal systems involve the storage, transfer, and conversion of energy. Energy can be stored within a system in different forms, such as kinetic energy and gravitational potential energy. Energy also can be stored within the matter making up the system. Energy can be transferred between a system and its surroundings by work, heat transfer, and the flow of hot or cold streams of matter. Energy also can be converted from one form to another, (Moran, 2003).

Thermal processes have existed since the earliest phases of the earth's formation. However, as humans gained more insights into the elusive concept of heat and its connection to the ability to do work, the idea of using a thermal system was born, (Boehm, 1997). Since then, the basic mechanisms of heat transfer, conduction, convection, and radiation have been studied.

Thanks to advances in technology and research, thermal processes have become more efficient and reliable for humankind, converting into an essential process in manufacturing, electronics, aerospace, and environmental management. The study of the thermal systems in the industry has created the design of a similar process at a lower scale to analyze and understand its behavior and leverage numerous factors around this process, like stability, safety, and efficiency. Available temperature training platforms are focused on Single Input Single Output (SISO) control loops or 2x2 Inputs Multiple Outputs (MIMO) systems. This means that working with high-order MIMO systems featuring control loops isn't feasible on these platforms because of their complexity and some space limitations.

The upcoming sections will cover modeling, control strategies, and Digital Twin aspects of a designed thermal system platform with multiple inputs and outputs, allowing the possibility of studying thermal systems of high complexity, never presented before.

3.2 Modeling of thermal systems

The fundamentals of mathematical methods used today to model thermal systems were developed centuries ago by great mathematicians and scientists such as Laplace, Fourier, Poisson, and Stefan. The analytical solution of the equations describing the basic mechanisms of heat transfer – conduction, convection, and radiation– was always considered an extremely challenging mathematical problem. The study of energy transfer in thermal systems continues to be an important topic in engineering because it forms the basis of analysis of energy efficiency for indoor environmental controls, industrial processes, and all forms of energy transformation.

Temperature is usually dependent on spatial and temporal coordinates. As a result, the dynamics of thermal systems have to be described by partial differential equations. Moreover, radiation and convection are by their very nature nonlinear, further complicating the solutions. Few problems of practical interest described by nonlinear partial differential equations have been solved analytically, and the numerical solution usually requires an extensive study to be carried out with sophisticated finite-element and computational fluid dynamics software, (Kulakowski et al., 2007).

Other techniques, besides the use of analytical models, are Empirical models, using Finite Difference Method (FDM), Finite Element Method (FEM), Computational Fluid Dynamics (CFD), Lumped parameter models, System identification techniques, Computational heat transfer models, and Thermal quadrupole. The selection of one of these techniques will depend on the complexity, the level of accuracy required, the available data, and the purpose of the analysis or simulation. In some occasions, the model of the system is performed by multiple models that can be based on different techniques. In order to understand this process, the research community has created a training platform that represents real industrial thermal systems for modeling and control. That is why in the literature, we can find different training rigs, but these are expensive, require laboratory arrangements, have higher heating and cooling response times, and most of them are limited to SISO control loops or 2x2 MIMO systems.

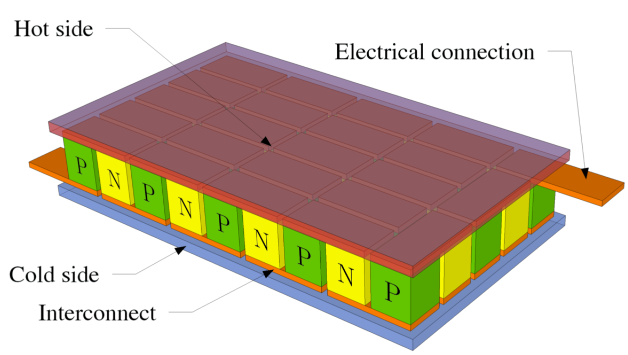

Figure 10. Peltier module

A novel high-order thermal system is designed and developed to study this process at low cost, portable, and for educational purposes. The platform was built with Peltier modules. A Peltier module, also known as a thermoelectric cooler (TEC), is a semiconductor device that enables the transfer of heat from one side to the other when an electric current is applied. It operates on the principle of the Peltier effect, which is named after the French physicist Jean Charles Athanase Peltier, who discovered it in 1834, (Peltier, 1834).

The Peltier effect is a phenomenon that occurs when an electric current flows through the junction of two different materials, typically N-type and P-type semiconductors, Figure 10. When the current flows in one direction, heat is absorbed at one junction (the cold side) and released at the other junction (the hot side). Reversing the current direction will reverse the heat transfer direction.

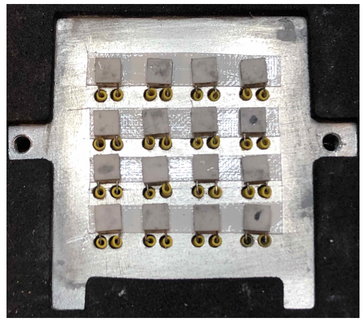

Figure 11. 4x4 Peltier array

The Peltier module can be used for both heating and cooling applications depending on the direction of the electric current. When used for cooling, it is often employed in electronic devices, such as Central Processing Unit (CPU) coolers, refrigerators, and portable coolers, to remove heat from the device and keep it operating at a lower temperature (Kungwalrut et al., 2017; Wen et al., 2014; Takahashi et al., 2012). For heating applications, it can be used for items such as heating plates or in temperature-regulated environments, (Viola et al., 2020).

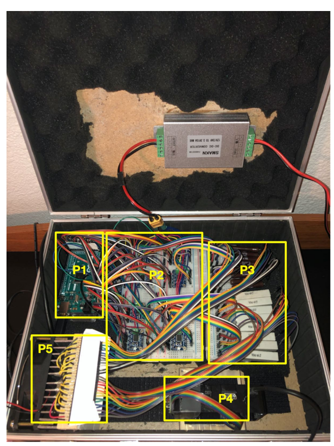

Figure 12. PHELP experimental platform

While Peltier modules have certain advantages, such as being solid-state with no moving parts, they also have limitations, including relatively low efficiency compared to traditional refrigeration methods such as compressors and limitations in the amount of heat they can move. As a result, they are most effective in applications with low heat loads or where precise temperature control is necessary.

Introducing the Pixel Heating Experiments Learning Platform (PHELP), a low-cost, real-time, high-order MIMO temperature uniformity control platform for education and research comprised of a set of 16 Peltier modules, Figure 11, individually controlled in a flat array configuration, which functions as heating and cooling elements.

The PHELP training platform is presented in Figure 12, and its block diagram in Figure 13. As can be observed, the system is composed of an array 4 by 4 of Peltier modules, a thermal infrared camera, operating on a Raspberry Pi (P4), which sends the temperature data using TCP/IP protocol, and an Arduino board (P1) set up on hardware in the loop (HIL) configuration with Matlab-Simulink to perform the data acquisition, identification, and control tasks for the system. A power block is included made up of a PWM generator and a power driver (P2) to manage the power applied to each Peltier module according to the control action defined by the control algorithm. Between the Peltier module and the Power Driver, a module of power resistors (P3) is used to dissipate the power in the line and to guarantee the maximum voltage and current handled by the Peltier.

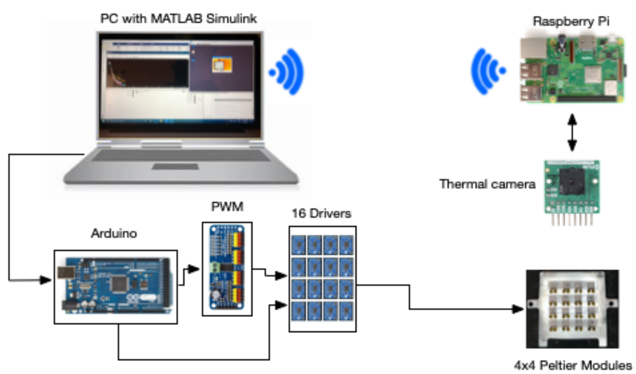

Figure 13. PHELP platform block diagram

The Peltier array was constructed with the NL1020T module employed as a heating element because it is a solid-state device with low maintenance requirements and a long service lifetime. The temperature range for this device starts from 15 ^oC to 100 ^oC, with a maximum heating of 1 W and a power requirement of 0.9 V DC and 1.8 Amps. The power on the Peltier system is controlled using pulse width modulation managed by the Arduino board, PWM/Servo Driver, and power driver. PWM signal range goes from -4000 to 0 for cooling and from 0 to 4000 for heating. Over the Peltiers shown in Figure 11, an aluminum surface was placed to create the interaction between the 16 Peltiers. The temperature control system regulates the value in the place of each Peltier depending on the desired value; it always must be physically realizable. Also, the heat sink was modified to install all the Peltiers and dissipate the extra heat, to extend the modules' lifetime.

A low-cost infrared thermal camera, Figure 14, is used as a feedback sensor for the system, which gives a visual distribution of the uniformity of temperature. Finally, in the heatsink, a fan (P5) is installed to dissipate the heat generated by the Peltier modules. Figure 14 shows on the left an image of the heating process and on the right the cooling process. In both images, green dots placed represent the measurement points of the system, which are aligned with the Peltiers modules. The camera is manufactured by FLIR, which is a long-wave infrared camera that measures the temperature over a surface through its infrared-emitted radiation. The wavelength range for this camera ranges from 8 μm to 14 μm with a maximum frame rate of 9 FPS. The camera has a resolution of 80x60 pixels with an accuracy of $\pm$0.5 ^oC, and its size is less than a quarter coin. In addition, the camera has an SPI interface, which allows its connection with many edge devices. Additionally, the LeptonThread software development kit is available for camera data acquisition, which runs in Python and C++. For this platform, the thermal camera works together with a Raspberry Pi 3B+, which reads the camera through the SPI interface, sending the data to Matlab-Simulink employing a TCP/IP client-server configuration. In this system, the thermal camera with the Raspberry Pi acts as the server, and the Matlab-Simulink application runs as the client for the thermal data camera. An example of the image of the infrared vision camera that works on the Raspberry Pi is presented in the middle of Figure 14.

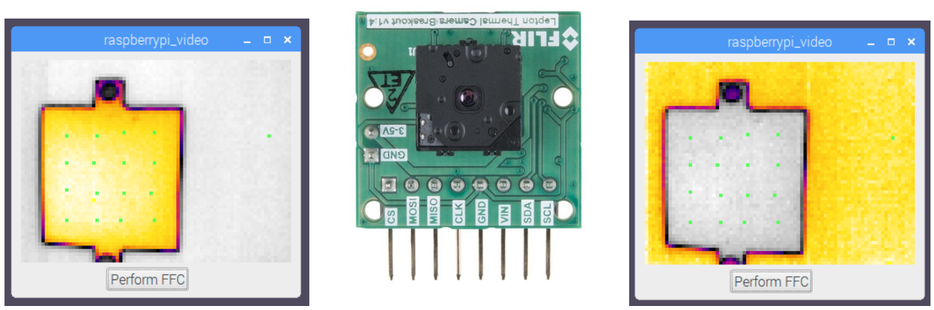

Figure 14. FLIR Lepton thermal camera

Figure 15 shows the power management interface employed in the PHELP system. It is made up of an Arduino Mega board that works as a data acquisition interface with the MATLAB-Simulink software. It is configured as HIL in order to obtain a real-time interaction of the real system with the PC. After sending the control signal through the Arduino, this signal splits in magnitude (to the PWM/Servo Driver) and direction (to the power driver). Finally, the PWM/Servo Driver applies the PWM signal to the power driver to control the current in each Peltier and the temperature as a consequence. The Adafruit 16-channel 12-bit PWM/Servo Driver was used to communicate with the Arduino board using the I2C protocol and the Adafruit TB6612 1.2A DC/Stepper Motor Driver with a range of 4.5V DC to 13.5 V DC.

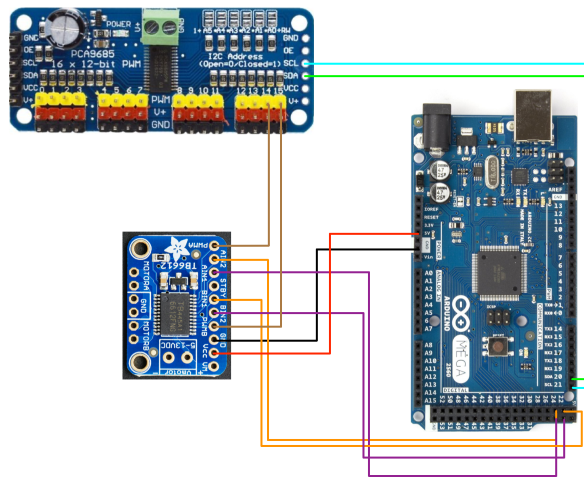

Figure 15. Arduino Mega, PWM generator and TB6625 motor driver

Table 2 shows the total cost of this platform. As can be observed, the overall cost of the platform is $\$727.00$ USD, which is an affordable cost for many engineering schools interested in MIMO complex temperature control training. In the following section, a fractional-order transfer function is obtained to represent the dynamic of the platform, and also Data-Driven techniques with a good fit.

Table 2. Temperature training platform total cost

Component	Quantity	Total Price
16 Peltier module	16	$288.00 USD
Raspberry PI 3B+	1	$ 35.00 USD
Arduino Mega board	1	$ 30.00 USD
PWM/Servo Driver	1	$ 15.00 USD
Dual Power drivers	8	$ 80.00 USD
Thermal Camera	1	$229.00 USD
Others		$ 40.00 USD
Total cost		$727.00 USD

3.2.1 Consensus using fractional order transfer functions

In the realm of mathematics and engineering, fractional calculus has emerged as a powerful and intriguing field that extends traditional calculus to non-integer orders. By introducing fractional derivatives and integrals, it provides a more comprehensive framework to model complex phenomena in various disciplines, particularly in the analysis and control of dynamic systems.

Traditional calculus deals with integer-order derivatives and integrals, which are fundamental for modeling linear and time-invariant systems. However, many real-world systems exhibit nonlocal memory and long-term correlations, which cannot be accurately described by integer-order calculus. The fractional calculus addresses this limitation by introducing fractional derivatives, denoted by D^{α}, where α represents a real order. Fractional derivatives can be defined through different mathematical frameworks, such as the Riemann-Liouville (RL), Caputo, or Grünwald-Letnikov (GL) definitions (Oldham & Spanier, 1974; Podlubny, 1999).

The continuous integro-differential operator is defined as

$$
{}_aD_t^\alpha = \begin{cases} \frac{d^\alpha}{dt^\alpha} & : \alpha > 0, \\ 1 & : \alpha = 0, \\ \int_a^t (d\tau)^{-\alpha} & : \alpha < 0. \end{cases} \tag{45}
$$

The GL definition is given by

$$
{}_aD_t^\alpha f(t) = \lim_{h \to 0} h^{-\alpha} \sum_{j=0}^{\left[\frac{t-a}{h}\right]} (-1)^j \begin{pmatrix} \alpha \\ j \end{pmatrix} f(t - jh), \tag{46}
$$

where [.] means the integer part, the RL as

$$
{}_aD_t^\alpha f(t) = \frac{1}{\Gamma(n-\alpha)} \frac{d^n}{dt^n} \int_a^t \frac{f(\tau)}{(t-\tau)^{\alpha-n+1}} d\tau \tag{47}
$$

for $(n - 1 < \alpha < n)$ and where $\Gamma(.)$ is the $Gamma$ function, and the Caputo definition can be written as

$$
{}_aD_t^\alpha f(t) = \frac{1}{\Gamma(\alpha - n)} \int_a^t \frac{f^{(n)}(\tau)}{(t-\tau)^{\alpha-n+1}} d\tau \tag{48}
$$

for $(n-1 < \alpha < n)$. The initial conditions for the fractional-order differential equations with the Caputo derivatives are in the same form as for the integer-order differential equations. In the above definition, $\Gamma(m)$ is the factorial function, defined for positive real m, by the following expression:

$$
\Gamma(m) = \int_0^\infty e^{-u} u^{m-1} du \tag{49}
$$

for which, when m is an integer, it holds that:

$$
\Gamma(m+1) = m! \tag{50}
$$

In system theory, the analysis of dynamical behaviors is often done by means of transfer functions. With this in view, the introduction of the Laplace transform of non-integer order derivatives is necessary for an optimal study. Fortunately, not very large differences can be found with respect to the classical case, confirming the utility of this mathematical tool even for fractional systems. The inverse Laplace transformation is also useful for the time domain representation of systems for which only the frequency response is known.

The most general formula is the following,

$$L\left\{\frac{d^{\alpha}f(t)}{dt^{\alpha}}\right\} = s^{\alpha}L\{f(t)\} - \sum_{k=0}^{n-1} s^{k}\left[\frac{d^{\alpha-1-k}f(t)}{dt^{\alpha-1-k}}\right]_{t=0} \tag{51}$$

where n is an integer such that $n-1<\alpha<n$. This expression becomes very simple if all the derivatives are zero:

$$L\left\{\frac{d^{\alpha}f(t)}{dt^{\alpha}}\right\} = s^{\alpha}L\{f(t)\} \tag{52}$$

The expression (52) is very useful to calculate the inverse Laplace transform of elementary transfer functions, such as noninteger order integrators $\frac{1}{s^{\alpha}}$. In fact, replacing α with $-\alpha$ and considering $f(t) = \delta(t)$, the Dirac impulse, by means of the Caputo definition (48), holds that:

$$L\left\{\frac{t^{m-1}}{\Gamma(m)}\right\} = \frac{1}{s^{m}}; \quad L^{-1}\left\{\frac{1}{s^{m}}\right\} = \frac{t^{m-1}}{\Gamma(m)} \tag{53}$$

that is the impulse response of a noninteger order integrator.

A literature review on fractional-order transfer function models shows that in the last two decades, fractional-order models have received more attention in system identification than classical integer-order model transfer functions. The literature shows that some techniques on fractional calculus and fractional-order models have been presenting valuable contributions to real-world processes and achieved better results. Such new developments have impelled research to extend classical identification techniques to advanced fields of science and engineering (Kothari et al., 2019).

Fractional-order models have been widely used in modeling and identification of thermal systems. By considering the concepts of fractional calculus in modeling real-world systems, the models obtained can describe the behavior of these systems more adequately compared to traditional models of integer order. Many diffusive phenomena, such as heat transfer, can be better described by fractional-order models (Badri & Tavazoei, 2015). In a study on thermal system identification using fractional models for high temperature levels around different operating points, it was found that because of their compactness, as compared to rational models and finite element models, fractional models are suitable for modeling such diffusive phenomena. For large temperature variations, thermal characteristics such as thermal conductivity and specific heat vary along with the temperature. In this context, the thermal diffusion obeys a nonlinear partial differential equation and cannot be modeled by a single linear model (Maachou et al., 2012).

On the other hand, Dynamic Consensus Networks are a type of network that can be used to model and analyze thermal processes in buildings. In these networks, nodes represent integrators, and edges are 2-tuples of real rational functions representing dynamical systems that couple the nodes. The idea is to generalize the notion of graphs with integrating nodes and dynamic edges and to give conditions under which such graphs admit consensus, which means that in the steady state, the node variables converge to a common value (Moore et al., 2011).

This approach is motivated by the problem of modeling thermal processes in buildings, where weights are no longer static gains, but instead represent dynamical systems. The consensus variable is calculated via a dynamic consensus protocol that extends the standard static consensus protocol in two ways: (1) the connection variables are transfer functions, and (2) different connection weights are allowed to multiply the current estimate of the node and the estimates of other nodes.

In this problem, suppose that N agents n_i evolve their individual belief ξ_i about a global consensus variable ξ using nearest neighbor communications according to the consensus protocol.

$$\dot{\xi}_i = -\sum_{j \in \mathcal{N}_i} \lambda_{ij}(\xi_i - \xi_j), \tag{54}$$

where $\mathcal{N}_i$ is the collection of indices of all agents n_j with whom agent n_i can communicate. More information on this topic can be found in (Olfati-Saber et al., 2007).

We consider the problem in the form of

$$\Xi_i(s) = -\frac{1}{s} \sum_{j \in \mathcal{N}_i} \left[\lambda_{ij}^S(s)\Xi_i(s) - \lambda_{ij}^C(s)\Xi_j(s) \right] \tag{55}$$

where $\Xi_i(s)$ is the Laplace transform of $\xi_i(t)$ and we define the real rational (transfer) functions $\lambda_{ij}^S(s)$ and $\lambda_{ij}^C(s)$ to be the self-correction term and the cross-correction term, respectively, for the node n_i.

Many systems fall into the dynamic consensus framework, particularly large-scale systems described by interconnected storage elements (Moore et al., 2011). In the case when two rooms are separated by a wall, Figure 16 and there are no external heat flows, the temperatures in each room can be described by

$$T_i(s) = -\frac{1}{C_i^r s}\left[\frac{A_{ij}(s)}{B_{ij}(s)} T_i(s) - \frac{D_{ij}(s)}{B_{ij}(s)} T_j(s)\right], \tag{56}$$

Following the same analogy, the thermal system platform can be described by,

$$Y(s) = \begin{bmatrix} G_{1,1}(s) & G_{1,2}(s) & \dots & G_{1,16}(s) \\ G_{2,1}(s) & G_{2,2}(s) & \dots & G_{2,16}(s) \\ \vdots & \vdots & \ddots & \vdots \\ G_{16,1}(s) & G_{16,2}(s) & \dots & G_{16,16}(s) \end{bmatrix} U(s) \tag{57}$$

where $G_{i,j}(s)$ denotes the interaction between the input i and the output j of the 4x4 Peltier modules matrix and is identified using a transfer function with the structure of a Fractional Order Plus Dead Time system (FOPDT) given by (58), where K_{ij} is the system gain, T_{ij} is the system time constant, α is the fractional-order of the denominator, and L_{ij} is the time delay for the system for the i and j columns of the transfer function array.

$$G_{ij}(s) = \frac{K_{ij}}{(T_{ij}s^{\alpha_{ij}} + 1)} e^{-L_{ij}s}, \qquad i, j = 1, 2, \dots, 16. \tag{58}$$

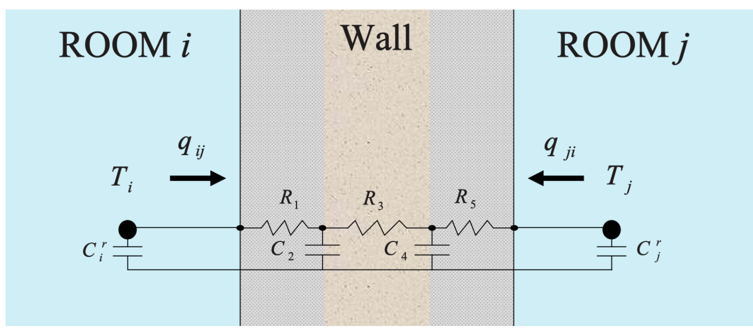

Figure 16. Two rooms connected by a wall using the 3R2C model.

A robust identification experiment is designed for the temperature system in order to identify its uncertainty. This experiment consists of applying a stepped signal with different amplitudes. The dynamic behavior of each Peltier and the interaction between them was measured in the 16 Peltiers for a total of 256 data vectors. Figure 17 shows the identification data acquired from Peltier for the first row and column of the Peltier array shown in Figure 11.

$$\begin{aligned} G_1(s) &= \frac{1.3026}{15.153s^{0.9} + 1} \\ G_2(s) &= \frac{2.3329}{8.3473s^{0.6} + 1} \\ G_3(s) &= \frac{3.3999}{6.7947s^{0.5} + 1} \end{aligned} \tag{59}$$

Equations (59) show that the system presents different models for each stepped signal applied. Based on these, it is possible to define the family of plants for the temperature system with uncertainty boundaries for K, T and α, defined by (58).

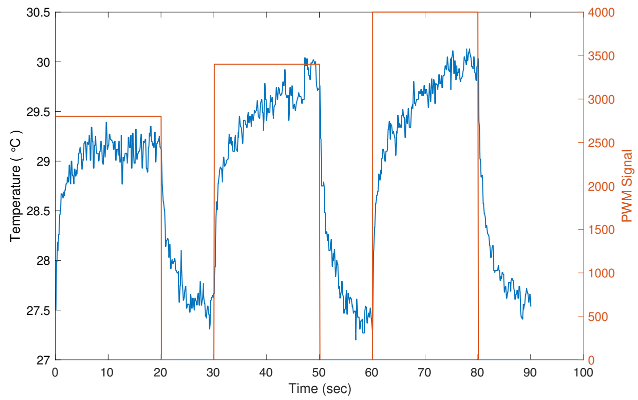

Figure 17. Identification signal for the Peltier module

The gap metric is a measure of the distance between two Linear Time-Invariant (LTI) systems. It was introduced by Zames and El-Sakkary to model uncertain systems and to measure the distance between systems. A modified gap, called the ν-gap, was later discovered by Vinnicombe and was shown to have advantages (Qiu & Zhao, 2021).

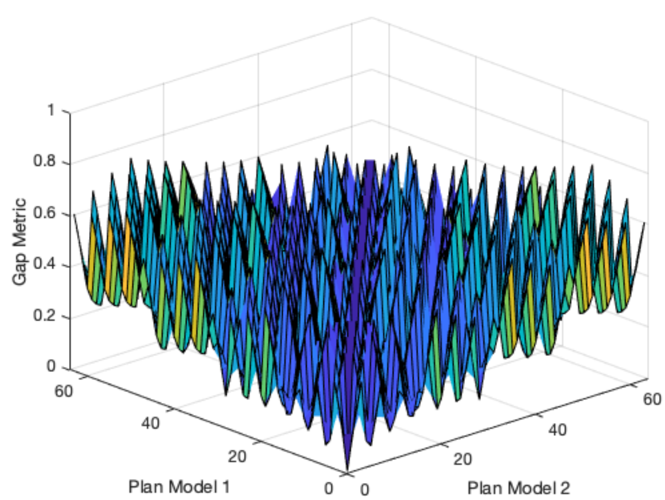

Figure 18. Gap metric surface

The gap metric values satisfy $0 \leq \nu$-gap $\leq$ gap ≤ 1. Values close to zero imply that any controller that stabilizes one system also stabilizes the other with similar closed-loop gains. The gap metric is used in robust control, where it is necessary to start with a model of system uncertainty. A good uncertainty model needs to capture the possible perturbations and uncertainties of the system and must be mathematically tractable.

After that, the gap metric among plants is calculated, producing a gap metric matrix, with the help of the Oustaloup approximation of fractional-order systems for CRONE. The gap metric surface for the set of plants is shown in Figure 18, where it is possible to see that the gap metric converges close to zero. For the first Peltier, the nominal model is

$$G(s) = \frac{1.3026}{12.367s^{0.5} + 1} \tag{60}$$

and the rest of the model appears in Table 3.

Considering that the system has 256 transfer functions, Table 4 presents the model parameters for the main diagonal of $Y(s)$. For these cases, the term L is equal to zero because the nonlinear system does not have a time delay on the main diagonal. All PHELP system identification data and parameters are available in (Rodriguez, 2020).

The validation of the MIMO model (57) is shown in Figure 19, where the blue lines are the model outputs and the red lines are the real validation data. As observed, the identified model fits the validation data.

Table 3. $Y(s)$ main diagonal transfer functions parameters

	G_1	G_2	G_3	G_4	G_5	G_6	G_7	G_8
K	1.30	1.61	0.79	1.83	1.45	0.67	0.26	0.72
T	12.36	20.13	17.89	20.82	21.51	35.43	9.10	11.60
α	0.5	0.75	0.86	0.5	0.65	0.85	0.65	0.65
	G_9	G_{10}	G_{11}	G_{12}	G_{13}	G_{14}	G_{15}	G_{16}
K	1.11	1.41	0.92	0.61	0.94	0.69	0.30	0.73
T	23.12	18.38	28.27	16.58	8.41	15.62	7.57	5.34
α	0.61	0.5	1	0.9	0.65	0.5	0.5	0.9

Table 4. Model FIT

M_1	M_2	M_3	M_4	M_5	M_6	M_7	M_8
76.03	79.88	80.61	83.43	78.02	78.00	73.93	86.59
M_9	M_{10}	M_{11}	M_{12}	M_{13}	M_{14}	M_{15}	M_{16}
75.98	78.39	79.96	75.33	78.99	76.83	76.08	80.87

3.2.2 Data-driven techniques

Data-driven dynamical Systems is a rapidly evolving field that focuses on discovering dynamics from data and finding data-driven representations that make nonlinear systems amenable to linear analysis

(Brunton & Kutz, 2019). This field combines established and emerging methods from data science and machine learning to tackle the challenges of nonlinear dynamics and unknown or partially known dynamics.

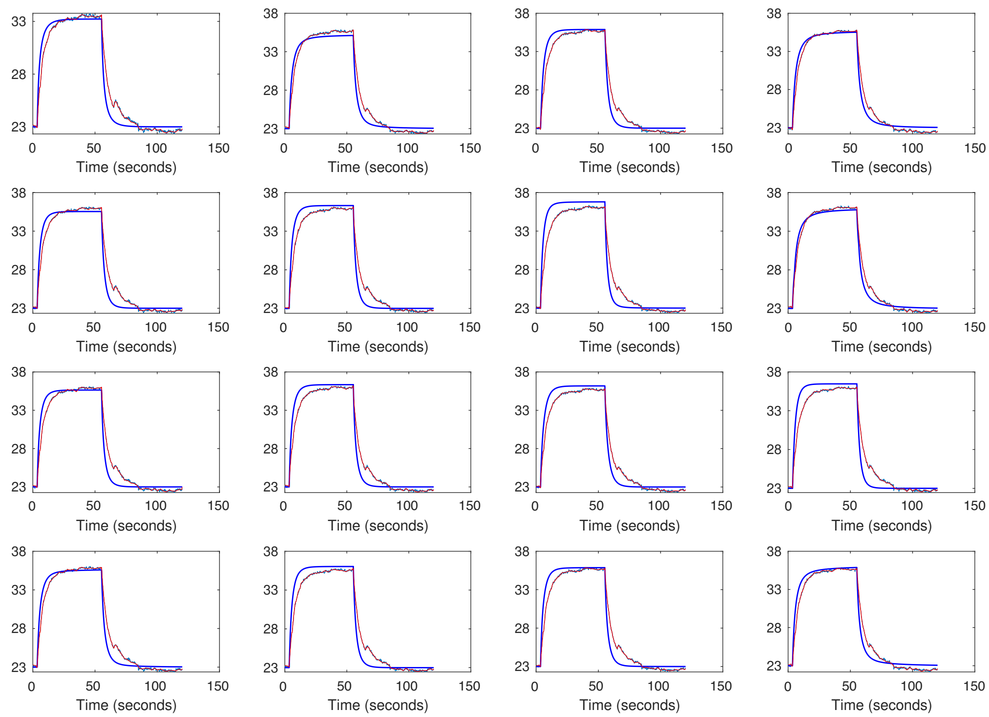

Figure 19. Validation of the system model

One example of a data-driven approach to dynamical systems is the Dynamic Data Driven Applications Systems (DDDAS) paradigm. DDDAS is a framework that dynamically couples high-dimensional physical and other analysis models and methods, run-time measurements, and computational architectures (Blasch et al., 2022). In this paradigm, the computation and instrumentation aspects of an application system are dynamically integrated in a feedback control loop, allowing instrumentation data to be dynamically incorporated into the executing model of the application and, in reverse, the executing model can control the instrumentation. Overall, Data-driven dynamical systems is an exciting field with many potential applications in science, engineering, and beyond. Using the power of data science and machine learning, researchers are developing new techniques to better understand and control complex dynamical systems.

In the case of multivariable thermal systems, its control is performed using PID, model predictive, and nonlinear strategies, among others (Su et al., 2020; Sun et al., 2020a; Kamesh & Rani, 2017; Chen

& Bai, 2021). Likewise, modeling and identification of multivariable thermal systems employ techniques such as spectral analysis, linear models, or machine learning (Pittino et al., 2020; Deng & Li, 2005; Diversi et al., 2020). It is important to note that in most of the control and identification techniques presented above, the system dimensions used to be 2×2 or 3×3.

However, for higher-order multivariable thermal systems with more complex analytical models (Viola et al., 2020), obtaining an accurate representation of the system based on the input-output data streams is required. In recent years, the Dynamic Mode Decomposition (DMD) (Brunton & Kutz, 2019) has relevance because it is a data-driven technique that allows one to obtain a representation of a complex system based only on input-output data without concern about the analytical model of the system. There are several modeling applications of DMD in the field of fluid dynamics (Sun et al., 2020a; Priyanga et al., 2019; Luong et al., 2021) with applications for thermal systems (Guida et al., 2021; Kanbur et al., 2020; Sun et al., 2020b), as well as others for system identification and control (Stevens et al., 2020) using a variant of DMD known as DMD with control or DMDc.

Dynamic Mode Decomposition is an algorithm developed to identify coherent spatio-temporal structures from high-dimensional data (Brunton & Kutz, 2019). DMD identifies the best-fit linear dynamical system based on a set of input-output data streams of a system, making DMD a data-driven technique.

3.2.2.1 Original DMD

Consider a dataset of m time snapshots denoted by $x(t_k), x(t'_k)_{k=1}^{m}$ where $t'_k = t_k + \Delta k$, and Δk is the sampling time. The data are stored in a matrix $X \in R^{n \times m-1}$ and X' is the shifting of X by one sampling time, which can be defined as (61) and (62),

$$X = \begin{bmatrix} | & | & & | \\ x(t_0) & x(t_1) & ... & x(t_{m-1}) \\ | & | & & | \end{bmatrix}, \tag{61}$$

$$X' = \begin{bmatrix} | & | & & | \\ x(t_1) & x(t_2) & ... & x(t_m) \\ | & | & & | \end{bmatrix}. \tag{62}$$

The DMD algorithm searches the eigenvalues and eigenvectors of the best-fit linear operator A that relates X and X' as:

$$X' \approx AX. \tag{63}$$

Thus, the best-fit operator A is defined as (64) where $X^\dagger$ is the matrix pseudoinverse,

$$A = X'X^\dagger. \tag{64}$$

According to (Brunton & Kutz, 2019), the best-fit operator A resembles the Koopman operator. Thus, DMD uses dimensionality reduction to compute the dominant eigenvalues and eigenvectors of A without directly requiring explicit computations of A. The DMD algorithm can be summarized as shown in Algorithm 2. As can be observed, $\tilde{A}$ is an approximation of A calculated based on the Singular Value Decomposition (SVD) of X, and which eigenvalues Λ correspond to the eigenvectors of the high-dimensional DMD modes Φ. When the dimensions of X and X' are high, its eigenvalues and eigenvectors can be truncated to improve the efficiency of the DMD algorithm.

3.2.2.2 DMD with control (DMDc)

Notice that the original DMD algorithm does not consider the effect of actuation on the system, which is essential for the identification and control of the control system. Therefore, (Brunton & Kutz, 2019) presents the so-called DMD algorithm with control or DMDc. This method, inspired by disease control problems, seeks to identify the best-fit linear operators A and B that satisfy the dynamics of the discrete domain (65).

$$x_{k+1} = Ax_k + Bu_k. \tag{65}$$

In addition to X and X', the actuation matrix Υ (66) is considered,

$$\Upsilon = \begin{bmatrix} | & | & & | \\ u(t_0) & u(t_1) & ... & u(t_{m-1}) \\ | & | & & | \end{bmatrix}, \tag{66}$$

which allows writing the system dynamics as (67),

$$X' = AX + B\Upsilon. \tag{67}$$

Assuming that A and B are unknown, X' can be calculated as (68) where the matrix $G = [A\ B]$ can be calculated as $G \approx X'\Omega^\dagger$, and $\Omega \triangleq [X\ \Upsilon]^T$. The DMDc algorithm is summarized in Algorithm 3. As can be observed, the SVD for Ω is calculated and $\tilde{U}^* = [\tilde{U_1}^* \ \tilde{U_2}^*]$ is separated in two matrices for X and Υ respectively.

$$X' \approx [A \ B] \begin{bmatrix} X \\ \Upsilon \end{bmatrix} = G\Omega. \tag{68}$$

Algorithm 2 Original DMD Algorithm

1: Calculate SVD $X \approx \tilde{U}\tilde{\Sigma}\tilde{V}^*$
2: Compute $\tilde{A} = \tilde{U}^* X' \tilde{V}' \tilde{\Sigma}^{-1}$
3: Obtain the eigenvalues Λ and eigenvectors W of A $\qquad \tilde{A}W = W\Lambda$
4: Determine high frequency modes $\Phi = X'\tilde{V}\tilde{\Sigma}^{-1}W$

The identification experiment was designed to capture the PHELP system dynamics and construct a model capable of representing and predicting the system's behavior. For this purpose, different Pseudo-Random Binary Signal (PRBS) were applied in the 16 inputs of the system, measuring the surface temperature with the thermal camera and an environmental temperature around the $29.84\ ^\circ C$.

Algorithm 3 DMDc Algorithm with B unknown

1: Construct X, X', Υ, and form $\Omega = [X^* \ \Upsilon^*]^*$
2: Calculate SVD $\Omega \approx \tilde{U}\tilde{\Sigma}\tilde{V}^*$
3: Calculate SVD $X' \approx \hat{U}\hat{\Sigma}\hat{V}^*$
4: Compute $\tilde{A} = \hat{U}^* X' \tilde{V}' \tilde{\Sigma}^{-1} \tilde{U}_1^* \hat{U} \qquad \tilde{B} = \tilde{U}^* X' \tilde{V}' \tilde{\Sigma}^{-1} \tilde{U}_2^*$
5: Calculate the eigenvalue decomposition of $\tilde{A} \qquad \tilde{A}W = W\Lambda$
6: Get high frequency modes $\Phi = X'\tilde{V}\tilde{\Sigma}^{-1}\tilde{U}_1^*\hat{U}W$

Figure 20 shows the identification data acquired during the heating cycle. The same procedure is applied for the cooling, inverting the power source sign, and obtaining the dynamic in both cycles due to the system's nonlinear behavior. For each cycle, a pair of data is captured to identify and validate the model. Thus, the final model of the PHELP system is shown in Figure 21, which combines the heating and cooling cycles.

The DMDc Algorithm 3 seeks to identify the best-fit linear MIMO model of the PHELP system. However, if the system presents noise in the data, a direct shift of the vector X does not give a proper signal derivative. In this case, instead of using (62), X' was calculated using a fourth-order approximation of the derivative (69),

$$X'(i) = \frac{1}{12}\left(-X(i+2) + 8X(i+1) - 8X(i-1) + X(i-2)\right). \tag{69}$$

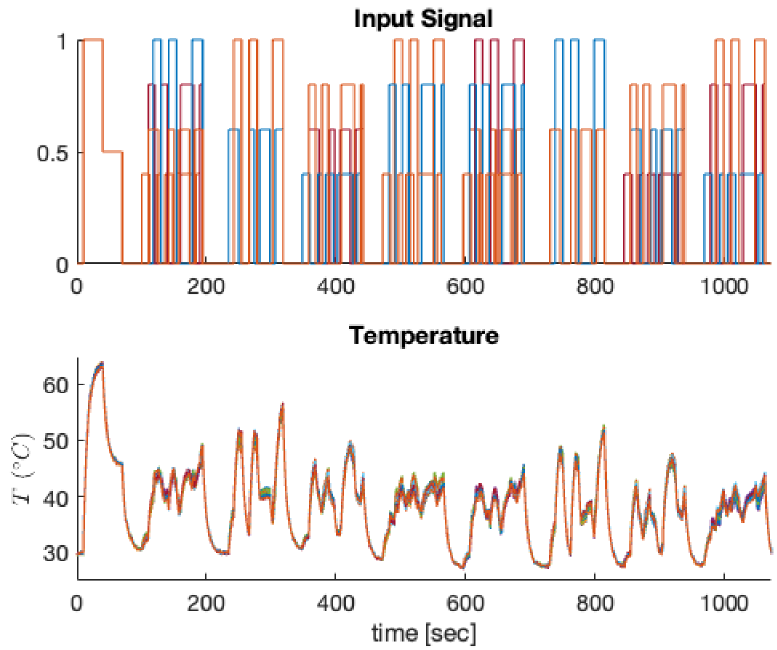

Figure 20. PHELP identification data using data-driven technique

Following the DMDc Algorithm 3 steps, the PHELP heating and cooling processes are characterized by a MIMO model, obtaining a square A and B matrix, on page 101 with a patron where the control signals affect the dynamic of the system by quadruple (1-3-5-9,2-8-12-15,6-10-13-16,4-7-11-14), see Figure 11. This solution suggests an increased complexity in designing the control algorithm due to the high-order transfer function of the system.

The results are shown in Figures 22 and 23 with an NRMSE fitness value (70) of 92.74% and 90.30% for the heating and cooling process, respectively. The mean error is around $0.5\ {}^{\circ}C$ in both cases, related to the thermal camera resolution due to the sensor introducing an error of $\pm 0.5\ {}^{\circ}C$. The obtained matrices A, B are shown in Appendix A.

$$\text{FIT} = 100 \times \left(1 - \frac{||y_{out} - y_{model}||}{||y_{out} - \bar{y}||}\right) \tag{70}$$

One of the fundamental characteristics of multivariable control is the effect of coupling and interaction between individual loops. Therefore, eliminating such effects inherently depends on the adequate design of the control system. Thus, the use of decoupling techniques represents an essential alternative. Nevertheless, applying a decoupling for this system may be impractical. Therefore, a scalar matrix B was designed to reduce the high order of the transfer function of the system. Thus, with the proposed B, a new matrix A can be calculated using the DMDc Algorithm 4, which is a modification of the DMDc

Algorithm 3 when B is known.

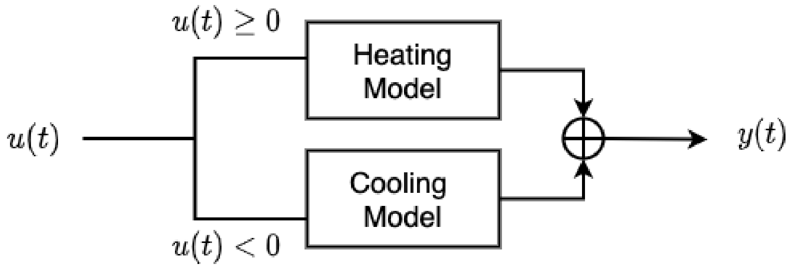

Figure 21. Heating/Cooling model of the PHELP system

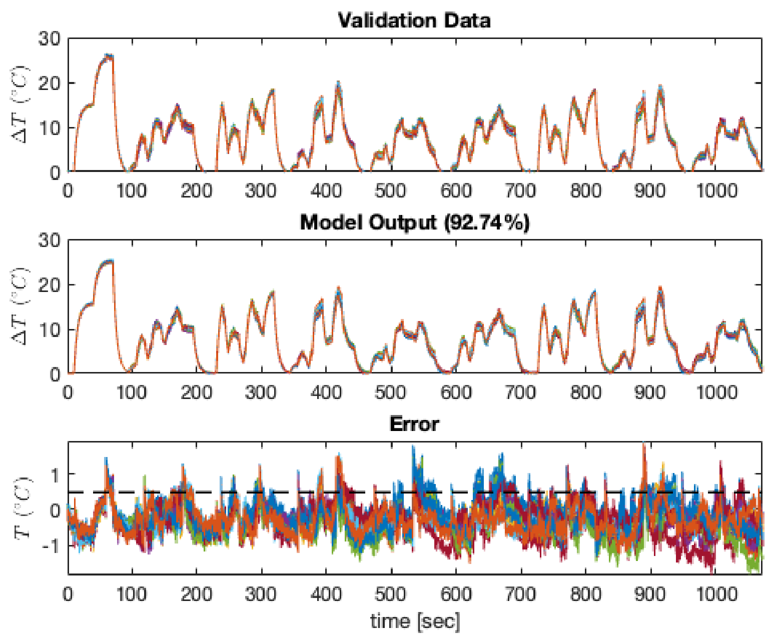

Figure 22. Validation of the model for the heating process with matrix B unknown

From the matrix B calculated using Algorithm 3 the maximum eigenvalues $\lambda_{heat} = 0.59$ and $\lambda_{cool} = 0.28$ were selected as the initial value of the new scalar matrix B until finding the value that provides the best fit to the model. The proposed scalar matrix B for heating and cooling is given by (71), which assumes that all Peltier provide the same heat flux to the system. The DMDc using a known B is defined by Algorithm 4.

$$B_{heat} = \begin{bmatrix} 0.52 & & \\ & \ddots & \\ & & 0.52 \end{bmatrix}, \quad B_{cool} = \begin{bmatrix} 0.27 & & \\ & \ddots & \\ & & 0.27 \end{bmatrix}. \tag{71}$$

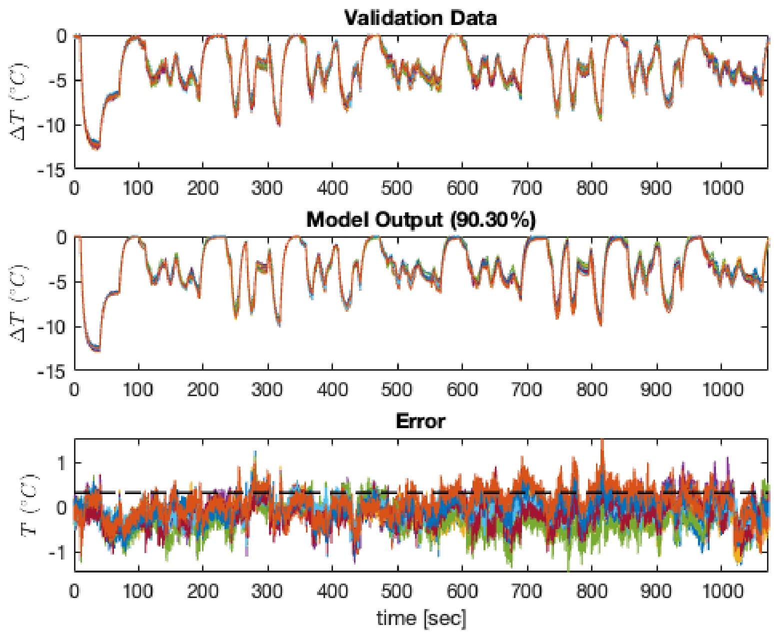

Figure 23. Validation of the model for the cooling process with matrix B unknown

Algorithm 4 DMDc Algorithm with matrix B know

1: Construct X, X', Υ, and form $\Omega = [X^* \ \Upsilon^*]^*$
2: Calculate SVD $\Omega \approx \tilde{U}\tilde{\Sigma}\tilde{V}^*$
3: Compute $\tilde{A} = \hat{U}^* \left(X' - B\Upsilon\right) \tilde{V}'\tilde{\Sigma}^{-1}$
4: Calculate the decomposition of the eigenvalue of $\tilde{A}$
$\tilde{A}W = W\Lambda$
5: Get high frequency modes $\Phi = \left(X' - B\Upsilon\right) \tilde{V}\tilde{\Sigma}^{-1}W$

The results of DMDc using Algorithm 4 are shown in Figure 24 and 25, depicting a good fitness for heating and cooling processes. Therefore, the simplest models of each process are defined by (72) and (73) with $C = \mathcal{I}^{16\times16}$ and $D = 0^{16\times16}$.

$$\begin{aligned} \dot{x} &= A_{heat}x + B_{heat}u, \\ y &= Cx + Du, \end{aligned} \tag{72}$$

$$\begin{aligned} \dot{x} &= A_{cool}x + B_{cool}u, \\ y &= Cx + Du. \end{aligned} \tag{73}$$

In the subsequent section, following the favorable outcomes obtained from the fractional-order transfer function matrix modeling and data-driven techniques, our focus shifts towards formulating a control algorithm to successfully maintain a uniform temperature on the surface, controlling the heat in each

Peltier.

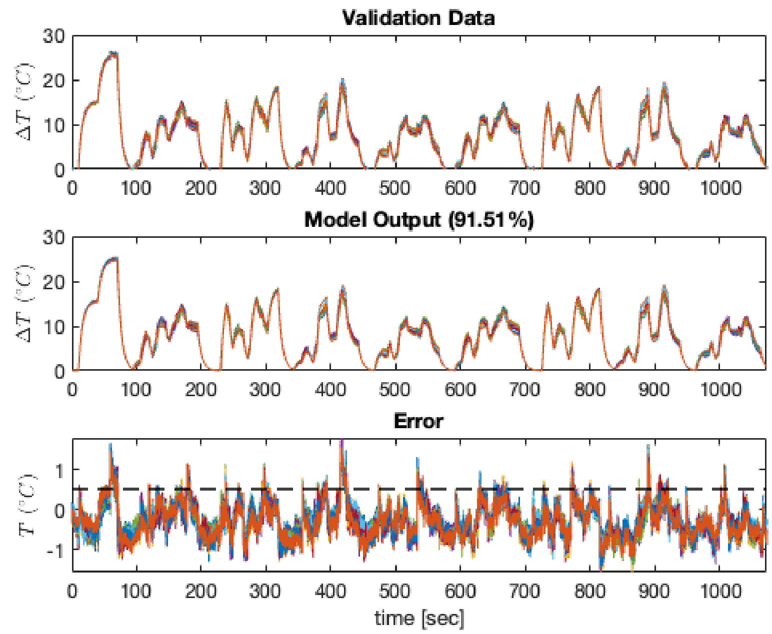

Figure 24. Validation of the model for the heating process with matrix B known

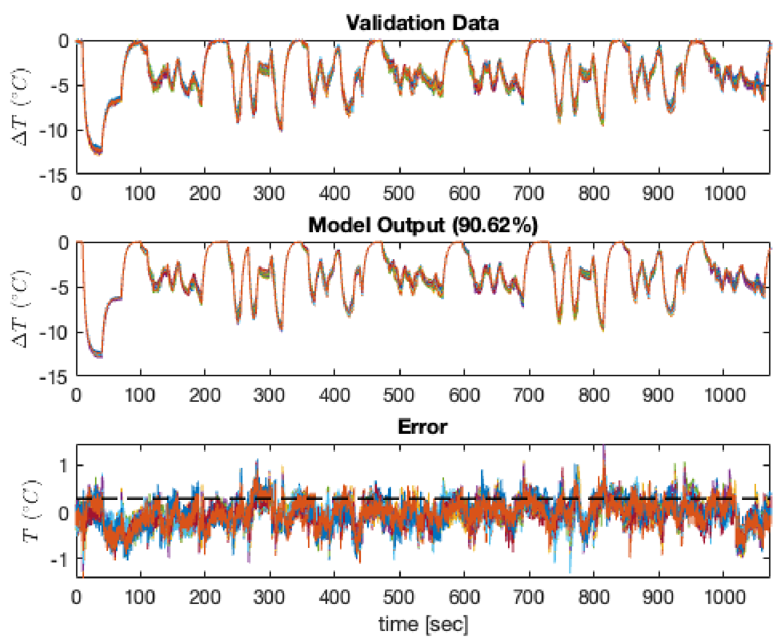

Figure 25. Validation of the model for the cooling process with matrix B known

3.3 Controller design

This section will cover the controller design for the fractional-order transfer function matrix and the data-driven model of the PHELP. A decentralized Proportional-Integral (PI) control strategy is used to control the temperature in the PHELP system, based on the fractional-order transfer function model. Thus, the FOPDT models of the main diagonal of the transfer function matrix (57) are used for controller design using the parameters in Table 3. An optimal PI tuning algorithm (Monje et al., 2010) is employed to find the gains of the PI controller. It requires a Linear Time-Invariant (LTI) integer or fractional-order transfer function of the system $G_p(s)$ and the controller transfer function $G_c(s)$, which must satisfy the following specifications:

- Phase margin (pm):
$$arctan(G_c(jw)G_p(jw)) = -\pi + pm \tag{74}$$
- Gain crossover frequency(w_c):
$$|G_c(s)G_p(s)| = 0\ dB \tag{75}$$
- Robustness against variation of plant gain:
$$\frac{d}{dw}arctan(G_c(jw)G_p(jw)) = 0 \tag{76}$$
- Rejection of high-frequency noise:
$$\left|\frac{G_c(jw)G_p(jw)}{1 + G_c(jw)G_p(jw)}\right| = B\ dB \tag{77}$$
- Rejection of output disturbances:
$$\left|\frac{1}{1 + G_c(jw)G_p(jw)}\right| = A\ dB \tag{78}$$

The Fractional Order Modeling and Control Toolbox (FOMCON) for MATLAB is a fractional-order calculus-based toolbox for system modeling and control design. The core of the toolbox is derived from an existing toolbox FOTF ("Fractional-order Transfer Functions") (Tepljakov, 2017). FOMCON is related to other existing fractional-order calculus-oriented MATLAB toolboxes, such as CRONE (Oustaloup et al., 2000) and Ninteger (Duarte, 2023) through either system model conversion features or shared code, and this relation is depicted in Figure 26. In addition, its modular structure is shown in Figure 27

(Tepljakov, 2017).

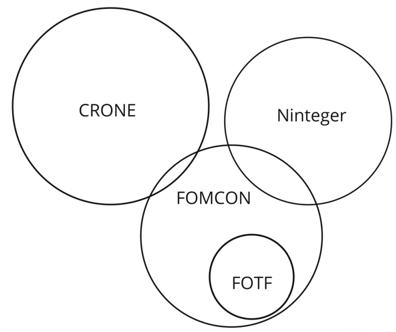

Figure 26. Relation of FOMCON toolbox to similar packages

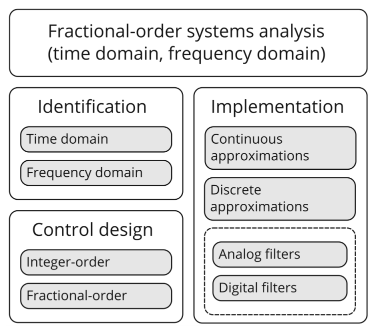

Figure 27. Modular structure of the FOMCON toolbox

The Matlab FOMCON Toolbox is employed to solve the optimal control problem to find the values of K and T_i using the PI controller form (79). Thus, the desired system performance specifications are given in terms of gain margin and phase margin using the Integral of Time multiplied by Absolute Error (ITAE) criterion as the optimization criterion. For these models, a phase margin $PM = 60° - 65°$, and a gain margin $GM = 10 - 15\,dB$ are used, and the parameters obtained from the PI controllers are shown in Table 5.

$$PI(s) = K\left(1 + \frac{1}{T_i s}\right) = K + \frac{I}{s}. \tag{79}$$

Figures 28 and Figure 29 show the time response and control action of the system for a change in the reference around ($13\,°$C). As can be observed, the decentralized PI controllers reach the desired setpoint with uniformity in the control signal, allowing a suitable thermal performance on the surface to avoid wear of the material and prolong the life cycle of the Peltier. At a time of 106 seconds, the thermal camera applies a perturbation in the control system due to the thermal camera presenting an error of $\pm 0.5\,°$C, and every certain time it performs an adjustment of the image quality, changing the measured value markedly.

Table 5. Decentralized PI controller parameters

	PI_1	PI_2	PI_3	PI_4	PI_5	PI_6	PI_7	PI_8
K	65.73	83.33	83.33	83.33	83.33	83.33	83.33	83.33
I	1.17	2.01	2.44	2.83	1.5	1.5	1.5	1.5
	PI_9	PI_{10}	PI_{11}	PI_{12}	PI_{13}	PI_{14}	PI_{15}	PI_{16}
K	83.33	68.57	83.33	83.33	83.33	83.33	83.33	83.33
I	1.5	1.23	3.34	2.35	1.5	1.5	1.5	4.45

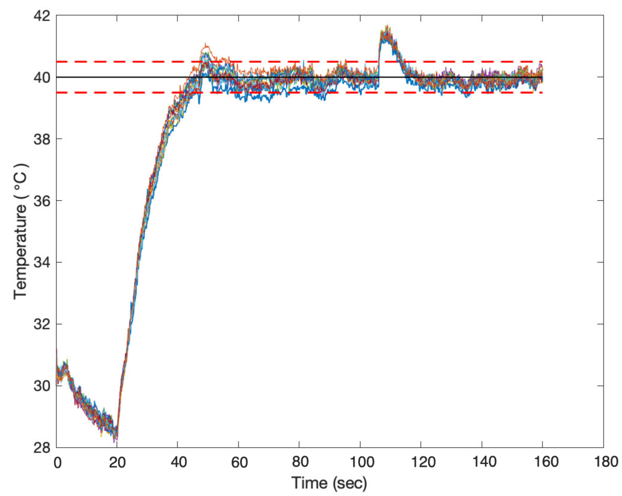

Figure 28. PHELP system step response with PI controllers

The controller's effectiveness in stabilizing the heat output of each Peltier device has led to a notable improvement in temperature uniformity across the surface. As depicted in Figure 29, variations in the control signals of individual elements are apparent. These variations arise from the unique characteristics of each element and their distinct contributions to the overall surface temperature.

The dynamic of the control signals can be attributed to the intricate interplay between the Peltier devices. Each device responds differently to the control algorithm due to inherent differences in material properties and thermal behavior. Consequently, the control algorithm orchestrates a consensus of these diverse responses, culminating in the observed temperature uniformity.

In summation, the results showcased in Figure 29 highlight the good results in the modeling and control of the PHELP using fractional-order systems and its control methods.

Considering the state-space modeling setup of the PHELP system, a control strategy combining ν-gap metric and Linear Quadratic Regulator (LQR) is proposed to reach a uniformity temperature control. The Vinnicombe gap (ν-gap) (80) is a metric introduced in (Vinnicombe, 1993) and measures the distance between systems in terms of how their differences can affect closed-loop behavior.

$$\delta_\nu\left(P_0, P_1\right) := \begin{cases} \left\| \left(I + P_1 P_1^*\right)^{-1/2} \left(P_1 - P_0\right) \left(I + P_0^* P_0\right)^{-1/2} \right\|_\infty, \\ \quad \text{if } \eta\left[P_1, -P_0^*\right] = \eta\left[P_0, -P_0^*\right] \\ 1, \quad \text{otherwise} \end{cases} \tag{80}$$

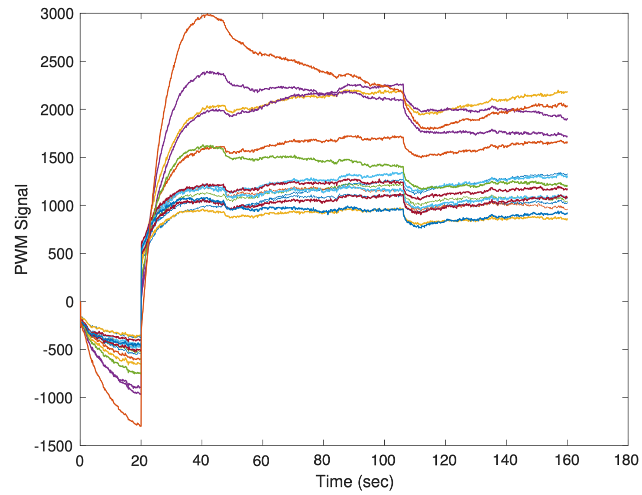

Figure 29. PHELP system control action for PI controllers

In general, if the ν-gap distance between two plants is small then any controller which performs well with one plant will also perform well with the other. Assuming the linear time-invariant state-space model for heating and cooling given by (72) and (73), a cost function (81) is used to minimize the input signal u(t), where Q and R are the weighting matrices for the states and inputs, respectively, and $u^*(t) = -Kx(t)$ with $K = R^{-1}B^T P$.

$$J = \frac{1}{2}\int_{t_0}^{t_f} \left[x^T(t)Qx(t) + u^T(t)Ru(t)\right] dt. \tag{81}$$

With the closed-loop state space equations under state feedback (82) where $\theta = heat, cool$ process, the closed-loop control diagram for multiple linear models is given by Figure 30.

$$\begin{aligned} \dot{x}_\theta &= \left(A_\theta - B_\theta K_\theta\right) x_\theta + B_\theta v(t), \\ y_\theta &= \left(C - DK_\theta\right) x_\theta + Dv(t). \end{aligned} \tag{82}$$

In this case, for the PHELP system, a linearized transfer function of different equilibrium points over the operating range can be approximated by taking the Taylor series expansion. Thus, an optimal robust controller is designed for each nominal linear model, making every closed-loop linear system have the largest generalized stability margin (Yubo et al., 2013).

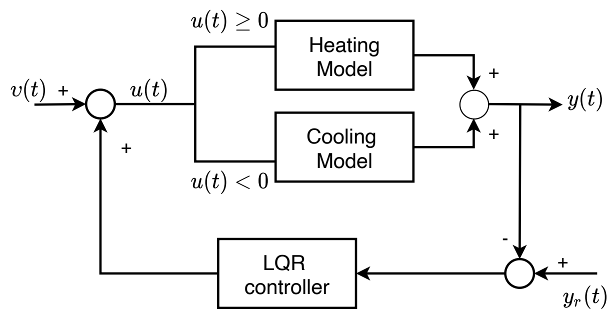

Figure 30. State feedback of the PHELP system

Thus, considering a set of m local controllers, the global output of the controller is given by (83), where $u_i(t)$ is the output of the $i-th$ local controller C_i for the P_i model, and the $w_i(t)$ is the weight coefficient, calculated by (Georgiou & Smith, 1990) using (84). Because $0 \leq \nu$-gap $\leq$ gap ≤ 1, the ν-gap can provide a more stringent test for robustness. For both metrics, the robust performance (85) result holds.

$$u(t) = \sum_{i=1}^{m} w_i(t) u_i(t), \tag{83}$$

$$w_i = \frac{b_{P_i,C_i}}{\sum_{j=1}^{m} b_{P_j,C_j}}, \qquad i = 1, 2, \ldots, m, \tag{84}$$

$$b_{P_i,C_i} \triangleq \left\| \begin{pmatrix} I \\ P \end{pmatrix} (I - CP)^{-1} \begin{pmatrix} I & C \end{pmatrix} \right\|_{\infty.}^{-1} \tag{85}$$

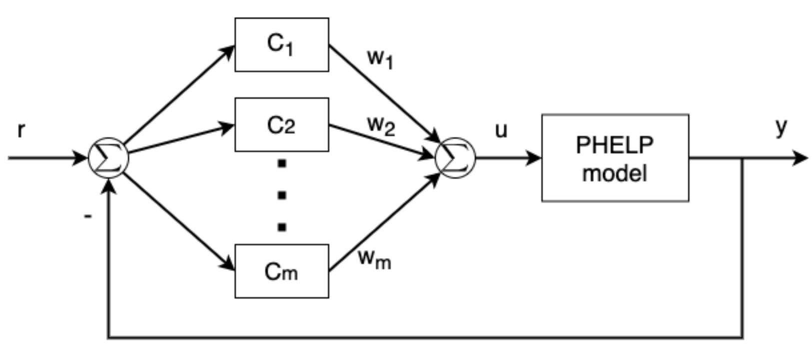

Figure 31. Structure of multi-model control system

The multi-model control system structure is depicted in Figure 31, selecting the Q and R matrices for the controllers as (86), with the weights (87).

$$Q = \begin{bmatrix} 0.8 & & \\ & \ddots & \\ & & 0.8 \end{bmatrix}, \quad R = \begin{bmatrix} 0.1 & & \\ & \ddots & \\ & & 0.1 \end{bmatrix}, \tag{86}$$

$$w_{heat} = 0.4974, \quad w_{cool} = 0.5026. \tag{87}$$

A numerical simulation study for the PHELP system model identified using DMDc controlled by the LQR controller with and without the ν-gap metric analysis is shown in Figures 32 and 33 with a sampling time of 1 second. For the case without the ν-gap metric, the controller was designed using the heating model of the system. Figure 32 shows the response to system time, which has a good performance of both controllers. However, the controller with the ν-gap metric presents a lower control effort with a maximum RMS value of 0.7368 and more uniformity than the w/o ν-gap metric, helping to a more efficient system and delay the aging of the system; see Figure 33.

Finally, the LQR controller with the ν-gap metric was implemented in the real system, with the Arduino Board as Hardware in the Loop (HIL) as presented in Figure 13.

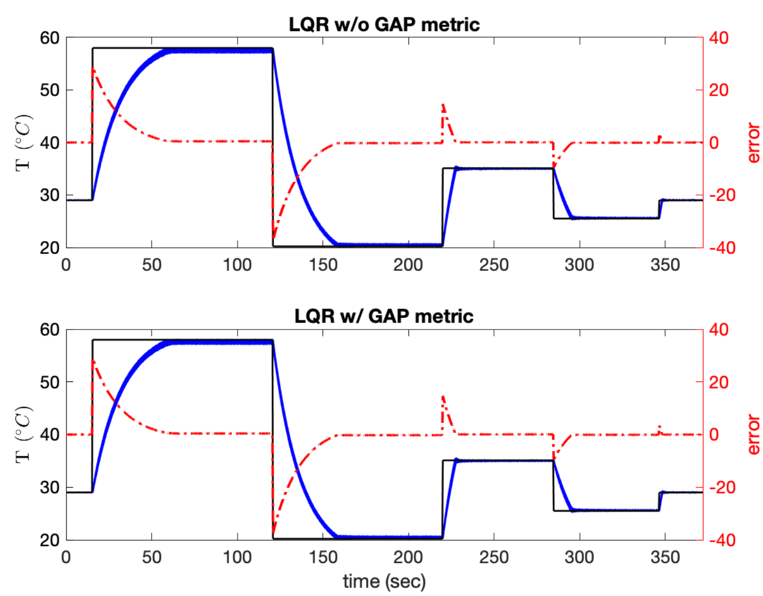

Figure 32. Output of the PHELP system controlled by the LQR controller w/o & w/ ν-gap metric

A video of the real experiment is available at (Rodriguez, 2021), where three scopes show the response of the real system (left), the control signal (middle), and the output of the DMDc model (right). Figure

34 shows the responses of the real experiment showing an error bounded by $|e(t)| \leq 2\,°C$ and a maximum RMS value of $0.533\ °C$. Therefore, it is possible to say that using the DMDc to identify a high-order system allows determining the system dynamics with high accuracy. Additionally, knowing the B matrix can reduce the complexity of the model and improve the closed-loop control response.

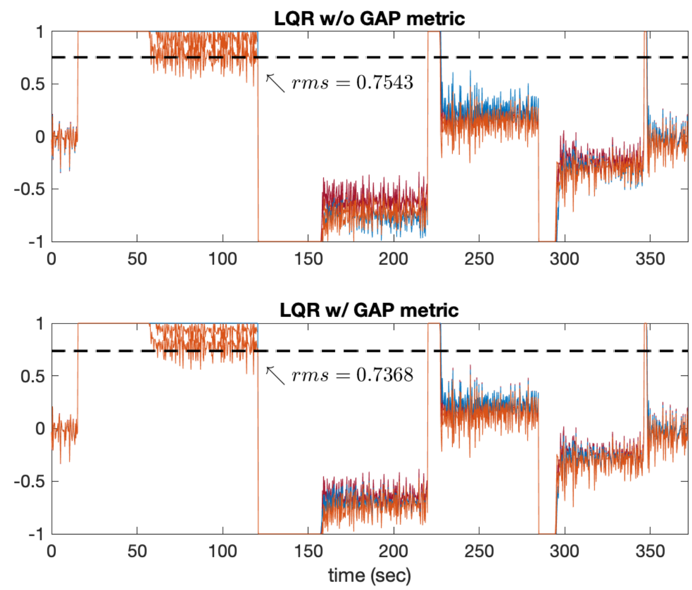

Figure 33. Control signal of the LQR controller w/o & w/ ν-gap metric

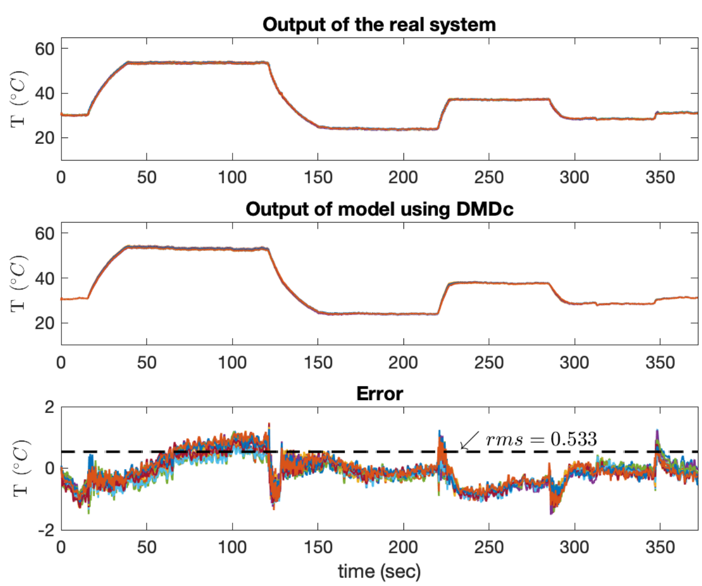

Figure 34. Comparison of the real system and model using DMDc

3.4 Digital Twins

Artificial intelligence (AI) was officially declared a research field, and no one would have ever predicted the huge influence and impact its description, prediction, and prescription capabilities would have on our daily lives. In parallel to continuous advances in AI, the past decade has seen the spread of broadband and ubiquitous connectivity, (embedded) sensors collecting descriptive high dimensional data, and improvements in big data processing techniques and cloud computing.

The joint usage of such technologies has led to the creation of digital twins, artificial intelligent virtual replicas of physical systems. Digital Twin (DT) technology is being developed and commercialized to optimize several manufacturing and aviation processes, while in the healthcare and medicine fields, this technology is still at its early development stage, (Barricelli et al., 2019).

A DT is a virtual representation of a real-world object, system, process, or entity created through the integration of data from various sources, such as sensors, simulations, and historical records. This digital counterpart mirrors the physical entity in a digital environment, allowing real-time monitoring, analysis, and interaction. This concept and many others can be found in the literature. The evolution of the DT concepts started by **(Grieves, 2015)**: *"DT is a virtual, digital equivalent to a physical product."*, later **NASA**: *"an integrated Multiphysics, multiscale, probabilistic simulation of an as-built vehicle or system that uses the best available physical models, sensor updates, fleet history, etc., to mirror the life of its corresponding flying twin"*, continues **(Tao & Qi, 2019)**: *"DT are precise, virtual copies of machines or systems driven by data collected from sensors in real-time; these sophisticated computer models mirror almost every facet of a product, process or service."*. However, we use the definition given by **MESA Lab, UC Merced**: *"A Digital Twin is the combination of multiple, individual and detailed simulation models (continuous, discrete, hybrid), where its interconnection represents the dynamics of a complex system, which is periodically updated (windowed or real-time) with system information to reflect system current status as well as predict future behavior and possible faults."*

The main concept of the DT is to bridge the gap between the digital and physical worlds. This will enable organizations to optimize processes, achieve deep insight into each step, and make efficient decisions.

The power of data analytics, AI, and the Internet of Things (IoT) allow DT to offer a more complete model usable in various industries, like healthcare, manufacturing, aerospace, and more. Some features of the DT are Realizability, Real-time system data updating, Behavioral Matching, Modular structure, Trackability, and Reprogramability, and its key characteristics include Real-time Monitoring, Simulation, and Analysis, Predictive Maintenance, Lifecycle Management, Informed Decision-making, and Collaboration.

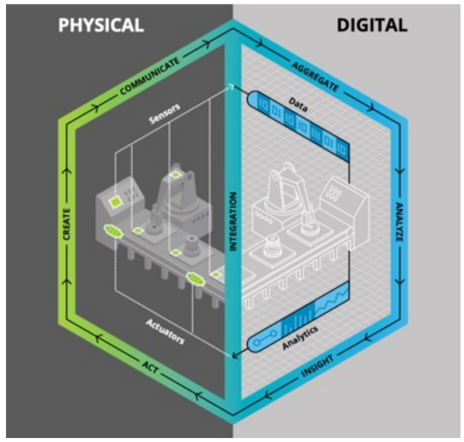

Figure 35. Physical and digital components of Digital Twins

As the technology behind Digital Twins continues to advance, the potential applications are expanding, and the concept is becoming a driving force for innovation and efficiency across industries. Although challenges related to data security, interoperability, and scalability must be addressed, the promise of improved performance, reduced costs, and enhanced sustainability make the adoption of Digital Twins an increasingly attractive proposition for forward-thinking organizations. More information can be found in (Jain et al., 2019; Farsi et al., 2020; Qi et al., 2019; Madni et al., 2019; Qi & Tao, 2018; Viola & Chen, 2023).

Figure 35 illustrates a DT's components based on the system's environment. The physical aspect encompasses sensors responsible for collecting operational and environmental data from the physical system to fuel the DT. Additionally, actuators play a role in translating analytical results into tangible signals that the system can comprehend. On the other hand, digital components comprise real-time and historical data, which serve as inputs for both simulation models and analytics. These simulations are constructed using multidomain models, while analytics encompasses various techniques for data analysis, visualization, and generating insights regarding the behavior of both the DT and the real-world system.

The virtual representation of a real system can be defined in four levels. Each level has a specific purpose and scope and helps with decision-making and answering questions throughout the life cycle of the system. Table 6 presents these different levels along with the characteristics that define each level (Madni et al., 2019).

An approach to a Peltier DT is developed to describe the dynamic of the component and predict its behavior and aging during time, for a more accurate model of the PHELP platform. Based on data-driven techniques as used to model the thermal system, but in this case, using Sparse Identification of Nonlinear Dynamics (SINDy).

Table 6. Digital Twin levels.

Level	**Model Sophistication**	**Physical Twin**	**Data Acquisition from Physical Twin**	**Mahine Learning (Operator Preferences)**	**Machine Learning (System / Environment)**
1. Pre-Digital Twin	virtual system model with emphasis on technology / technical-risk mitigation	does not exist	Not applicable	No	No
2. Digital Twin	virtual system model of the physical twin	exists	performance, health status, maintenance, batch updates	No	No
3. Adaptive Digital Twin	virtual system model of the physical twin with adaptive UI	exists	performance, health status, maintenance, real-time updates	Yes	No
4. Intelligent Digital Twin	virtual system model of the physical twin with adaptive UI and reinforcement learning	exists	performance, health status, maintenance, environment, both batch / real-time updates	Yes	Yes

SINDy is a data-driven algorithm for obtaining dynamical systems from data. Given a series of snapshots of a dynamical system and its corresponding time derivatives, SINDy performs a sparsity-promoting regression (such as LASSO) on a library of nonlinear candidate functions of the snapshots against the derivatives to find the governing equations. This procedure relies on the assumption that most physical systems only have a few dominant terms which dictate the dynamics, given an appropriately selected coordinate system and quality training data. It has been applied to identify fluid dynamics, based on proper orthogonal decomposition, as well as other complex dynamical systems, such as biological networks (Brunton et al., 2016).

Generically, we seek to represent the system as a nonlinear dynamical system

$$\dot{x}(t) = f(x(t)). \tag{88}$$

The vector $x(t) = [x_1(t)\ x_2(t) \dots x_n(t)]^T \in \mathbb{R}^n$ represents the state of the system at time t, and the nonlinear function $f(x(t))$ represents the dynamic constraints that define the equations of motion of the system. To determine the form of the function f from the data, we collect a time history of the state

$x(t)$ and its derivative $\dot{x}(t)$ sampled at a number of instances in time $t_1, t_2, \ldots, t_m$. These data are then arranged into two large matrices:

$$X = \begin{bmatrix} x^T(t_1) \\ x^T(t_2) \\ \vdots \\ x^T(t_m) \end{bmatrix} = \begin{bmatrix} x_1(t_1) & x_2(t_1) & \cdots & x_n(t_1) \\ x_1(t_2) & x_2(t_2) & \cdots & x_n(t_2) \\ \vdots & \vdots & \ddots & \vdots \\ x_1(t_m) & x_2(t_m) & \cdots & x_n(t_m) \end{bmatrix} \tag{89}$$

where the columns represent the states of the system and the rows the time, and the derivative

$$\dot{X} = \begin{bmatrix} \dot{x}^T(t_1) \\ \dot{x}^T(t_2) \\ \vdots \\ \dot{x}^T(t_m) \end{bmatrix} = \begin{bmatrix} \dot{x}_1(t_1) & \dot{x}_2(t_1) & \cdots & \dot{x}_n(t_1) \\ \dot{x}_1(t_2) & \dot{x}_2(t_2) & \cdots & \dot{x}_n(t_2) \\ \vdots & \vdots & \ddots & \vdots \\ \dot{x}_1(t_m) & \dot{x}_2(t_m) & \cdots & \dot{x}_n(t_m) \end{bmatrix}. \tag{90}$$

Next, we construct an augmented library $\Theta(X)$ consisting of candidate nonlinear functions of the columns of X. For example, $\Theta(X)$ may consist of constant, polynomial and trigonometric terms:

$$\Theta(X) = \begin{bmatrix} | & | & | & | & & | & | & | & | & \\ 1 & X & X^{P_2} & X^{P_3} & \cdots & \sin(X) & \cos(X) & \sin(2X) & \cos(2X) & \cdots \\ | & | & | & | & & | & | & | & | & \end{bmatrix}. \tag{91}$$

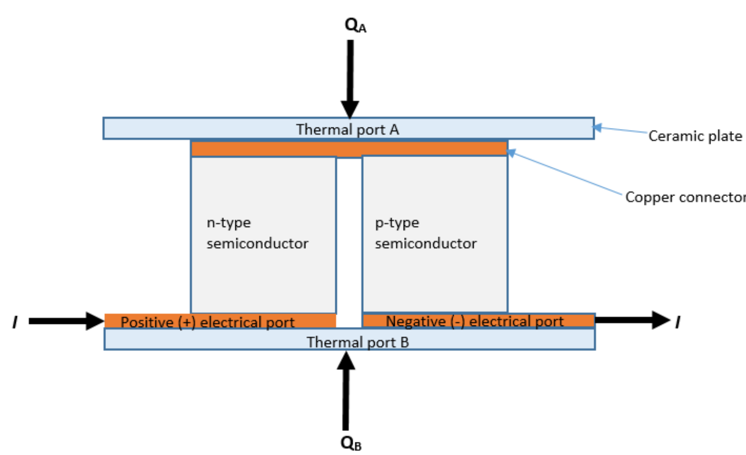

Figure 36. Peltier device block

For the Peltier nonlinear dynamics, its known that the dynamic is represented by the following equations

$$Q_A = \alpha T_A I - \frac{1}{2} I^2 R + K\left(T_A - T_B\right) \tag{92}$$

$$Q_B = -\alpha T_B I - \frac{1}{2} I^2 R + K\left(T_B - T_A\right) \tag{93}$$

$$W = VI \tag{94}$$

where Q_A is heat flow into port A, Q_B is heat flow into port B, T_A is port A temperature, T_B is port B temperature, W is electrical power (positive when flowing into the block), V is potential difference across the + and - ports, I is electrical current, positive from + to - port, R is total electrical resistance, α is Seebeck coefficient, K is thermal conductance, see Figure 36. Based on (94) the $\Theta(x)$ augmented library proposed

$$\Theta(x) = \begin{bmatrix} 1 & x & u & x^2 & xu & u^2 \end{bmatrix} \tag{95}$$

was used to find the coefficients and achieve a good fit with the real data. In Figure 37, a comparison between the model obtained by sparse identification with real data shows the effectiveness of the tool.

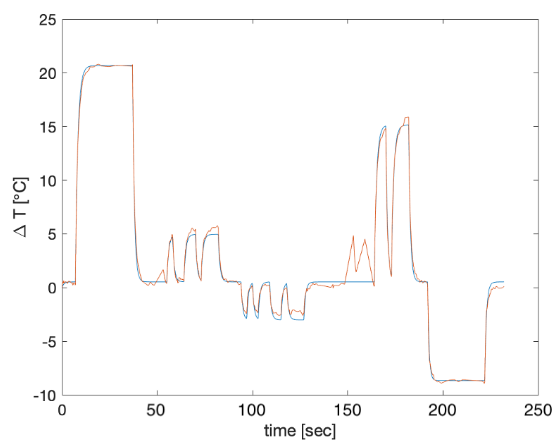

Figure 37. Fitting of sparse-identification model (red) with real data (blue).

As mentioned, Dynamic Targeting (DT) can be constructed using multidomain models. Another approach that was tested involves the use of Simscape modeling in MATLAB. Simscape enables the rapid creation of models for physical systems within the Simulink environment. With Simscape, the physical component models are based on physical connections that integrate directly with block diagrams and other modeling paradigms, allowing the construction of system models such as electric motors, bridge rectifiers, hydraulic actuators, and refrigeration systems. This is achieved by assembling fundamental components into a schematic.

Figure 38 shows the design of the Peltier device in the Simscape environment. With the acquisition of real data, Figure 39, and with the Simulink Design Optimization toolbox, the estimation of the parameters α, R, K, and c from (94) continued.

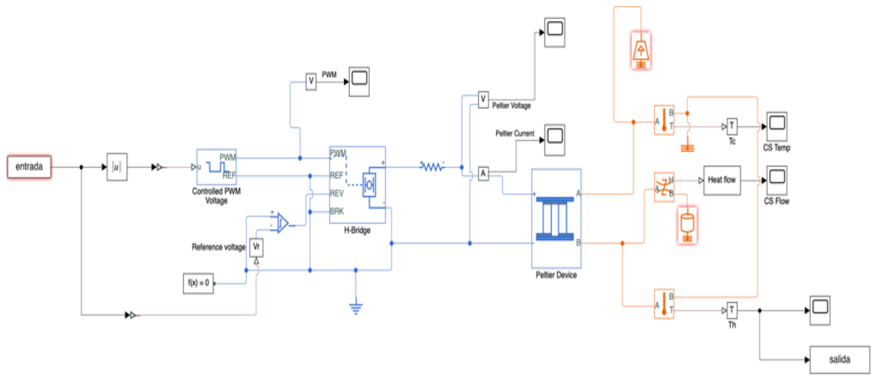

Figure 38. Simscape model of the Peltier device

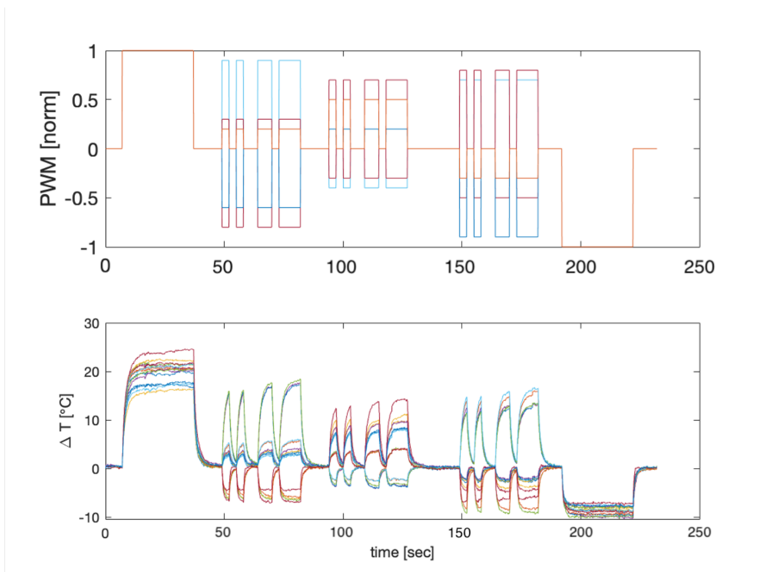

Figure 39. Peltier identification data to determine the Simscape coefficients.

Table 7 shows the value of each coefficient for the 16 Peltiers. These two approaches for obtaining a model of the Peltier device can be used to describe its dynamic behavior and test different scenarios that may be impractical to conduct with the physical component. However, they could prove useful for predicting the future response of these devices and aging under different conditions.

3.5 Conclusions

Thermal systems are a very important topic nowadays because of their significance in manufacturing, energy management, and environmental sustainability. Combining fractional-order transfer functions and data-driven techniques, analysis, prediction, and optimization of thermal behavior become more precise and adaptable to the physical world.

Table 7. Coefficients of the Simscape Peltier model

Peltier	R	c	α	K
1	0.3973	466.0200	0.0022	0.0503
2	0.4667	477.0300	0.0021	0.0437
3	0.3888	510.6400	0.0021	0.0536
4	0.4926	572.8300	0.0025	0.0498
5	0.4714	465.2300	0.0025	0.0517
6	0.4764	562.3700	0.0022	0.0509
7	0.4601	462.8900	0.0021	0.0445
8	0.3975	497.2300	0.0022	0.0470
9	0.4178	427.9400	0.0021	0.0451
10	0.4135	462.5100	0.0018	0.0394
11	0.4382	490.4690	0.0022	0.0476
12	0.4054	489.7700	0.0018	0.0426
13	0.3792	470.6800	0.0017	0.0416
14	0.3821	472.5800	0.0018	0.0412
15	0.3947	310.1800	0.0014	0.0321
16	0.3303	451.9900	0.0016	0.0393

Fractional-order differential equations allow a more precise dynamic representation of physical systems, such as thermal systems, with a more accurate representation of heat conduction, convection, and radiation, often encountered in the real world. By embracing fractional-order modeling, engineers and researchers can uncover hidden insights, optimize system designs, and improve thermal efficiency.

Using DMD, linear and nonlinear models with high accuracy were obtained from the data set. Based on large data sets, this technique makes it possible to identify patterns, correlations, and nonlinear relationships that could be difficult to capture using traditional analytical methods. The results demonstrate its efficiency in obtaining high-order models, such as, for example, the 16x16 temperature system using Peltier elements, as well as the modeling of this nonlinear element coinciding with the model obtained with the analytical one.

Fractional order systems and data-driven techniques make it possible to model thermal systems with greater precision, allowing them to be designed, controlled, and optimized efficiently.

Chapter 4. Radio frequency impedance matching based on control Lyapunov function

4.1 Introduction

Impedance matching is significant in radio frequency (RF) circuit design. It involves the design of a circuit to be inserted between the source and the load to achieve maximum power transfer. Impedance matching is not always about maximum power transfer; it can trade off gain requirements, bandwidth, and noise in wideband and low-noise amplifiers. To maximize the power delivery of the RF power system, the input impedance of the load must be matched to the output impedance of the RF generator and the transmission line, which has a characteristic impedance of 50 Ω.

Wireless communication, radar, satellite communication, plasma generation, and radio broadcasting systems are applications where impedance matching is essential. For our purpose, we focused on the plasma etching process for semiconductor fabrication. With RF impedance matching helping in the etching process, a proper match of the network impedance allows a stable plasma, creating uniformity in the etching process and an etch rate control crucial for achieving the desired dimensions and profiles in semiconductor devices. Also, other characteristics of the process can be achieved, process stability and reliability, damage and contamination reduction, enhanced equipment efficiency, process consistency, and yield and time-cost savings.

In the following sections, we present the state of the art research within this field. In addition, new control approaches are proposed to enhance the effectiveness of minimizing the reflected power of the system and reducing the tuning time.

4.2 State of art of radio-frequency impedance matching control

From our knowledge, (Mazza, 1970) is the first work on automatic impedance matching networks; see Figure 40. The author establishes that the impedance being monitored is that of the matching network and sputtering system combined, and the DC output signals of the VI probe are used with servo-amplifiers to adjust the matching network. It also reveals three interrelated problems that should be considered before the output signals can be used to adjust the matching network:

1. Adjustments of the shunt and series capacitances in the matching network are not independent; that is, they each affect both the phase and magnitude of the monitored impedance,

2. Any particular adjustment of one of the capacitors may produce opposite polarity signals from one of the detectors; for example, if the shunt capacitance is increased while the series capacitance is held constant, the magnitude detector may produce a positive output, but if the series capacitor is set to a new value, the same increase in shunt capacitance may lead to a negative output from the magnitude detector, and

3. The impedance of the sputtering system, a glow discharge chamber, depends on the RF voltage supplied. This voltage is a function of the values of the matching network components. Therefore, matching the sputtering system to the transmission line becomes analogous to the "dog chasing its tail."

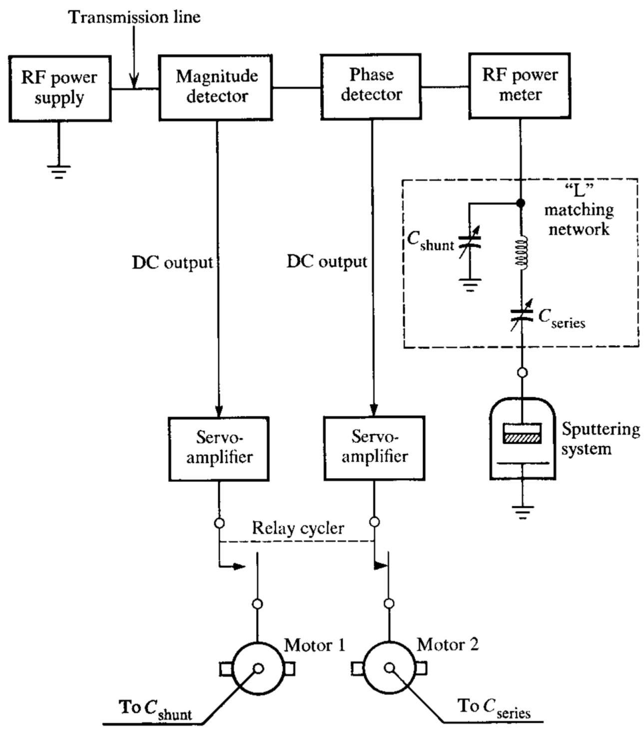

Figure 40. Block diagram of an impedance matching network

An automatic impedance matching was presented by (Vai & Prasad, 1993), a novel technique that uses a neural network to adjust a stub-tuning network. Adjusting the locations and lengths of the stubs is fully automated and thus precise. Since this work is focused on plasma processes, the following discoveries in the impedance matching control systems are more related to the results presented by Mazza.

Many works were reported using different control strategies to solve the impedance matching problem using neural networks, genetic algorithms, deterministic tuning with look-up tables and adaptive systems, and nonlinear control systems (Bacelli. et al., 2007). The matching conditions do not affect the load impedance in all these cases. (Bacelli. et al., 2007) proposed a hierarchical structure controller composed of a coarse controller at higher levels that drives the system close to the matching point and a feedback controller at lower levels for fine-tuning. Also, (Firrao et al., 2008) used two steps: the imaginary part of the load impedance is tuned to (almost) zero using a series (or shunt) reactance, and then the resulting real part is transformed to the target real value with a tunable transformer. Hirose in (Hirose et al., 2009) used a Seek + Follow control for robust behavior using the phase and amplitude of the impedance as reference variables. An adaptive impedance matching is proposed by (van Bezooijen et al., 2010) and presents an overview of adaptive controlled matching networks. (Ishida et al., 2011) presented the same idea as Hirose but with different conditions and assumed that it knows the exact value of the network components. The results showed a controllable region but did not analyze the impedance region corresponding to the series and shunt capacitor values. A tracking controller is demonstrated in (Li et al., 2019) with initial conditions close to the desired value.

The extremum control is also applied to solve this problem in (Zhang & Ordóñez, 2012; Viola et al., 2021). Furthermore, a centralized controller that uses feedback compensation to regulate power and feedforward correction for impairments in RF power transmission is presented in (Coumou, 2012, 2013). In addition, binary search is applied with significant improvement in convergence time but does not guarantee a monotonic decrease in the reflected power over time (Xiong & Hofmann, 2016; Xiong et al., 2020).

More recently, (Alibakhshikenari et al., 2020) proposed an automatic quantum genetic algorithm (AQGA) to optimize T-type networks by harnessing principles of quantum mechanics for efficient computation. In another study, (Roessler et al., 2023) used a discrete search algorithm in a field programmable array (FPGA) with a switched stub tuner capable of optimizing output power in just 260 μs. Shin in (Shin & Hong, 2023) proposed a Stochastic Gradient Descent optimization to achieve a fast matching time and high efficiency of the matching trajectories.

To address the challenge of large and heavy matching boxes, Hanaoka (Hanaoka et al., 2020) and Jurkov (Jurkov et al., 2020) proposed frequency-variable tuning to achieve impedance matching within 5 ms. Motor-driven variable vacuum capacitors (VVCs) have become a prevalent choice in the industry due to their extensive tunability.

4.3 Modeling of network configuration

The matching network can be designed using different configurations. The most used architectures are the L-type (van Bezooijen et al., 2010), Π, and the T network, Figure 41. The L-type network shown in Figure 42 can provide a unique solution using only two variables: a series capacitor C_m and a shunt capacitor C_t. So, the network can be easily tuned for any feasible load impedance (Thompson & Fidler, 2004).

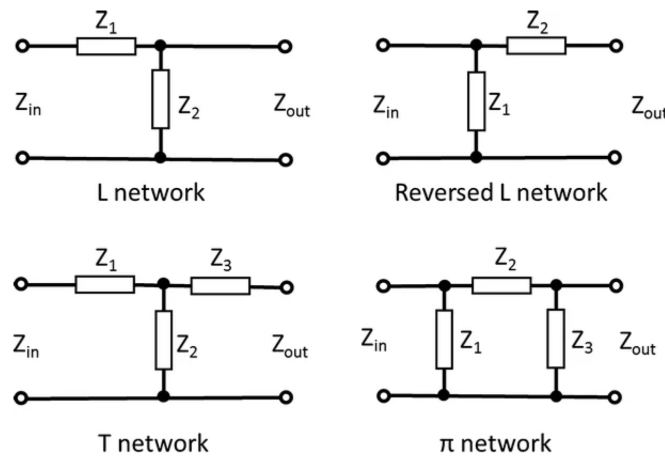

Figure 41. L, Pi, and T network configurations.

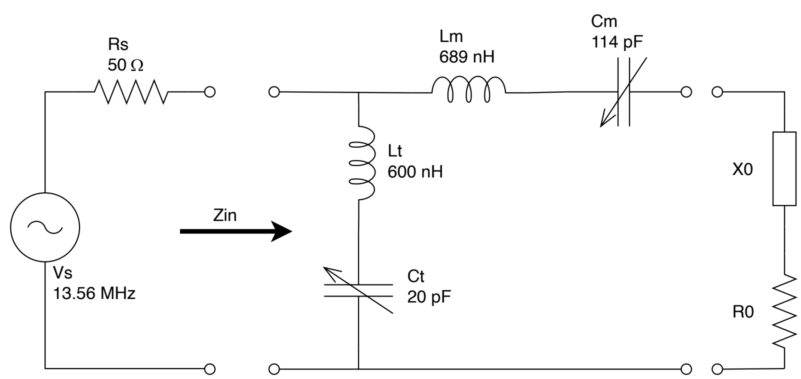

Figure 42. L-Network configuration.

The load impedance of the network is given by $Z_0 = R_0 + jX_0$. Therefore, by changing the capacitance of the variable capacitors C_t and C_m, the input impedance seen from the generator toward the load Z_{in} can be controlled. A V-I probe can be placed in different locations in the network before the chamber, only measuring the impedance of the plasma or in the power generator and seeing the impedance of the complete network. For our analysis, the sensor is assumed to be on the input side of the network, giving the impedance amplitude and phase. It is well known (Zhang & Ordóñez, 2012) that maximum power transfer in a system occurs when the network impedance Z_{in} is equal to the complex conjugate of the source impedance Z_s,

$$Z_{in} = Z_s^*, \tag{96}$$

and for the most RF power generator, Z_s is equal to 50 Ohms.

The power loss through Ohmic heating and degradation over time due to high voltages across the capacitors reduces the efficiency of the matching network. In addition, any changes in plasma parameters (e.g., RF power, pressure, gas mixture) or stray components in the network will affect the network impedance. Consequently, the reflected power affects the transfer power to the load. The reflection coefficient is determined by the load impedance Z_{in} at the end of the transmission line, as well as the characteristic impedance of the line Z_s, given by

$$|\Gamma| = \sqrt{\frac{P_r}{P_{in}}} = \left|\frac{Z_{in} - Z_s}{Z_{in} + Z_s}\right|. \tag{97}$$

More generally, the squared magnitude of the reflection coefficient $|\Gamma|^2$ denotes the proportion of that power that is "reflected" and absorbed by the source P_r, with the power delivered to the load P_d, being $(1 - |\Gamma|^2)P_{in}$.

The RF power generator presented in Figure 42 can deliver a maximum of 15 kW at a frequency of 13.56 MHz with a generator output impedance $50\ \Omega$. A stepping motor moves the series capacitor (C_m), and the shunt capacitor (C_t), and the speed of the motor limits the change rate. In this case, the rate limit for the motors is $100\ \%/s$ with a second-order dynamic and a time constant of $20\ ms$. The current profile of the motors uses the maximum rate limit, which does not guarantee a global monotonic decrease of the reflected power. The details of the matching box shown in Table 8, and the range of load impedance on the real and imaginary axes for the capacitors' values are shown in Figure 43.

Table 8. Parameters of the matching box.

	Minimum	Maximum
C_m	$114\ pF$	$445\ pF$
C_t	$20\ pF$	$205\ pF$
L_m	$689\ nH$	
L_t	$600\ nH$	

As mentioned, there are different configurations of matching boxes to match the impedance between the source and the load. The reference signal to control the matching box with the proper behavior of the system depends on the network configuration. According to (van Bezooijen et al., 2010; Xiong et al., 2020) for Γ, the downconverting networks of T and L, the right variable is the impedance. Nevertheless, for the L up-converting is the admittance. The model of the matching network, including the load impedance, is given by (102). Initially, the impedance in section $Z_1 = f(L_m, C_m, X_0, R_0)$ is

$$Z_1 = R_0 + j\left(\omega L_m - \frac{1}{\omega C_m} + X_0\right) \tag{98}$$

$$Y_1 = \frac{1}{Z_1} = \frac{R_0 - j\left(\omega L_m - \frac{1}{\omega C_m} + X_0\right)}{R_0^2 + \left(\omega L_m - \frac{1}{\omega C_m} + X_0\right)^2} \tag{99}$$

$$Y_1 = G_1 - jB_1. \tag{100}$$

Thus, the input admittance can be obtained as:

$$Y_{in} = Y_1 - j\left(\frac{\omega C_t}{\omega^2 C_t L_t - 1}\right) \tag{101}$$

$$Y_{in} = G_1 - j\left(B_1 + \frac{\omega C_t}{\omega^2 C_t L_t - 1}\right) \tag{102}$$

with

$$G_1 = \frac{R_0}{R_0^2 + \left(\omega L_m - \frac{1}{\omega C_m} + X_0\right)^2} \tag{103}$$

$$B_1 = \frac{\omega L_m - \frac{1}{\omega C_m} + X_0}{R_0^2 + \left(\omega L_m - \frac{1}{\omega C_m} + X_0\right)^2}. \tag{104}$$

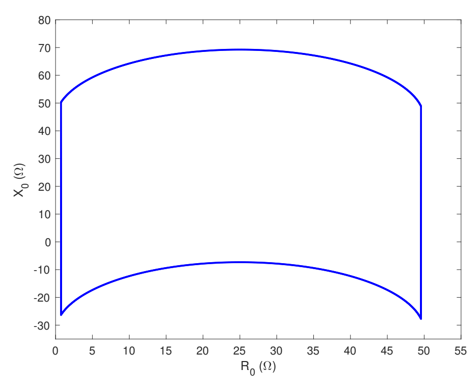

Figure 43. Range of the load impedance (real and imaginary part) for the L-type network.

Figure 44 shows the range of feasible load impedance in Smith's chart. So, the controller has to be able to drive the impedance value to the center of the Smith chart that represents $Y = 0.02\ S$ or

$Z = 50\ \Omega$.

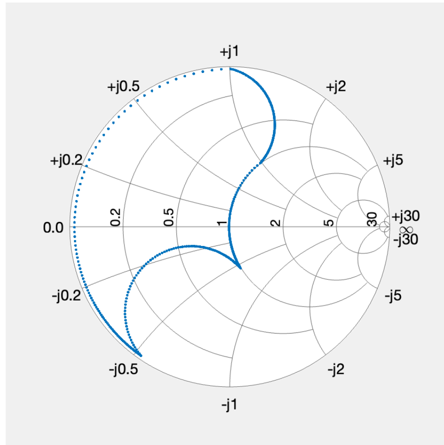

Figure 44. Smith chart range of the L-type network load impedance.

4.4 Feedforward control design

Initially, feedforward control is proposed as a baseline for the RF impedance benchmark, using the block diagram in MATLAB Simulink, Figure 46. It uses the high rate limit of the motors at the same time, called (MAX-MAX). However, in addition to this profile, achieving a low convergence time to zero of the reflected power does not guarantee a monotonic decreasing behavior. Therefore, a new profile design is proposed using three or four points, as shown in Figure 45. To build the 3-point and 4-point profiles, the knobs (r_i and r_j) were used, respectively, with $i = 1, 2, 3$ and $j = 1, \ldots, 5$. The 3-points and 4-points present a similar performance, then for simplicity was selected the 3-points.

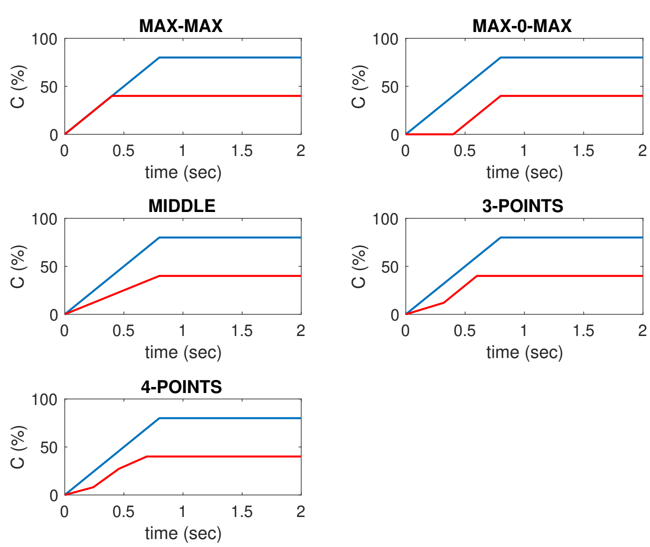

Figure 45. Trajectory of the capacitor position for the profiles used in the Feedforward controller.

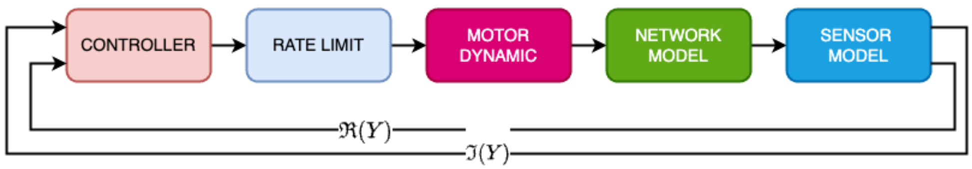

Figure 46. Block diagram for the RF impedance matching with L-type network.

To find the optimal values, it has the cost function with the convergence time T_{tune}

$$\min_{r_{1\dots n}} J = w_1 T_{tune} + w_2 \max\left\{\frac{d}{dt}|\Gamma|\right\}. \tag{105}$$

The ensemble values of the profiles are given by (106) for the 3-points and (107) for the 4-points. Figures 47 and 48 show how the three- or four-point profile guarantees a monotonic decreasing behavior in the reflection coefficient.

$$r_1 = 0.6425, r_2 = 0.3865, r_3 = 0.7556, \tag{106}$$

$$\begin{aligned} r_1 = 0.6425, r_2 = 0.3865, r_3 = 0.7556, \\ r_4 = 0.6448, r_5 = 0.3668; \end{aligned} \tag{107}$$

The performance of the feedforward controller is evaluated using a set of performance criteria defined by (108) - (111). These indices are the controller tuning time, the integral of the reflection coefficient, and the mean reflected power and the peak power, respectively. Table 9 compares the performance of the feedforward controller using the profiles (MAX-MAX, MAX-0-MAX, MIDDLE, 3 POINTS, and 4-POINTS).

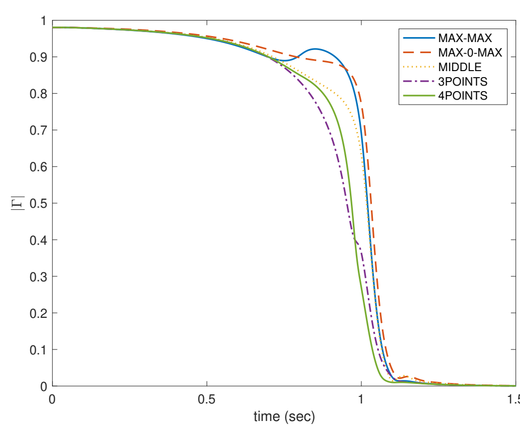

Figure 47. Performance of $|\Gamma|$ using different profiles.

The best performance was obtained for $w_1 = 0.7$ and $w_2 = 0.3$, resulting in an optimal capacitor path and transient reflection coefficient by the 3-point feedforward profile.

$$T_{tune} = \text{time to fall within 5\% of } |\Gamma|_{final}, \tag{108}$$

$$G_{int} = \int_0^t |\Gamma(t)| dt, \tag{109}$$

$$max(P_r) = \max_{i \in n} P_r(i), \tag{110}$$

$$mean(P_r) = \text{mean}(P_r). \tag{111}$$

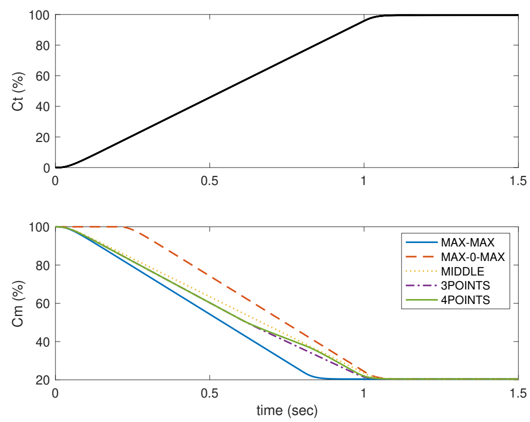

Figure 48. Profile of the C_t and C_m capacitor.

Table 9. Performance of the system for different profiles in the Feedforward Control.

PROFILES		T_{tune} (sec) mean	T_{tune} (sec) max	G_{int} mean	G_{int} max	mean(P_r) (kW) mean	mean(P_r) (kW) max	max(P_r) (kW) mean
MAX-MAX		0.613	1.132	178.962	536	5.468	14.203	8.783
MAX-0-MAX		0.627	1.16	190.205	537.476	5.973	14.040	8.773
MIDDLE		0.618	1.158	182.079	537.177	5.535	13.753	8.754
3-POINTS	Optimal	0.612	1.128	180.982	536.256	5.555	14.118	8.753
	Ensemble	0.610	1.14	179.875	536.359	5.527	14.118	8.759
4-POINTS	Optimal	0.611	1.128	181.357	536.362	5.582	14.118	8.764
	Ensemble	0.611	1.148	180.229	536.350	5.533	14.118	8.757

4.5 Feedback control design

An RF impedance benchmark compares the controllers proposed by Bacelli (Bacelli. et al., 2007), Hirose (Hirose et al., 2009), Ishida (Ishida et al., 2011), Bezooijen (van Bezooijen et al., 2010), Cottee (Cottee & Duncan, 2003) and our proposal PI+FF.

All strategies are available at (Rodriguez et al., 2021) by *Bacilli.xls, Hirose.slx, Ishida.slx, Bezoo.xls, Cottee.xls* and *PI.xls*. Bacelli used Γ as a controllable variable with the control rule with τ as a certain time delay. Only analyze one system condition and show robustness against variations (a step in RF power, gate valve position, in O_2 and A_r flow).

$$\begin{aligned} u_{C_t} &= Im\left(\Gamma\right) \\ u_{C_m} &= -\left(1-|\Gamma|\right)^2 Re\left(\Gamma\right) + 0.1|\Gamma|\text{sgn}\left(\Gamma(t)-\Gamma(t-\tau)\right) \end{aligned} \tag{112}$$

Hirose and Ishida (Hirose et al., 2009) used a Seek+Follow strategy with different switching conditions. Hirose proposes a switch between the controllers under the conditions

$$\begin{aligned} Follow &= \{35 \leq |Z_{in}| \leq 65\ ,\ -30 \leq \phi \leq 30\} \\ Seek &= \{|Z_{in}| < 35\ or\ 65 < |Z_{in}|\ ,\ \phi < -30\ or\ 30 < \phi\} \end{aligned} \tag{113}$$

while Ishida,

$$\begin{aligned} Follow &= \{40 \leq |Z_{in}| \leq 60\ ,\ -18 \leq \phi \leq 18\} \\ Seek &= \{|Z_{in}| < 40\ or\ 60 < |Z_{in}|\ ,\ \phi < -18\ or\ 18 < \phi\}. \end{aligned} \tag{114}$$

The Follow controller consists on

$$\begin{aligned} \phi > 0, &\quad \text{decrease } C_m \\ \phi < 0, &\quad \text{increase } C_m \\ |Z| > 50, &\quad \text{decrease } C_t \\ |Z| < 50, &\quad \text{increase } C_t \end{aligned} \tag{115}$$

and the Seek controller on the system's inverse model to compute the capacitors' desirable value to match the impedance value.

On the other hand, Bezooijen (van Bezooijen et al., 2010) analyzed the behavior of the real and imaginary part of the impedance against the displacement of the capacitors C_t and C_m. Then, they proposed a control rule for each impedance matching network type, resulting for L-network the one given by (116),

$$\begin{aligned} u_{C_t} &= K_t\left(B_{ref} - B_{in}\right), \\ u_{C_m} &= -K_m(G_{ref}\text{sgn}\left(-B_{in}\right) - G_{in}). \end{aligned} \tag{116}$$

The problem with the previous strategies is that they only analyzed the behavior of the network under a closed region of the matching value and not globally. Then, Cottee (Cottee & Duncan, 2003) performed a global analysis of the network and proved the local and global stability of the network. Following his methodology for the L-Type network, the control action is defined by (117)

$$
\begin{aligned}
u_{C_t} &= -A\text{sgn}\left(s_1\right) \\
u_{C_m} &= -B\text{sgn}\left(s_2\right)
\end{aligned}
\tag{117}
$$

with

$$
s_1 = B_{in} \tag{118}
$$

$$
s_2 = \begin{cases} -B_{in} - \frac{1}{\beta_{min}+\omega L_t}, & -B_{in} - \frac{1}{\beta_{min}+\omega L_t} \leq 0 \\ 0.02 - G_{in}, & -B_{in} - \frac{1}{\beta_{min}+\omega L_t} > 0; \end{cases} \tag{119}
$$

and $\beta_{min} = -\frac{1}{\omega C_{mmin}}$.

4.5.1 Proportional-Integral controller

Based on the information of the reflected coefficient ($|\Gamma| \leq threshold$), the system switches between the Feedforward and Feedback Control and using different values ($threshold = 0.1, 0.3, 0.5, 0.7, 0.9, 1$), the performance of the system changes. The system is under the Feedback Control only when the threshold equals one. The proposed control action is defined as

$$
\begin{aligned}
Follow &= \{|\Gamma| \leq \text{threshold}\}, \\
Seek &= \{|\Gamma| > \text{threshold}\},
\end{aligned}
\tag{120}
$$

and the Follow Controller is

$$
\begin{aligned}
u_{C_t} &= K_t\left(B_{ref} - B_{in}\right), \\
u_{C_m} &= -K_m\left(G_{ref} - G_{in}\right),
\end{aligned}
\tag{121}
$$

with $K_t, K_m > 0$. The performance of the controllers presented in the previous section is evaluated under a set of extremum load impedance values and initial conditions of the capacitors C_t and C_m that were selected as shown in Figure 49(b). As an example, Figure 50 shows the response of each controller for $Z_{load} = 12.9 - j8.6\ \Omega$ with initial conditions $C_{t0} = 0\ \%$ and $C_{m0} = 50\ \%$. The best performance is observed for controllers that use admittance as a controllable variable (Bezooijen, Cottee, and PI+FF). Nevertheless, the Cotee controller presents a high value of the integral of $|\Gamma|$, which is related to the slow convergence of the system. Ishida improved Hirose's performance by reducing the region of Follow Control using the Seek Control to get closer to the matching point. Still, both use the impedance's phase and amplitude, which is inappropriate for this type of network. However, using the same idea but with the proper signal (admittance) and the reflection coefficient $|\Gamma|$ as a measurement of the distance to the matching value, the convergence time is reduced, and the percentage of convergence is superior to the other strategies for $|\Gamma| \leq 0.9$.

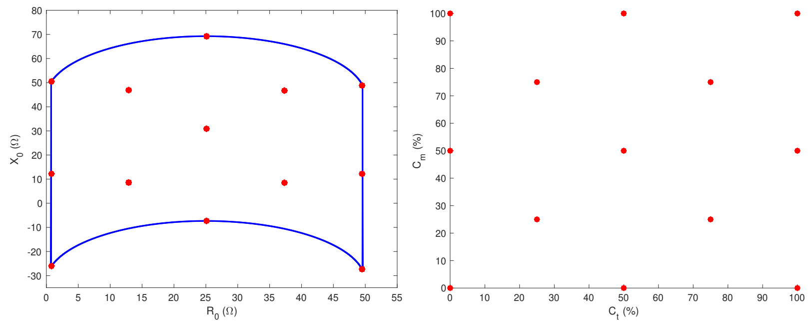

(a) Load impedance values (b) Capacitor values

Figure 49. Extremum values of load impedances and capacitors.

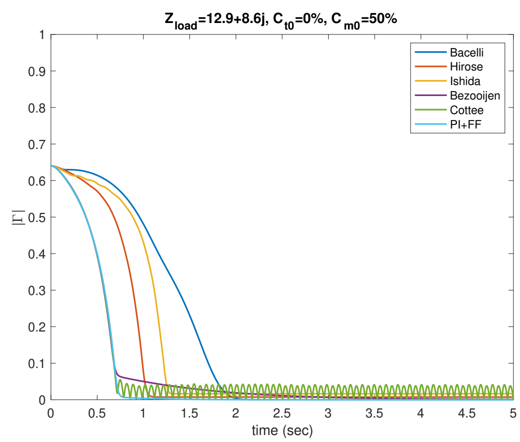

Figure 50. Response of the controllers for $Z_{LOAD} = 12.9 + j8.6\Omega$.

Figure 51 shows the response of the controllers against a step perturbation in the load impedance equal to $Z_{pert} = 5 - j5\Omega$. The Bacelli controller presents the best rejection again perturbation and validates its conclusion (Bacelli. et al., 2007). The Bezooijen, Hirose, and Ishida are not robust against perturbation in the load impedance.

In case of distortion in the amplitude (122),

$$|Z_{in}| = |Z_{in}| + k|Z_{in}|^3, \; k = 5e-4. \tag{122}$$

all model base controllers (MBC) do not match the impedance of the system, as shown in Figure 52. The distortion in phase does not affect the system's response. For the PI+FF controller with $|\Gamma| = 0.1$ the Figure 53 and 54 show the phase plane of the capacitors for the load impedance $Z_{load} = 12.9 + j8.6\ \Omega$

and $Z_{load} = 37.32 + j46.7\ \Omega$ respectively, using all the range of values of the capacitors. The feedforward control drives the capacitors simultaneously but not at the same rate (almost straight line in the phase plane) to ensure a monotonic decrease of the reflection coefficient and reduce the system's convergence time.

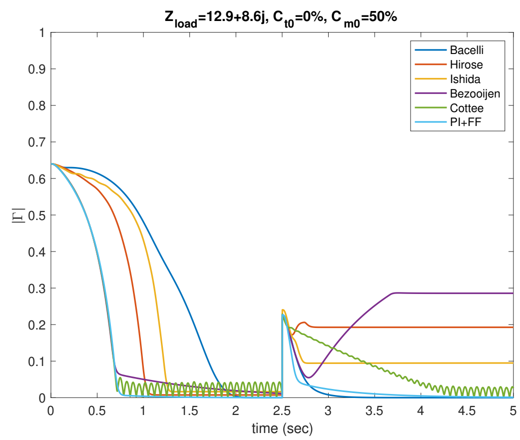

Figure 51. Response against perturbation $Z_{PERT} = 5 - j5\Omega$.

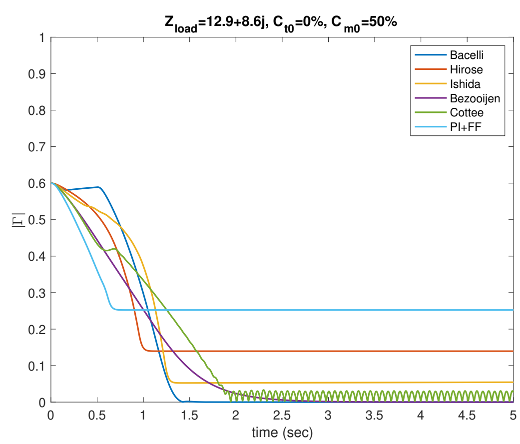

Figure 52. Response of the system with distortion in the amplitude.

Table 10. Performance of the controllers with optimal parameters.

CONTROLLERS		T_{tune} (sec) mean	max	G_{int} mean	max	mean(P_r) (kW) mean	max	max(P_r) (kW) mean	% Conv.
Bacelli (Bacelli. et al., 2007)		2.894	19.996	736.737	7.386	3.016	12.756	5.638	61.54
Hirose (Hirose et al., 2009)		7.517	14.998	1063	4660	3.014	14.454	8.913	71.01
Ishida (Ishida et al., 2011)		7.114	14.998	1107	7175	3.165	14.101	8.782	85.21
Bezooijen (van Bezooijen et al., 2010)		1.9	4.996	507.322	2407	4.725	14.301	8.821	84.62
Cottee (Cottee & Duncan, 2003)		5.310	47.372	2188.245	22290.339	5.281	13.878	8.755	100
	0.1	0.642	1.382	180.826	536.415	5.461	14.093	8.759	100
	0.3	0.707	1.926	185.696	537.812	5.230	13.810	8.809	99.41
PI+FF	0.5	0.727	3.148	191.090	541.208	5.287	14.032	8.959	96.45
	0.7	0.755	3.708	196.618	657.099	5.271	14.211	9.012	94.08
	0.9	0.729	2.13	197.082	535.273	5.327	14.102	8.924	91.12
	1.0	0.738	1.982	198.532	936.626	4.779	13.634	8.299	82.24

Finally, Table 10 shows the performance indices of the controllers evaluated for all the initial conditions described in Figure 49. For the 13 extremum values of capacitance and load impedance, a total of

169 cases were obtained. For each case, optimal values of the controllers were obtained and are available at (Rodriguez et al., 2021). As can be seen, for the proposed controller PI + FF with $|\Gamma| = 0.1$, a global convergence (100 %) of precision is reached but decreases as $|\Gamma|$ increases.

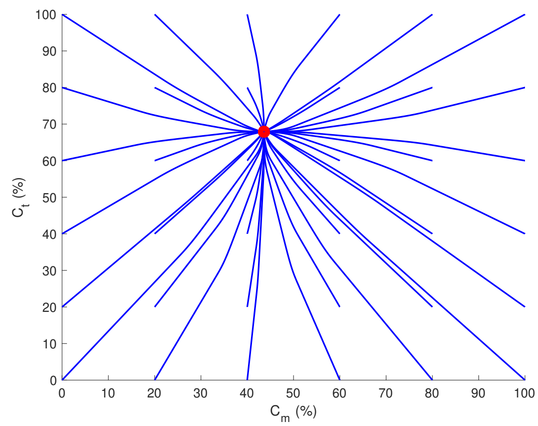

Figure 53. Phase plane for $Z_{LOAD} = 12.9 + j8.6\ \Omega$.

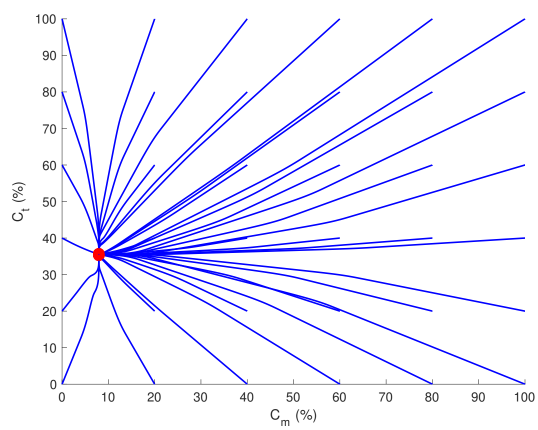

Figure 54. Phase plane for $Z_{LOAD} = 37.32 + j46.7\ \Omega$.

4.5.2 Control Lyapunov function with safety constraints

A state representation of this network has been proposed by (Cottee & Duncan, 2003), using $x = [\alpha, \beta]^T = [-1/(\omega C_m), -1/(\omega C_t)]^T$ as state and $y = [R_{in}, X_{in}]^T$ as output. We propose a more convenient state definition given by

$$
\begin{aligned}
x &= \begin{bmatrix} C_m \\ C_t \end{bmatrix} \\
y &= \begin{bmatrix} G_{in} \\ B_{in} \end{bmatrix} = \begin{bmatrix} \frac{R_0}{\theta^2 + R_0^2} \\ -\frac{\omega x_2}{\omega^2 x_2 L_t - 1} - \frac{\theta}{\theta^2 + R_0^2} \end{bmatrix},
\end{aligned}
\tag{123}
$$

with

$$\theta = \omega L_m - \frac{1}{\omega x_1} + X_0. \tag{124}$$

For a desired reference signal $y_d = (0.02, 0)^T$ [S], it has a tracking error signal $e(t) = y(t) - y_d$. Now, the objective of the control law is that the closed-loop system be stable and the output can track the reference input asymptotically in the following sense:

$$\lim_{t\to\infty} (y(t) - y_d) = 0. \tag{125}$$

As a result, the system with the tracking error $e(t)$ as the output takes the following form:

$$\begin{aligned} \dot{x} &= \begin{bmatrix} u_1 \\ u_2 \end{bmatrix} \\ e &= \begin{bmatrix} \frac{R_0}{\theta^2+R_0^2} - 0.02 \\ -\frac{\omega x_2}{\omega^2 x_2 L_t - 1} - \frac{\theta}{\theta^2+R_0^2} \end{bmatrix}, \end{aligned} \tag{126}$$

and the error dynamic can be found by differentiating $e(t)$,

$$\dot{e} = \begin{bmatrix} \frac{2(e_1+0.02)(\beta+e_2)}{\omega {x_1}^2} & 0 \\ \frac{(\beta+e_2)^2-(e_1+0.02)^2}{\omega {x_1}^2} & \frac{\omega}{(\omega^2 x_2 L_t-1)^2} \end{bmatrix} \begin{bmatrix} u_1 \\ u_2 \end{bmatrix}. \tag{127}$$

Figure 55 shows a phase space trajectory diagram to understand the system behavior better. If a, b, c, and d are complex constants with $ad - bc = 0$, then the complex function defined by (128) is referred to as a linear fractional transformation (LFT).

$$w = \frac{az+b}{cz+d}, \quad z \in C \tag{128}$$

A linear fractional transformation maps a circle or a line in the z-plane to either a line or a circle in the w-plane. The central point and radius of the circle in the w-plane are determined by complex constants a, b, c, and d. After applying this mathematical transformation, it has

$$\left(e_1 - \frac{1+0.04R_0}{2R_0}\right)^2 + (e_2+\beta)^2 = \left(\frac{1}{2R_0}\right)^2, \tag{129}$$

with the help of linear fractional transformation.

The changes in the series capacitor C_m move the error over the circumference arc, while the variation in the shunt capacitor C_t shifts the center in its y-axis. According to the capacitor values, the phase space presents geometric restrictions to converge the error to zero, i.e., the series capacitor in the upper section of the circumference has always increased.

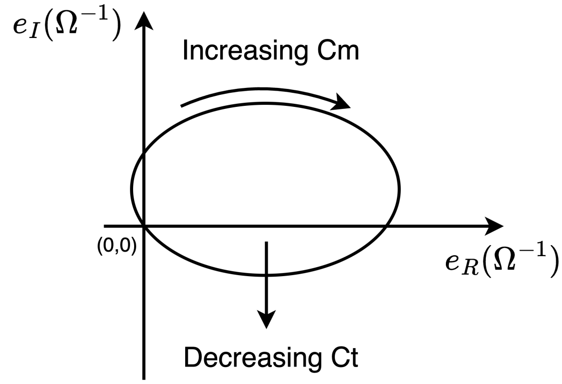

Figure 55. Plot of phase space showing possible trajectories of e_1 and e_2 as the capacitors changed.

4.5.2.1 Control Lyapunov function

Notation 4.1 *By $\overline{M}$, we denote the closure of the set M.*

Definition 4.1 ((Lafferriere & Sontag, 1993)) *Let M be an open connected subset of $\mathbb{R}^n$. Given the system,*

$$\dot{x} = f(x) + \sum_{i=1}^{m} g_i(x)u_i, \tag{130}$$

a function $V : \overline{M} \to \mathbb{R}$ is called a CLF for (130) *in M if the following is satisfied:*

1. *V is continuous on $\overline{M}$, and of class $\mathcal{C}^1$ on M*
2. *V is positive definite and proper on $\overline{M}$*
3. $\inf_{u\in\mathbb{R}^m}\{L_fV(x) + u_1L_{g_1}V(x) + \cdots + u_mL_{g_m}V(x)\} < 0$ *for each $x \in M$.*

The existence of a CLF for the system (127) is equivalent to the existence of a global asymptotically stabilizing control law.

$$u = k(e), \tag{131}$$

which is smooth everywhere, except possibly at $e = 0$ (Artstein, 1983). Moreover, such a control law can be explicitly calculated k from f, g, and V (Sontag, 1989).

Based on the geometric restriction shown in Figure 55, if $e_2 + \beta > 0$, it is known that the series capacitor C_m has to move counterclockwise until it reaches the lower section $e_2 + \beta \leq 0$ to reach the origin of the system.

The reflection coefficient magnitude can be expressed as a function of the input admittance value $|\Gamma| = \mathcal{F}(e)$. For passive loads, the magnitude is $0 \leq |\Gamma| \leq 1$. According to the practical conditions of the impedance matching network, the magnitude of the reflection coefficient is always positive and zero for the matching condition.

The reflection coefficient magnitude in the state of the system (127) can be expressed as

$$|\Gamma| = \frac{\sqrt{e_1^2 + e_2^2}}{\sqrt{(e_1 - 0.04)^2 + e_2^2}}. \tag{132}$$

The purpose is to decrease the reflection coefficient magnitude at minimum time and ensure a monotonic decreasing behavior of (132), i.e.,

$$\frac{d}{dt}|\Gamma| \leq 0. \tag{133}$$

Based on the desired behavior of $|\Gamma|$, we propose a Lyapunov function

$$V(e) = |\Gamma| = \frac{\sqrt{e_1^2 + e_2^2}}{\sqrt{(e_1 - 0.04)^2 + e_2^2}}, \tag{134}$$

where $V(e)$ is positive definite and $V(e) = 0$ only at the origin of the system. In the next section, $V(e)$ is proven to be a CLF.

4.5.2.2 A piecewise continuous controller

The nonlinear output dynamic (127) cannot be controlled by a continuous feedback law; therefore, a piecewise continuous controller is designed to make the system globally asymptotically stable.

From the universal construction of Artstein's theorem on nonlinear system (130) stabilization, the construction of the controller k can be carried out directly without explicit resources to the general result Sontag (1989),

$$k := -\frac{a(x) + \sqrt{a(x)^2 + b(x)^4}}{b(x)}, \tag{135}$$

where

$$a(x) := \nabla V(x) f(x), \tag{136}$$

$$b(x) := \nabla V(x) g(x). \tag{137}$$

The condition that V is a CLF is precisely the statement that

$$b(x) = 0 \implies a(x) < 0 \tag{138}$$

for all nonzero x.

For the system output (126) we can establish the feedback law $k_{i,j}$ with $i = 1, 2$ corresponding to sections C_i and $j = 1, 2, \ldots, m$. The series capacitor for section M_1, according to the phase-plane restriction, is

$$k_{1,1} = \frac{625\left(e_1^2 + e_2^2\right)}{(50e_1 + 1)} > 0, \tag{139}$$

and the control law of the shunt capacitor is

$$k_{1,2} = \begin{cases} \frac{\beta V(e)}{b_2} - \frac{b_1}{b_2} k_{1,1} & b_2 \neq 0, \\ 0 & b_2 = 0, \end{cases} \tag{140}$$

to obtain

$$\dot{V} = L_f V + \sum_{i=1}^{2} L_{g_i} V k_{1,i}, \tag{141}$$

$$= b_1 k_{1,1} + b_2 k_{1,2}, \tag{142}$$

$$= b_1 k_{1,1} + b_2 \left(\frac{\beta V(e)}{b_2} - \frac{b_1}{b_2} k_{1,1} \right), \tag{143}$$

$$= \beta V(e) \leq 0. \tag{144}$$

Then, we must ensure that the capacitors drove according to the condition (133). In subsection M_2, the system is not conditioned to any restriction, so the Sontag's general formula (135) can be applied to obtain the controller that makes the system globally asymptotically stable, that is,

$$k_{2,1} = -b_{2,1}, \tag{145}$$

$$= -\frac{\varphi\big(\beta^2 e_2 + \beta {e_1}^2 + 0.04\beta e_1 + \beta {e_2}^2 - 0.0004 e_2\big)}{625}, \tag{146}$$

and,

$$k_{2,2} = -b_{2,2}, \tag{147}$$

$$= -\frac{\varphi e_2}{625}, \tag{148}$$

with

$$\varphi = \frac{(50e_1 + 1)}{\sqrt{e_1^2 + e_2^2}\sqrt{\Big((e_1 + 0.04)^2 + e_2^2\Big)^3}}. \tag{149}$$

We conclude that the feedback law

$$k(e) = \begin{cases} k_{1,j}(e) & e_2 + \beta > 0 \\ k_{2,j}(e) & e_2 + \beta \le 0 \\ 0 & e_1 = e_2 = 0. \end{cases} \tag{150}$$

with $j = 1, 2$ always drives the error signal towards the origin with a consistently decreasing behavior of the reflection coefficient. This means that the system output consistently follows and tracks the reference signal, ensuring a seamless convergence of the error to zero.

4.5.2.3 Control barrier function (CBF)

Unlike stability, which involves driving a system to a given point (or set), safety can be framed in the context of enforcing the invariance of a set, i.e., the system must not leave a safe set. In particular, we consider a set $\mathcal{C}$ defined as the super-level set of a continuously differentiable function $h : H \subset \mathbb{R}^n \to \mathbb{R}$, yielding:

$$\mathcal{C} = \{x \in H \subset \mathbb{R}^n : h(x) \ge 0\}, \tag{151}$$

$$\partial\mathcal{C} = \{x \in H \subset \mathbb{R}^n : h(x) = 0\}, \tag{152}$$

$$\mathrm{Int}(\mathcal{C}) = \{x \in H \subset \mathbb{R}^n : h(x) > 0\}. \tag{153}$$

We refer to $\mathcal{C}$ as the safe set (Ames et al., 2019).

Definition 4.2 *The set $\mathcal{C}$ is forward invariant if for every $x_0 \in \mathcal{C}$, $x(t) \in \mathcal{C}$ for $x(0) = x_0$ and for all $t \in I(x_0)$. The system* (126) *is safe concerning the set $\mathcal{C}$ if the set $\mathcal{C}$ is forward invariant.*

With the motivation of CLF, the concept of safety can be generalized under the definition of CBF.

Definition 4.3 ((Ames et al., 2019)) *Let $\mathcal{C} \subset H \subset \mathbb{R}^n$ be a superlevel set of a continuously differentiable function $h : H \to \mathbb{R}$, then h is a CBF if there exists an extended class K_∞ function α such that for the control system* (126)*:*

$$\sup_{u \in U} \left[L_f h(x) + L_g h(x) u\right] \geq -\alpha(h(x)), \tag{154}$$

for all $x \in H$.

Variable capacitors are limited to a minimum and maximum value. This physical restriction can be set as a safety constraint of the system and can ensure that the value of the capacitor does not exceed that limit. For both capacitors, we set two safety constraints, one for the minimum value and the other for the maximum value,

$$h_{i_1}(\bar{x}_i) = \left(\bar{x}_i + x_i^* - x_{i_{min}}\right), \tag{155}$$

$$h_{i_2}(\bar{x}_i) = \left(x_{i_{max}} - \bar{x}_i - x_i^*\right), \tag{156}$$

with $i = 1, 2$.

Applying (154) with $\alpha(h(x)) = \lambda h(x)$ and $\lambda > 0$, it has the following constraints for the control laws of the system (126), including the rate limit (RL) of the capacitors, with $i = 1, 2$, and $j = 1, 2$,

$$u_i = \begin{cases} \max\left(-\lambda\left(\bar{x}_i + x_i^* - x_{i_{min}}\right), k_{i,j}, -RL\right) & , k_{i,j} < 0, \\ \min\left(\lambda\left(x_{i_{max}} - \bar{x}_i - x_i^*\right), k_{i,j}, RL\right) & , k_{i,j} \geq 0, \end{cases} \tag{157}$$

to stop the capacitors within the safety constraints. We decided to stop the capacitor at the boundaries because we ensure their correct driving by using the control law (150). The control signal is restricted, as shown in Figure 56 below.

The system performance was evaluated with 121 feasible load impedance values in the zone shown in Figure 57(a), and 121 initial conditions of the capacitors, see Figure 57(b).

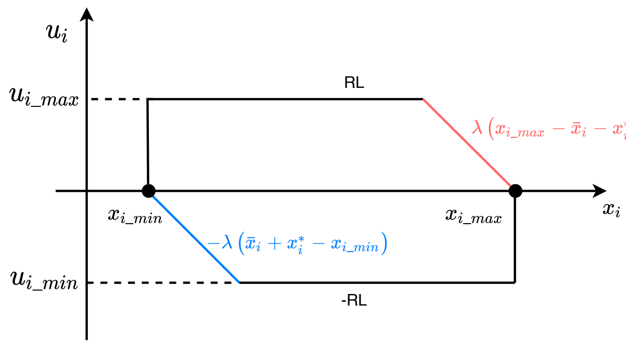

Figure 56. Safety constraint of the control signal to drive the capacitor $(i = 1, 2)$.

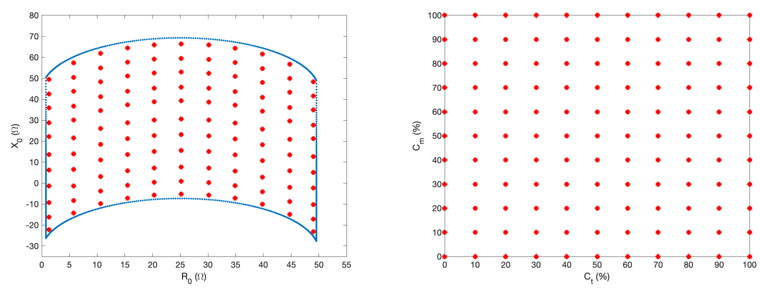

(a) (b)

Figure 57. Load impedance and capacitors values.

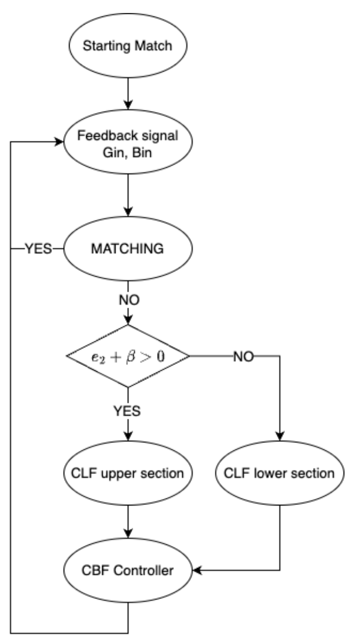

Figure 58. Flow chart of CLF+CBF control.

The CLF/CBF controller was implemented in a modified version of the benchmark proposed by (Rodriguez et al., 2021). A flow diagram of the CLF+CBF controller is shown in Figure 58. Table 11 summarizes the obtained results using the performance indices, T_{tune} time when $|\Gamma|$ remain under 0.1, G_{int} the integral of the admittance value, given by

$$T_{tune} = \max_{|\Gamma| \geq 0.1} t, \tag{158}$$

$$G_{int} = \int_0^t |\Gamma(t)| dt, \tag{159}$$

and mean(P_r) and max(P_r) for the total of 14641 cases.

Table 11. Controller performance

	T_{tune} (sec)		G_{int}		mean(P_r) (kW)		max(P_r) (kW)
CONTROLLER	mean	max	mean	max	mean	max	mean
CLF/CBF	1.11	9.33	378.62	5290	3.24	13.84	7.55
CLF	1.12	10	378.25	5298	3.33	14.03	7.56

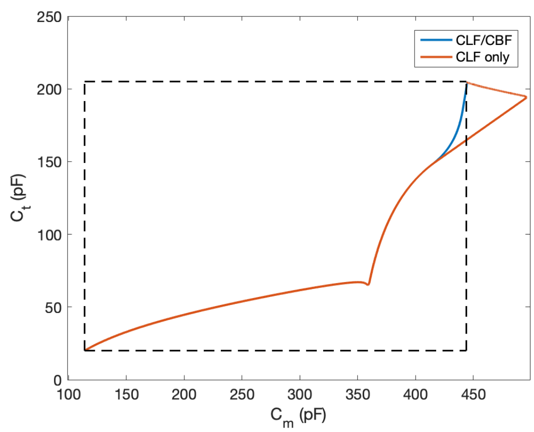

Figure 59. Feasibility conditions of capacitor C_m and C_t with CLF and CLF/CBF controller.

The results highlight the best performance of the system with the CLF/CBF controller with lower values in convergence time, average, and maximum power transfer. In addition, it should be noted that this controller restricts the value of the capacitors to the allowed region. The final gains of the controller are

$$k^*_{1,1} = k^*_{1,2} = 10^{-8} k_{1,1}; \tag{160}$$

$$k^*_{2,1} = |\Gamma|^2 \times 10^{-7} k_{1,2}; \tag{161}$$

$$k^*_{2,2} = 2|\Gamma|^2 \times 10^{-8} k_{2,2}; \tag{162}$$

$$\lambda = 10 \tag{163}$$

with the term $|\Gamma|^2$ used to reduce the effort in the capacitors when the system is close to the matching point. Figure 59 shows how the trajectories satisfy the state constraint requirements $C_{m\_min} \leq x_1 \leq C_{m\_max}$ and $C_{t\_min} \leq x_2 \leq C_{t\_max}$ with the CLF/CBF controller for a load impedance $Z_0 = 0.8 - j26\ \Omega$, and Figure 60 shows the evolution of the states over time.

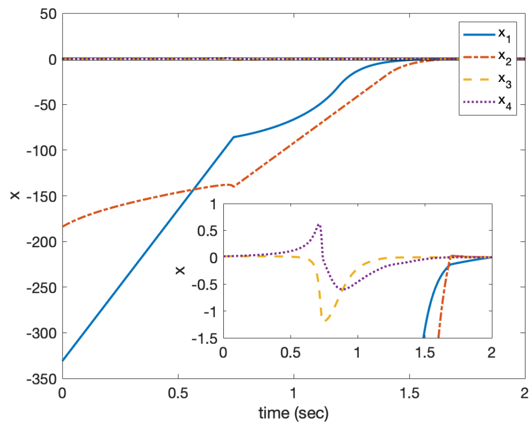

Figure 60. State trajectories of the RF impedance matching system with CLF/CBF controller.

This means that, without the CBF, the feasible capacitance region is violated when the capacitors take a minimum or maximum value to match the system impedance. Figure 61(a) shows simulated results for the phase plane of capacitors with $Z_L = 15.4200 + j62.1\ \Omega$ without CBF, and the feasible region is violated. However, in Figure 61(b), with the barrier function, the values of both capacitors are guaranteed inside that region.

4.6 Conclusions

In conclusion, establishing a benchmark system for designing and evaluating RF impedance matching controllers has provided valuable insights into the performance of various RF impedance matching controllers. A thorough comparison of proposed controllers revealed the novel Feedforward profile's effectiveness in enhancing the reflection coefficient's convergence with a desirable monotonic decreasing behavior. Although the PI + FF controller demonstrated an improved response with a switching value of $|\Gamma| = 0.1$, it fell short of achieving the global convergence achieved by the Cottee proposal without Feedforward Control. The advantage of the Feedforward approach lies in its ability to accelerate convergence; however, it does exhibit sensitivity to sensor distortion, necessitating careful consideration.

The Feedforward controller is a valuable tool to reduce the convergence time, particularly when $|\Gamma| \geq 0.3$. At the same time, the Bacelli, Bezooijen, or Cottee proposals remain preferable when near the matching value. This benchmark is a foundational platform for analyzing RF impedance matching networks within this framework. Moving forward, the exploration of additional control strategies such as Model Predictive Control (MPC), Model-Free Adaptive Control (MFAC), and Fractional Extremum Seeking Control (FESC) holds promise for further improving system performance and assessing its resilience against external disturbances and uncertainties.

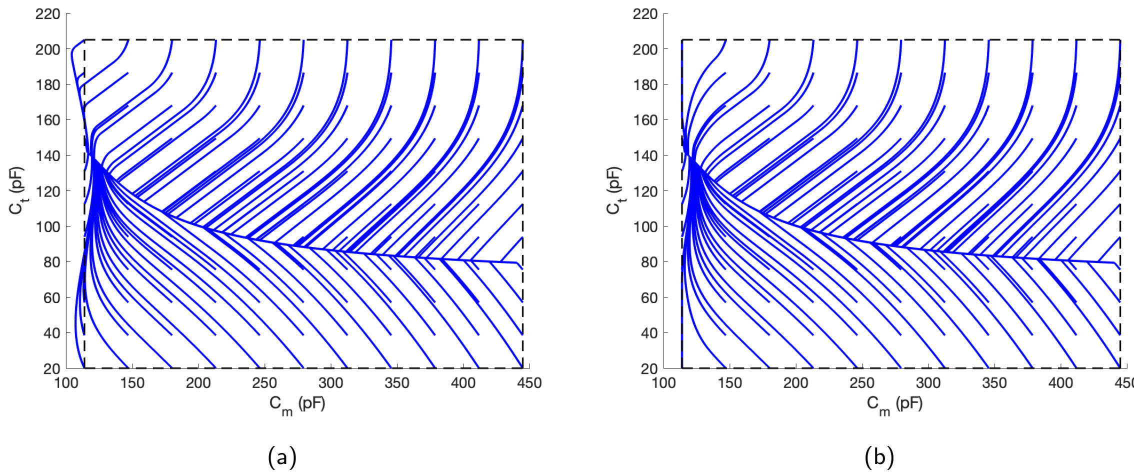

Figure 61. Phase plane of the capacitors for $Z_0 = 15.42 + j62.1\ \Omega$.

Furthermore, the design of a CLF/CBF controller introduced a significant advancement in ensuring global asymptotic stability for RF Impedance Matching systems. Addressing the intricate controller design challenges posed by phase-space geometrical constraints inherent in the L-type matching network model, the CLF/CBF controller methodology demonstrated superior convergence time to the origin compared to the existing literature. This novel approach also successfully maintains the capacitors within the feasible region, a feat that is unattainable with the CLF controller alone. In particular, this study breaks new ground by subjecting these systems to an in-depth analysis, setting the stage for future research efforts to refine control strategies and assess performance under varying conditions.

Chapter 5. Conclusions and future research

Bidirectional coupling in fractional-order dynamic synchronization has been addressed by a pilot study, which makes it innovative. Such an approach aims to explore many more parameter combinations than ever before were studied. These findings will be an important beginning point for delving into this complex subject matter and set the ground for future study using similar methods (expanding this kind of study to incommensurate fractional order systems, for instance).

Thermal systems with noninteger-order properties are characterized by complex dynamics that can be captured effectively by fractional-order transfer functions. With such an advanced modeling capability, phenomena commonly encountered in practical situations like conduction, convection, and radiation can be more accurately represented. Fractional order modeling uncovers underlying relationships, improves system designs, and enhances thermal efficiencies. It offers a complete representation of thermal system modeling combined with data-driven techniques. This method aids in bridging the gap between theoretical knowledge and real world complexities, thus enhancing our ability to design, operate and optimize thermal systems with greater accuracy and efficiency, leading to improved Digital Twins precision as well.

Finally, the CLF+CBF controller shows a significant improvement in tuning time and effective load region matching compared to other techniques evaluated. The method presented can be used to include a frequency control approach, thus shortening the time for tuning and minimizing capacitors' displacement, leading to a longer life of these components. Novel algorithms should emphasize an optimal trajectory that secures an unambiguously monotonic decrease of the reflected power while decreasing the matching time even when capacitor motion is always in line with the desired setting.

References

Adloo, H. & Roopaei, M. (2011). Review article on adaptive synchronization of chaotic systems with unknown parameters. *Nonlinear Dynamics*, *65*, 141–159. https://doi.org/10.1007/s11071-010-9880-6.

Alibakhshikenari, M., Virdee, B. S., Shukla, P., See, C. H., Abd-Alhameed, R. A., Falcone, F., & Limiti, E. (2020). Improved adaptive impedance matching for RF front-end systems of wireless transceivers. *Scientific Reports*, *10*, 14065. https://doi.org/10.1038/s41598-020-71056-0.

Alomari, A. (2011). A new analytic solution for fractional chaotic dynamical systems using the differential transform method. *Computers & Mathematics with Applications*, *61*(9), 2528–2534. https://doi.org/https://doi.org/10.1016/j.camwa.2011.02.043.

Alvino, A., Matos, M., Carpio, C. d., & Vinces, L. (2018). Development of automatic control for temperature-based reduction of bitterness in tarwi. In *2018 IEEE International Conference on Automation/XXIII Congress of the Chilean Association of Automatic Control (ICA-ACCA)*, 1–5. https://doi.org/10.1109/ICA-ACCA.2018.8609852.

Ames, A. D., Coogan, S., Egerstedt, M., Notomista, G., Sreenath, K., & Tabuada, P. (2019). Control barrier functions: Theory and applications. In *2019 18th European Control Conference (ECC)*, 3420–3431. https://doi.org/10.23919/ECC.2019.8796030.

Artstein, Z. (1983). Stabilization with relaxed controls. *Nonlinear Analysis: Theory, Methods & Applications*, *7*(11), 1163–1173. https://doi.org/https://doi.org/10.1016/0362-546X(83)90049-4.

Azar, A. T., Vaidyanathan, S., & Ouannas, A. (2017). *Fractional Order Control and Synchronization of Chaotic Systems*. Springer, https://doi.org/10.1007/978-3-319-50249-6.

Bacelli., G., V. Ringwood., J., & Iordanov., P. (2007). Impedance matching controller for an inductively coupled plasma chamber - l-type matching network automatic controller. In *Proceedings of the Fourth International Conference on Informatics in Control, Automation and Robotics - Volume 2: ICINCO*, 202–207. INSTICC, SciTePress. https://doi.org/10.5220/0001648802020207.

Badri, V. & Tavazoei, M. S. (2015). Fractional order control of thermal systems: achievability of frequency-domain requirements. *Nonlinear Dynamics*, *80*(4), 1773–1783. https://doi.org/10.1007/s11071-014-1394-1.

Barricelli, B. R., Casiraghi, E., & Fogli, D. (2019). A survey on digital twin: Definitions, characteristics, applications, and design implications. *IEEE Access*, *7*, 167653–167671. https://doi.org/10.1109/ACCESS.2019.2953499.

Bhalekar, S. & Patil, M. (2018). Singular points in the solution trajectories of fractional order dynamical systems. *Chaos: An Interdisciplinary Journal of Nonlinear Science*, *28*(11), 113123. https://doi.org/10.1063/1.5054630.

Blasch, E. P., Darema, F., & Bernstein, D. (2022). *Introduction to the Dynamic Data Driven Applications Systems (DDDAS) Paradigm*, (pp. 1–32). Springer International Publishing, Cham, https://doi.org/10.1007/978-3-030-74568-4_1.

Blekhman, I. I., Fradkov, A. L., Nijmeijer, H., & Pogromsky, A. Y. (1997). On self-synchronization and controlled synchronization. *Systems and Control Letters*, *31*(5), 299–305. https://doi.org/10.1016/S0167-6911(97)00047-9.

Boehm, R. F. (1997). *Introduction and trends in the thermal design field*, 1–15. Cambridge University Press.

Brown, R., Rulkov, N. F., & Tufillaro, N. B. (1994). Synchronization of chaotic systems: The effects of additive noise and drift in the dynamics of the driving. *Physical Review E*, *50*(6), 4488–4508. https://doi.org/10.1103/PhysRevE.50.4488.

Brunton, S. L. & Kutz, J. N. (2019). *Data-Driven Science and Engineering: Machine Learning, Dynamical Systems, and Control*. Cambridge University Press, Cambridge, https://doi.org/10.1017/9781108380690.

Brunton, S. L., Proctor, J. L., & Kutz, J. N. (2016). Discovering governing equations from data by sparse identification of nonlinear dynamical systems. *Proceedings of the National Academy of Sciences*, *113*(15), 3932 LP – 3937. https://doi.org/10.1073/pnas.1517384113.

Caponetto, R., Dongola, G., Fortuna, L., & Petráš, I. (2010). *Fractional Order Systems: Modeling and Control Applications*. World Scientific Series on Nonlinear Science: Series A. World Scientific, https://doi.org/10.1142/7709.

Caputo, M. (1967). Linear Models of Dissipation whose Q is almost Frequency Independent-II. *Geophysical Journal of the Royal Astronomical Society*, *13*(5), 529–539. https://doi.org/10.1111/j.1365-246X.1967.tb02303.x.

Castillo, F. J. (2010). *Metodología de Diseño de Reguladores de Orden Fraccional a Partir de Especificaciones Temporales. Aplicación a Canales Principales de Riego.* [Tesis de doctorado, Universidad de Castilla-La Mancha]. https://hdl.handle.net/10578/2819.

Chen, H.-C. & Bai, Y.-W. (2021). Improvement of a High-Current-Density Power Backplane Design With a PID Fan Control Cooling System on an Enterprise Server. *IEEE Canadian Journal of Electrical and Computer Engineering*, *44*(1), 1–9. https://doi.org/10.1109/icjece.2020.3011357.

Chen, X., Park, J. H., Cao, J., & Qiu, J. (2017). Sliding mode synchronization of multiple chaotic systems with uncertainties and disturbances. *Applied Mathematics and Computation*, *308*, 161–173. https://doi.org/10.1016/j.amc.2017.03.032.

Cottee, C. J. & Duncan, S. R. (2003). Design of matching circuit controllers for radio-frequency heating. *IEEE Transactions on Control Systems Technology*, *11*(1), 91–100. https://doi.org/10.1109/TCST.2002.806447.

Coumou, D. J. (2012). Feedforward power distortion correction in RF power delivery systems for plasma processing systems. In *2012 18th IEEE-NPSS Real Time Conference*, 1–5. IEEE. https://doi.org/10.1109/RTC.2012.6418192.

Coumou, D. J. (2013). Coherent feedforward impedance correction and feedback power regulation in a plasma processing RF power delivery system. In *2013 IEEE 14th Workshop on Control and Modeling for Power Electronics (COMPEL)*, 1–4. IEEE. https://doi.org/10.1109/COMPEL.2013.6626421.

Danca, M.-F. & Kuznetsov, N. (2018). Matlab code for Lyapunov exponents of fractional order systems. *International Journal of Bifurcation and Chaos*, *8*(5). https://doi.org/10.1142/S0218127418500670.

Deng, H., Li, T., Wang, Q., & Li, H. (2009). A fractional-order hyperchaotic system and its synchronization. *Chaos, Solitons and Fractals*, *41*(2), 962–969. https://doi.org/10.1016/j.chaos.2008.04.034.

Deng, W. & Lü, J. (2007). Generating multi-directional multi-scroll chaotic attractors via a fractional differential hysteresis system. *Physics Letters A*, *369*(5), 438–443. https://doi.org/10.1016/j.physleta.2007.04.112.

Deng, W. H. & Li, C. P. (2005). Chaos synchronization of the fractional Lü system. *Physica A: Statistical Mechanics and its Applications*, *353*(1-4), 61–72. https://doi.org/10.1016/j.physa.2005.01.021.

Diethelm, K., Ford, N. J., & Freed, A. D. (2002). A Predictor-Corrector Approach for the Numerical Solution of Fractional Differential Equations. *Nonlinear Dynamics*, *29*, 3–22. https://doi.org/10.1023/A:1016592219341.

Dik, D., Polyakova, E., Chelovechkova, A., Moskvin, V., & Nikiforova, T. (2018). The system of environment control of botanic garden greenhouses. In *2018 International Multi-Conference on Industrial Engineering and Modern Technologies (FarEastCon)*, 1–7. https://doi.org/10.1109/FarEastCon.2018.8602559.

Diversi, R., Bartolini, A., & Benini, L. (2020). Thermal Model Identification of Computing Nodes in High-Performance Computing Systems. *IEEE Transactions on Industrial Electronics*, *67*(9), 7778–7788. https://doi.org/10.1109/TIE.2019.2945277.

Du, J., Zhang, X., & Shi, J. (2019). A condition change detection method for solar conversion efficiency in solar cell manufacturing processes. *IEEE Transactions on Semiconductor Manufacturing*, *32*(1), 82–92. https://doi.org/10.1109/TSM.2018.2875011.

Duarte, V. (2023). Toolbox ninteger for matlab, v. 2.3. https://web.ist.utl.pt/duarte.valerio/ninteger/ninteger.htm.

Echegoyen, I., Vera-Ávila, V., Sevilla-Escoboza, R., Martínez, J., & Buldú, J. (2019). Ordinal synchronization: Using ordinal patterns to capture interdependencies between time series. *Chaos, Solitons & Fractals*, *119*, 8–18. https://doi.org/10.1016/j.chaos.2018.12.006.

Echenausía-Monroy, J. L., Rodríguez-Martíne, C. A., Ontañón-García, L. J., Alvarez, J., & Peña Ramirez, J. (2021). Synchronization in Dynamically Coupled Fractional-Order Chaotic Systems: Studying the Effects of Fractional Derivatives. *Complexity*, *2021*. https://doi.org/10.1155/2021/7242253.

Edelman, M., Macau, E., & Sanjuán, M. (2018). *Chaotic, Fractional, and Complex Dynamics: New Insights and Perspectives*. Springer Cham, https://doi.org/10.1007/978-3-319-68109-2.

Farsi, M., Daneshkhah, A., Hosseinian-Far, A., & Jahankhani, H., editors (2020). *Digital Twin Technologies and Smart Cities*. Springer Cham, https://doi.org/10.1007/978-3-030-18732-3.

Feki, M. (2003). An adaptive chaos synchronization scheme applied to secure communication. *Chaos, Solitons & Fractals*, *18*(1), 141–148. https://doi.org/10.1016/S0960-0779(02)00585-4.

Femat, R. & Solis-Perales, G. (2008). *Robust Synchronization of Chaotic Systems via Feedback*. Springer, https://doi.org/10.1007/978-3-540-69307-9.

Firrao, E., Annema, A.-J., & Nauta, B. (2008). An Automatic Antenna Tuning System Using Only RF Signal Amplitudes. *IEEE Transactions on Circuits and Systems II: Express Briefs*, *55*(9), 833–837. https://doi.org/10.1109/TCSII.2008.925652.

Garrappa, R. (2018). Numerical solution of fractional differential equations: A survey and a software tutorial. *Mathematics*, *6*(2). https://doi.org/10.3390/math6020016.

Georgiou, T. T. & Smith, M. C. (1990). Optimal Robustness in the Gap Metric. *IEEE Transactions on Automatic Control*, *35*(6), 673–686. https://doi.org/10.1109/9.53546.

Grieves, M. (2015). Digital twin: Manufacturing excellence through virtual factory replication. White paper, https://bit.ly/3JbJede.

Grünwald, A. K. (1867). Uber begrenzte Derivationen und deren Anwendung. *Z. Angew. Math. Phys.*, *12*, 441–480. PDF file.

Guida, P., Saxena, S., & Roberts, W. L. (2021). Analysis of Thermally Induced Breakup of Ultrasonically Emulsified Heavy Fuel Oil using Dynamic Mode Decomposition. *International Journal of Heat and Mass Transfer*, *166*. https://doi.org/10.1016/j.ijheatmasstransfer.2020.120815.

Hanaoka, K., Takahashi, K., & Ando, A. (2020). Reproducibility of a Plasma Production in a Fast- and Automatically-controlled Radio Frequency Plasma Source. *IEEE Transactions on Plasma Science*, *48*(6), 2138–2142. https://doi.org/10.1109/TPS.2020.2987554.

He, J. M. & Chen, F. Q. (2017). A new fractional order hyperchaotic Rabinovich system and its dynamical behaviors. *International Journal of Non-Linear Mechanics*, *95*(March), 73–81. https://doi.org/10.1016/j.ijnonlinmec.2017.05.013.

Hirose, Y., Kawamura, A., Takayanagi, A., & Takada, H. (2009). Analysis of impedance matching control. In *2009 IEEE 6th International Power Electronics and Motion Control Conference*, 1188–1191. https://doi.org/10.1109/IPEMC.2009.5157563.

Huygens, C. (1673). *Horologium Oscillatorium*. PDF file.

Ishida, S., Kawamura, A., Takayanagi, A., & Takada, H. (2011). Robust convergence of the impedance matching process based on seek control. In *IECON 2011 - 37th Annual Conference of the IEEE Industrial Electronics Society*, 1554–1559. https://doi.org/10.1109/IECON.2011.6119538.

Jain, V., Patnaik, S., Popențiu Vlădicescu, F., & Sethi, I. K., editors (2019). *Recent Trends in Intelligent Computing, Communication and Devices*. Springer Singapore, https://doi.org/10.1007/978-981-13-9406-5.

Jeong, S., Ji, D., Park, J. H., & Won, S. (2013). Adaptive synchronization for uncertain chaotic neural networks with mixed time delays using fuzzy disturbance observer. *Applied Mathematics and Computation*, *219*(11), 5984–5995. https://doi.org/10.1016/j.amc.2012.12.017.

Jurkov, A. S., Radomski, A., & Perreault, D. J. (2020). Tunable Matching Networks Based on Phase-Switched Impedance Modulation1. *IEEE Transactions on Power Electronics*, *35*(10), 10150–10167. https://doi.org/10.1109/TPEL.2020.2980214.

Kamesh, R. & Rani, K. Y. (2017). Novel Formulation of Adaptive MPC as EKF Using ANN Model: Multiproduct Semibatch Polymerization Reactor Case Study. *IEEE Transactions on Neural Networks and Learning Systems*, *28*(12), 3061–3073. https://doi.org/10.1109/TNNLS.2016.2614878.

Kanbur, B. B., Kumtepeli, V., & Duan, F. (2020). Thermal performance prediction of the battery surface via dynamic mode decomposition. *Energy*, *201*. https://doi.org/10.1016/j.energy.2020.117642.

Khalil, H. K. (2015). *Nonlinear Control*. Pearson, Boston.

Khalil, R., Al Horani, M., Yousef, A., & Sababheh, M. (2014). A new definition of fractional derivative. *Journal of Computational and Applied Mathematics*, *264*, 65–70. https://doi.org/10.1016/j.cam.2014.01.002.

Kharabian, B. & Mirinejad, H. (2021). Synchronization of Rossler chaotic systems via hybrid adaptive backstepping/sliding mode control. *Results in Control and Optimization*, *4*, 100020. https://doi.org/10.1016/j.rico.2021.100020.

Kothari, K., Mehta, U., & Prasad, R. (2019). Fractional-Order System Modeling and its Applications. *Journal of Engineering Science and Technology Review*, *12*(6), 1–10. https://doi.org/10.25103/jestr.126.01.

Kulakowski, B. T., Gardner, J. F., & Shearer, J. L. (2007). *Dynamic Modeling and Control of Engineering Systems*, (3a ed.). Cambridge University Press.

Kungwalrut, P., Numsomran, A., Chaiyasith, P., Chaoraingern, J., & Tipsuwanporn, V. (2017). A PIλDμ controller design for peltier-thermoelectric cooling system. In *International Conference on Control, Automation and Systems*, volume 2017-Octob, 766–770. IEEE Computer Society. https://doi.org/10.23919/ICCAS.2017.8204331.

Lafferriere, G. & Sontag, E. (1993). Remarks on control lyapunov functions for discontinuous stabilizing feedback. In *Proceedings of 32nd IEEE Conference on Decision and Control*, volume 1, 306–308. https://doi.org/10.1109/CDC.1993.325127.

Lakshmanan, M. (2005). Nonlinear dynamics: Challenges and perspectives. *Pramana*, *64*(4), 617–632. https://doi.org/10.1007/BF02706208.

Letnikov, A. V. (1868). Theory of differentiation of fractional order. *Matematiceskij Sbornik*, *3*(1), 1–68. PDF file in Russian.

Li, C., Liao, X., & Yu, J. (2003). Synchronization of fractional order chaotic systems. *Physical Review E*, *68*(6), 067203. https://doi.org/10.1103/PhysRevE.68.067203.

Li, Y.-F., Hsieh, M.-H., & Liou, R.-S. (2019). Tracking controller design of a RF matching box with plasma load varying. In *2019 International Aegean Conference on Electrical Machines and Power Electronics (ACEMP) 2019 International Conference on Optimization of Electrical and Electronic Equipment (OPTIM)*, 610–615. https://doi.org/10.1109/ACEMP-OPTIM44294.2019.9007151.

Liu, D. (2008). Synchronization of Discrete Chaotic Dynamical Systems Using Active Control. In *2008 IFIP International Conference on Network and Parallel Computing*, 56–59. https://doi.org/10.1109/NPC.2008.63.

Lu, J. G. (2005). Chaotic dynamics and synchronization of fractional-order chua's circuits with a piecewise-linear nonlinearity. *International Journal of Modern Physics B*, *19*(20), 3249–3259. https://doi.org/10.1142/S0217979205032115.

Lu, J. G. (2006). Chaotic dynamics of the fractional-order Lü system and its synchronization. *Physics Letters, Section A: General, Atomic and Solid State Physics*, *354*(4), 305–311. https://doi.org/10.1016/j.physleta.2006.01.068.

Luong, H. T., Wang, Y., Sung, H.-G., & Sohn, C. H. (2021). A comparative study of dynamic mode decomposition methods for mode identification in a cryogenic swirl injector. *Journal of Sound and Vibration*, *503*, 116108. https://doi.org/10.1016/j.jsv.2021.116108.

Maachou, A., Malti, R., Melchior, P., Battaglia, J.-L., & Hay, B. (2012). Thermal system identification using fractional models for high temperature levels around different operating points. *Nonlinear Dynamics*, *70*(2), 941–950. https://doi.org/10.1007/s11071-012-0507-y.

Madni, A., Madni, C., & Lucero, S. (2019). Leveraging Digital Twin Technology in Model-Based Systems Engineering. *Systems*, *7*(1), 7. `https://doi.org/10.3390/systems7010007`.

Magin, R. (2006). *Fractional Calculus in Bioengineering*. Begell House.

Martínez-Guerra, R. & Pérez-Pinacho, C. A. (2018). *Advances in Synchronization of Coupled Fractional Order Systems*. Springer Cham.

Martínez-Martínez, R., Mata-Machuca, J. L., Martínez-Guerra, R., León, J. A., & Fernández-Anaya, G. (2011). Synchronization of nonlinear fractional order systems. *Applied Mathematics and Computation*, *218*(7), 3338–3347. `https://doi.org/10.1016/j.amc.2011.08.075`.

Martínez-Guerra, R., Pérez-Pinacho, C. A., & Gómez-Cortés, G. C. (2015). *Synchronization of Integer and Fractional Order Chaotic Systems*. Springer Cham.

Mazza, N. M. (1970). Automatic Impedance Matching System for RF Sputtering. *IBM Journal of Research and Development*, *14*(2), 192–193. `https://doi.org/10.1147/rd.142.0192`.

Miller, K. S. & Ross, B. (1993). *An Introduction to the Fractional Calculus and Fractional Differential Equations*. John Wiley & Sons.

Monje, C. A., Chen, Y., Vinagre, B. M., Xue, D., & Feliu, V. (2010). *Fractional-Order Systems and Controls*. Springer.

Moore, K. L., Vincent, T. L., Lashhab, F., & Liu, C. (2011). Dynamic consensus networks with application to the analysis of building thermal processes. *IFAC Proceedings Volumes (IFAC-PapersOnline)*, *44*(1 PART 1), 3078–3083. `https://doi.org/10.3182/20110828-6-IT-1002.02549`.

Moran, M. (2003). *Introduction to Thermal Systems Engineering: Thermodynamics, Fluid Mechanics, and Heat Transfer*. Number v. 1 in Introduction to Thermal Systems Engineering: Thermodynamics, Fluid Mechanics, and Heat Transfer. Wiley.

Muñoz-Pacheco, J. M., Posadas-Castillo, C., & Zambrano-Serrano, E. (2020). The effect of a non-local fractional operator in an asymmetrical glucose-insulin regulatory system: Analysis, synchronization and electronic implementation. *Symmetry*, *12*(9). `https://doi.org/10.3390/sym12091395`.

Nijmeijer, H. (2001). A dynamical control view on synchronization. *Physica D: Nonlinear Phenomena*, *154*(3-4), 219–228. `https://doi.org/10.1016/S0167-2789(01)00251-2`.

Odibat, Z. M., Bertelle, C., Aziz-Alaoui, M., & Duchamp, G. H. (2010). A multi-step differential transform method and application to non-chaotic or chaotic systems. *Computers & Mathematics with Applications*, *59*(4), 1462–1472. `https://doi.org/10.1016/J.CAMWA.2009.11.005`.

Oldham, K. B. & Spanier, J. (1974). *The Fractional Calculus : Theory and Applications of Differentiation and Integration to Arbitrary Order*. Academic Press.

Olfati-Saber, R., Fax, J. A., & Murray, R. M. (2007). Consensus and cooperation in networked multi-agent systems. *Proceedings of the IEEE*, *95*(1), 215–233. `https://doi.org/10.1109/JPROC.2006.887293`.

Oustaloup, A., Melchior, P., Lanusse, P., Cois, O., & Dancla, F. (2000). The CRONE toolbox for Matlab. In *CACSD. Conference Proceedings. IEEE International Symposium on Computer-Aided Control System Design (Cat. No.00TH8537)*, 190–195. `https://doi.org/10.1109/CACSD.2000.900210`.

Park, J. H. (2005). Adaptive synchronization of Rossler system with uncertain parameters. *Chaos, Solitons & Fractals*, *25*(2), 333–338. https://doi.org/10.1016/j.chaos.2004.12.007.

Peña Ramirez, J., Arellano-Delgado, A., & Nijmeijer, H. (2018). Enhancing master-slave synchronization: The effect of using a dynamic coupling. *Phys. Rev. E*, *98*, 012208. https://doi.org/10.1103/PhysRevE.98.012208.

Peña Ramirez, J., Garcia, E., & Alvarez, J. (2020). Master-slave synchronization via dynamic control. *Communications in Nonlinear Science and Numerical Simulation*, *80*, 104977. https://doi.org/https://doi.org/10.1016/j.cnsns.2019.104977.

Pecora, L. M. & Carroll, T. L. (1990). Synchronization in chaotic systems. *Physical Review Letters*, *64*(8), 821–824. https://doi.org/10.1103/PhysRevLett.64.821.

Pecora, L. M., Carroll, T. L., Johnson, G. A., Mar, D. J., & Heagy, J. F. (1997). Fundamentals of synchronization in chaotic systems, concepts, and applications. *Chaos: An Interdisciplinary Journal of Nonlinear Science*, *7*(4), 520–543. https://doi.org/10.1063/1.166278.

Peltier, J. C. A. (1834). *Nouvelles Experiences sur la Caloricite des Courans Electriques*, (1era ed.). Bailly.

Peng, G. (2007). Synchronization of fractional order chaotic systems. *Physics Letters, Section A: General, Atomic and Solid State Physics*, *363*(5-6), 426–432. https://doi.org/10.1016/j.physleta.2006.11.053.

Petráš, I. (2006). Method for simulation of the fractional order chaotic systems. *Acta Montanistica Slovaca*, *11*, 273–277. PDF file.

Petráš, I. (2011). *Fractional-Order Nonlinear Systems*. Springer Berlin, https://doi.org/10.1007/978-3-642-18101-6.

Pikovsky, A., Rosenblum, M., & Kurths, J. J. (2001). *Synchronization : A Universal Concept in Nonlinear Sciences*. Cambridge University Press.

Ping, Z., Yuan-Ming, C., & Fei, K. (2010). Synchronization between fractional-order chaotic systems and integer orders chaotic systems (fractional-order chaotic systems). *Chinese Physics B*, *19*(9), 090503. https://doi.org/10.1088/1674-1056/19/9/090503.

Pittino, F., Diversi, R., Benini, L., & Bartolini, A. (2020). Robust identification of thermal models for in-production high-performance-computing clusters with machine learning-based data selection. *IEEE Transactions on Computer-Aided Design of Integrated Circuits and Systems*, *39*(10), 2042–2054. https://doi.org/10.1109/TCAD.2019.2950378.

Podlubny, I. (1999). *Fractional Differential Equations*. Academic Press.

Pogromsky, A. (2002). Synchronization and adaptive synchronization in semi-passive systems. In *1997 1st International Conference, Control of Oscillations and Chaos Proceedings (Cat. No.97TH8329)*, volume 1, 64–68. IEEE. https://doi.org/10.1109/coc.1997.633478.

Priyanga, V. T., Chandni, M., Mohan, N., & Soman, K. P. (2019). Data-driven analysis for low frequency oscillation identification in smart grid using FB-DMD and T-DMD methods. *Proceedings of the 2019 9th International Conference on Advances in Computing and Communication, ICACC 2019*, 51–57. https://doi.org/10.1109/ICACC48162.2019.8986168.

Qi, Q. & Tao, F. (2018). Digital Twin and Big Data Towards Smart Manufacturing and Industry 4.0: 360 Degree Comparison. *IEEE Access*, *6*, 3585–3593. https://doi.org/10.1109/ACCESS.2018.2793265.

Qi, Q., Tao, F., Hu, T., Anwer, N., Liu, A., Wei, Y., Wang, L., & Nee, A. (2019). Enabling technologies and tools for digital twin. *Journal of Manufacturing Systems*. https://doi.org/10.1016/j.jmsy.2019.10.001.

Qiu, L. & Zhao, D. (2021). *Robust Control in Gap Metric*. Springer Cham, https://doi.org/10.1007/978-3-030-44184-5_165.

Rajagopal, K., Karthikeyan, A., & Srinivasan, A. K. (2017). FPGA implementation of novel fractional-order chaotic systems with two equilibriums and no equilibrium and its adaptive sliding mode synchronization. *Nonlinear Dynamics*, *87*(4), 2281–2304. https://doi.org/10.1007/s11071-016-3189-z.

Razminia, A., Majd, V., & Baleanu, D. (2011). Chaotic incommensurate fractional order Rössler system: active control and synchronization. *Advances in Difference Equations*, *2011*, 15. https://doi.org/10.1186/1687-1847-2011-15.

Rodriguez, C., Viola, J., & Chen, Y. (2021). Data-Driven Modelling for a High Order Multivariable Thermal System and Control. *IFAC-PapersOnLine*, *54*(20), 753–758. https://doi.org/10.1016/j.ifacol.2021.11.262.

Rodriguez, C. A. (2020). Peltier MIMO identification data. https://www.mathworks.com/matlabcentral/fileexchange/75172-peltier-mimo-identification-data.

Rodriguez, C. A. (2021). Data-driven model for high order multi-variable thermal system and contro. https://youtu.be/S3CLKOC3QHw.

Roessler, J., Fisher, A., Egbert, A., Missen, Z. V., Hoosier, T. V., Baylis, C., Khater, M. A., Peroulis, D., & Marks, R. J. (2023). A Plasma-Switch Impedance Tuner With Microsecond Reconfiguration. *IEEE Transactions on Microwave Theory and Techniques*, *71*(1), 296–308. https://doi.org/10.1109/TMTT.2022.3223344.

Shin, D. & Hong, S. J. (2023). Improved impedance matching speed with gradient descent for advanced RF plasma system. *Journal of Vacuum Science & Technology B*, *41*(6), 064002. https://doi.org/10.1116/6.0003034.

Sontag, E. D. (1989). A 'universal' construction of Artstein's theorem on nonlinear stabilization. *Systems & Control Letters*, *13*(2), 117–123. https://doi.org/10.1016/0167-6911(89)90028-5.

Stevens, A., Agoro, S., & Husain, I. (2020). Data-Driven Current Control of the PMSM with Dynamic Mode Decomposition and the Linear Quadratic Integrator. *Conference Proceedings - IEEE Applied Power Electronics Conference and Exposition - APEC*, *2020-March*, 271–278. https://doi.org/10.1109/APEC39645.2020.9124408.

Su, Y., Yu, Q., & Zeng, L. (2020). Parameter Self-Tuning PID Control for Greenhouse Climate Control Problem. *IEEE Access*, *8*, 186157–186171. https://doi.org/10.1109/ACCESS.2020.3030416.

Sun, C., Tian, T., Zhu, X., & Du, Z. (2020a). Input-output reduced-order modeling of unsteady flow over an airfoil at a high angle of attack based on dynamic mode decomposition with control. *International Journal of Heat and Fluid Flow*, *86*(August). https://doi.org/10.1016/j.ijheatfluidflow.2020.108727.

Sun, T., Yang, R., Li, H., Zhang, X., & Xu, T. (2020b). Active motor rotor temperature management based on one-node thermal network model predictive control. *IEEE Transactions on Power Electronics*, *35*(10), 11213–11221. https://doi.org/10.1109/TPEL.2020.2979824.

Takahashi, K., Wen, S., Sanada, M., & Deng, M. (2012). Nonlinear cooling control for a peltier actuated aluminum plate thermal system by considering radiation heat transfer. In *The 2012 International Conference on Advanced Mechatronic Systems*, 18–23.

Tao, F. & Qi, Q. (2019). Make more digital twins. *Nature*, *573*(7775), 490–491. https://doi.org/10.1038/d41586-019-02849-1.

Tarasov, V. E. & Zaslavsky, G. M. (2006). Fractional dynamics of coupled oscillators with long-range interaction. *Chaos: An Interdisciplinary Journal of Nonlinear Science*, *16*(2), 023110. https://doi.org/10.1063/1.2197167.

Tavazoei, M. S. & Haeri, M. (2008a). Chaotic attractors in incommensurate fractional order systems. *Physica D: Nonlinear Phenomena*, *237*(20), 2628–2637. https://doi.org/10.1016/j.physd.2008.03.037.

Tavazoei, M. S. & Haeri, M. (2008b). Synchronization of chaotic fractional-order systems via active sliding mode controller. *Physica A: Statistical Mechanics and its Applications*, *387*(1), 57–70. https://doi.org/10.1016/j.physa.2007.08.039.

Tepljakov, A. (2017). *FOMCON: Fractional-Order Modeling and Control Toolbox*, (pp. 107–129). Springer International Publishing, Cham, https://doi.org/10.1007/978-3-319-52950-9_6.

Thompson, M. & Fidler, J. (2004). Determination of the impedance matching domain of impedance matching networks. *IEEE Transactions on Circuits and Systems I: Regular Papers*, *51*(10), 2098–2106. https://doi.org/10.1109/TCSI.2004.835682.

Vai, M. & Prasad, S. (1993). Automatic Impedance Matching with a Neural Network. *IEEE Microwave and Guided Wave Letters*, *3*(10), 353–354. https://doi.org/10.1109/75.242258.

van Bezooijen, A., de Jongh, M., van Straten, F., Mahmoudi, R., & van Roermund, A. (2010). Adaptive Impedance-Matching Techniques for Controlling L Networks. *IEEE Transactions on Circuits and Systems I: Regular Papers*, *57*(2), 495–505. https://doi.org/10.1109/TCSI.2009.2023764.

Vinnicombe, G. (1993). Frequency domain uncertainty and the graph topology. *IEEE Transactions on Automatic Control*, *38*(9), 1371–1383. https://doi.org/10.1109/9.237648.

Viola, J. & Chen, Y. (2023). *Digital Twin Enabling Capabilities*, (pp. 47–71). Springer International Publishing, Cham, https://doi.org/10.1007/978-3-031-22140-8_3.

Viola, J., Hollenbeck, D., Rodriguez, C., & Chen, Y. (2021). Fractional-Order Stochastic Extremum Seeking Control with Dithering Noise for Plasma Impedance Matching. In *2021 IEEE Conference on Control Technology and Applications (CCTA)*, 247–252. https://doi.org/10.1109/CCTA48906.2021.9658616.

Viola, J., Rodriguez, C., & Chen, Y. (2020). Phelp: Pixel heating experiment learning platform for education and research on iai-based smart control engineering. https://arxiv.org/abs/2007.03048.

Wang, J., Xu, D., Zhou, H., & Zhou, T. (2018). Adaptive fractional order sliding mode control for Boost converter in the Battery/Supercapacitor HESS. *PLoS ONE*, *13*(4), 9. https://doi.org/10.1371/journal.pone.0196501.

Wang, X.-y. & Wang, M.-j. (2007). Dynamic analysis of the fractional-order Liu system and its synchronization. *Chaos: An Interdisciplinary Journal of Nonlinear Science*, *17*(3), 033106. https://doi.org/10.1063/1.2755420.

Wen, S., Liu, P., Wang, D., & Cao, F. (2014). Optimal tracking control for a peltier refrigeration system based on PSO. In *International Conference on Advanced Mechatronic Systems, ICAMechS*, 567–571. IEEE Computer Society. https://doi.org/10.1109/ICAMechS.2014.6911610.

Wolf, A., Swift, J. B., Swinney, H. L., & Vastano, J. A. (1985). Determining lyapunov exponents from a time series. *Physica D: Nonlinear Phenomena*, *16*(3), 285–317. https://doi.org/https://doi.org/10.1016/0167-2789(85)90011-9.

Wu, X., Bao, H., & Cao, J. (2021). Finite-time inter-layer projective synchronization of caputo fractional-order two-layer networks by sliding mode control. *Journal of the Franklin Institute*, *358*(1), 1002–1020. https://doi.org/https://doi.org/10.1016/j.jfranklin.2020.10.043.

Xin Gao & Juebang Yu (2005). Synchronization of fractional-order chaotic.systems. In *Proceedings. 2005 International Conference on Communications, Circuits and Systems, 2005.*, volume 2, 1169–1172, Hong Kong, China. IEEE. https://doi.org/10.1109/ICCCAS.2005.1495316.

Xiong, B. & Hofmann, K. (2016). Binary search algorithm for adaptive impedance matching network. *Electronics Letters*, *52*(9), 714–716. https://doi.org/10.1049/el.2015.3830.

Xiong, B., Yang, L., & Cao, T. (2020). A Novel Tuning Method for Impedance Matching Network Based on Linear Fractional Transformation. *IEEE Transactions on Circuits and Systems II: Express Briefs*, *67*(6), 1039–1043. https://doi.org/10.1109/TCSII.2019.2931412.

Xiong, P.-Y., Jahanshahi, H., Alcaraz, R., Chu, Y.-M., Gómez-Aguilar, J., & Alsaadi, F. E. (2021). Spectral entropy analysis and synchronization of a multi-stable fractional-order chaotic system using a novel neural network-based chattering-free sliding mode technique. *Chaos, Solitons & Fractals*, *144*, 110576. https://doi.org/https://doi.org/10.1016/j.chaos.2020.110576.

Yang, S., Hu, C., Yu, J., & Jiang, H. (2021). Finite-time cluster synchronization in complex-variable networks with fractional-order and nonlinear coupling. *Neural Networks*, *135*, 212–224. https://doi.org/https://doi.org/10.1016/j.neunet.2020.12.015.

Yassen, M. T. (2005). Chaos synchronization between two different chaotic systems using active control. *Chaos, Solitons and Fractals*, *23*(1), 131–140. https://doi.org/10.1016/j.chaos.2004.03.038.

Yu, Y. & Zhang, S. (2004). Adaptive backstepping synchronization of uncertain chaotic system. *Chaos, Solitons & Fractals*, *21*(3), 643–649. https://doi.org/10.1016/j.chaos.2003.12.067.

Yubo, D., Sai, Y., & Bin, L. (2013). Multi-model optimal robust control of nonlinear systems in gap metric. In *Proceedings of 2013 2nd International Conference on Measurement, Information and Control*, volume 02, 1255–1259. https://doi.org/10.1109/MIC.2013.6758187.

Zhang, C. & Ordóñez, R. (2012). Impedance Matching in Semiconductor Plasma Processing Chamber. In Zhang, C. & Ordóñez, R., editors, *Extremum-Seeking Control and Applications: A Numerical Optimization-Based Approach*, Advances in Industrial Control, (pp. 133–153). Springer, London. https://doi.org/10.1007/978-1-4471-2224-1_7.

Zhang, Q., Chen, S., Hu, Y., & Wang, C. (2006). Synchronizing the noise-perturbed unified chaotic system by sliding mode control. *Physica A: Statistical Mechanics and its Applications*, *371*(2), 317–324. https://doi.org/10.1016/J.PHYSA.2006.03.057.

Zhang, S., Zhao, D., Spurgeon, S. K., & Yan, X. (2016). Distributed model predictive control for the atmospheric and vacuum distillation towers in a petroleum refining process. In *2016 UKACC 11th International Conference on Control (CONTROL)*, 1–6. https://doi.org/10.1109/CONTROL.2016.7737534.

Zheng, W. & Zhang, G. (2018). Complete Synchronization of Finance Chaotic System with Disturbance by Using ADRC. In *2018 37th Chinese Control Conference (CCC)*, 1040–1045. https://doi.org/10.23919/ChiCC.2018.8484141.

Appendix

Matrices A and B obtained with DMDc Algorithm (3)

$$
A_H = \begin{bmatrix}
-0.04 & -0.036 & -0.01 & 0.016 & -0.006 & -0.001 & -0.019 & 0.013 & -0.028 & -0.001 & 0 & 0.032 & 0.017 & 0.043 & 0.012 & -0.008 \\
-0.005 & -0.049 & -0.009 & 0.01 & -0.014 & -0.017 & -0.005 & 0.016 & 0.009 & -0.013 & -0.002 & 0.011 & 0.026 & 0.007 & 0.032 & -0.016 \\
0.022 & -0.005 & -0.055 & -0.008 & -0.024 & 0.002 & -0.011 & 0.006 & -0.003 & 0.009 & -0.013 & 0.016 & -0.015 & 0.045 & 0.015 & 0.002 \\
0.006 & 0.023 & 0.011 & -0.098 & -0.003 & -0.018 & 0.033 & -0.005 & 0.027 & -0.03 & 0.007 & 0.007 & -0.018 & 0.023 & 0.007 & 0.012 \\
0.048 & -0.009 & -0.025 & 0.026 & -0.091 & -0.023 & -0.005 & 0.019 & -0.056 & -0.008 & -0.001 & 0.009 & 0.029 & 0.051 & 0.017 & 0.004 \\
0.053 & 0.016 & 0.02 & 0.003 & -0.022 & -0.133 & 0.005 & 0.028 & -0.021 & -0.018 & -0.021 & -0.022 & 0.015 & 0.039 & 0.011 & 0.028 \\
0.012 & 0.036 & -0.005 & -0.001 & -0.017 & -0.019 & -0.029 & -0.007 & 0.022 & -0.032 & -0.035 & -0.009 & -0.005 & 0.032 & 0.006 & 0.032 \\
0.002 & 0.023 & 0.006 & -0.014 & -0.023 & -0.015 & -0.011 & -0.034 & 0.042 & -0.007 & 0.018 & -0.026 & -0.005 & 0.017 & 0.022 & -0.013 \\
0.042 & 0.011 & -0.013 & 0.015 & -0.025 & -0.02 & 0.005 & 0.024 & -0.123 & -0.027 & -0.014 & 0.006 & 0.026 & 0.049 & 0.013 & 0.013 \\
0.028 & 0.036 & 0.052 & -0.016 & -0.01 & -0.031 & 0.002 & 0.012 & -0.038 & -0.107 & -0.034 & -0.008 & 0.042 & 0 & 0.002 & 0.051 \\
0.015 & 0.046 & 0.014 & -0.002 & -0.011 & -0.024 & -0.015 & 0.021 & 0.016 & -0.028 & -0.083 & -0.028 & 0.003 & 0.015 & 0.017 & 0.027 \\
0.005 & 0.023 & 0.017 & 0.014 & -0.023 & -0.028 & -0.009 & -0.009 & 0.025 & 0.01 & -0.013 & -0.045 & 0.016 & 0.004 & 0.028 & -0.034 \\
0.032 & 0.025 & -0.002 & 0.002 & -0.005 & -0.026 & 0.006 & 0.012 & -0.029 & 0.003 & -0.022 & -0.008 & -0.051 & 0.004 & -0.013 & 0.055 \\
0.026 & 0.013 & 0.036 & -0.009 & -0.014 & -0.015 & 0.012 & 0.013 & 0.01 & -0.049 & -0.013 & -0.016 & 0.011 & -0.044 & -0.009 & 0.029 \\
-0.002 & 0.045 & 0.011 & -0.004 & -0.011 & -0.017 & -0.011 & 0.015 & 0.019 & -0.011 & -0.002 & 0.002 & 0.017 & 0.004 & -0.077 & 0.006 \\
0.008 & 0.018 & 0.013 & 0.014 & -0.025 & -0.024 & 0.006 & 0.017 & -0.004 & 0.021 & 0 & -0.032 & 0.043 & -0.003 & -0.003 & -0.066
\end{bmatrix},
$$

$$
B_H = \begin{bmatrix}
0.095 & 0.018 & 0.095 & 0.006 & 0.095 & 0.015 & 0.006 & 0.018 & 0.095 & 0.015 & 0.006 & 0.018 & 0.015 & 0.006 & 0.018 & 0.015 \\
0.07 & 0.027 & 0.07 & 0.021 & 0.07 & 0.021 & 0.021 & 0.027 & 0.07 & 0.021 & 0.021 & 0.027 & 0.021 & 0.021 & 0.027 & 0.021 \\
0.061 & 0.024 & 0.061 & 0.033 & 0.061 & 0.017 & 0.033 & 0.024 & 0.061 & 0.017 & 0.033 & 0.024 & 0.017 & 0.033 & 0.024 & 0.017 \\
0.023 & 0.028 & 0.023 & 0.06 & 0.023 & 0.019 & 0.06 & 0.028 & 0.023 & 0.019 & 0.06 & 0.028 & 0.019 & 0.06 & 0.028 & 0.019 \\
0.11 & 0.005 & 0.11 & 0.001 & 0.11 & 0.036 & 0.001 & 0.005 & 0.11 & 0.036 & 0.001 & 0.005 & 0.036 & 0.001 & 0.005 & 0.036 \\
0.059 & 0.019 & 0.059 & 0.028 & 0.059 & 0.06 & 0.028 & 0.019 & 0.059 & 0.06 & 0.028 & 0.019 & 0.06 & 0.028 & 0.019 & 0.06 \\
0.03 & 0.037 & 0.03 & 0.051 & 0.03 & 0.036 & 0.051 & 0.037 & 0.03 & 0.036 & 0.051 & 0.037 & 0.036 & 0.051 & 0.037 & 0.036 \\
0.017 & 0.05 & 0.017 & 0.043 & 0.017 & 0.025 & 0.043 & 0.05 & 0.017 & 0.025 & 0.043 & 0.05 & 0.025 & 0.043 & 0.05 & 0.025 \\
0.091 & -0.002 & 0.091 & 0.011 & 0.091 & 0.057 & 0.011 & -0.002 & 0.091 & 0.057 & 0.011 & -0.002 & 0.057 & 0.011 & -0.002 & 0.057 \\
0.037 & 0.017 & 0.037 & 0.055 & 0.037 & 0.066 & 0.055 & 0.017 & 0.037 & 0.066 & 0.055 & 0.017 & 0.066 & 0.055 & 0.017 & 0.066 \\
0.011 & 0.037 & 0.011 & 0.059 & 0.011 & 0.053 & 0.059 & 0.037 & 0.011 & 0.053 & 0.059 & 0.037 & 0.053 & 0.059 & 0.037 & 0.053 \\
0.008 & 0.054 & 0.008 & 0.036 & 0.008 & 0.043 & 0.036 & 0.054 & 0.008 & 0.043 & 0.036 & 0.054 & 0.043 & 0.036 & 0.054 & 0.043 \\
0.038 & 0.012 & 0.038 & 0.04 & 0.038 & 0.057 & 0.04 & 0.012 & 0.038 & 0.057 & 0.04 & 0.012 & 0.057 & 0.04 & 0.012 & 0.057 \\
0.012 & 0.03 & 0.012 & 0.05 & 0.012 & 0.062 & 0.05 & 0.03 & 0.012 & 0.062 & 0.05 & 0.03 & 0.062 & 0.05 & 0.03 & 0.062 \\
0.003 & 0.045 & 0.003 & 0.044 & 0.003 & 0.054 & 0.044 & 0.045 & 0.003 & 0.054 & 0.044 & 0.045 & 0.054 & 0.044 & 0.045 & 0.054 \\
0.01 & 0.055 & 0.01 & 0.024 & 0.01 & 0.05 & 0.024 & 0.055 & 0.01 & 0.05 & 0.024 & 0.055 & 0.05 & 0.024 & 0.055 & 0.05
\end{bmatrix},
$$

$$
A_C = \begin{bmatrix}
-0.052 & -0.027 & -0.008 & 0.017 & -0.004 & -0.011 & -0.015 & -0.006 & -0.014 & 0.038 & 0.004 & 0.024 & 0.002 & 0.001 & 0.017 & 0.009 \\
0.01 & -0.073 & -0.002 & 0.006 & -0.021 & 0.008 & -0.016 & -0.01 & -0.003 & -0.008 & 0.04 & 0.003 & 0.019 & -0.031 & 0.031 & 0.023 \\
-0.004 & -0.02 & -0.045 & -0.003 & -0.002 & 0.02 & -0.015 & 0.011 & -0.003 & 0.014 & 0.003 & 0.015 & -0.009 & 0.016 & -0.003 & 0.005 \\
0.013 & -0.012 & 0.006 & -0.058 & 0.007 & 0.023 & 0.016 & -0.01 & 0.004 & -0.019 & 0.001 & -0.019 & -0.013 & 0.024 & 0.013 & 0.005 \\
0.018 & -0.026 & 0.009 & 0.033 & -0.071 & -0.004 & -0.021 & -0.002 & -0.043 & 0.002 & 0.03 & 0.001 & 0.014 & 0.017 & 0.017 & 0 \\
0.015 & 0.01 & 0.037 & 0.029 & 0.003 & -0.104 & 0.003 & -0.027 & -0.008 & -0.023 & -0.002 & 0.01 & -0.004 & 0.005 & 0.021 & 0.011 \\
0.011 & -0.004 & 0.014 & 0.007 & -0.008 & 0.017 & -0.061 & -0.011 & 0.018 & 0.003 & -0.019 & 0.01 & -0.029 & 0.008 & 0.001 & 0.022 \\
0.015 & -0.004 & 0.023 & -0.02 & 0 & -0.003 & -0.009 & -0.049 & -0.013 & 0.011 & 0.016 & -0.016 & 0.002 & 0.012 & 0.015 & 0 \\
0.019 & 0.004 & 0.008 & 0.03 & -0.025 & -0.005 & 0.018 & -0.014 & -0.099 & -0.014 & 0.012 & -0.003 & 0.014 & 0.003 & 0.013 & 0.013 \\
0.044 & -0.009 & 0.033 & -0.003 & 0.001 & -0.006 & 0.019 & 0.019 & -0.012 & -0.076 & -0.013 & -0.013 & -0.022 & -0.023 & 0.013 & 0.025 \\
0.005 & 0.023 & 0.016 & -0.012 & 0.018 & 0.02 & -0.023 & 0.009 & 0.006 & -0.025 & -0.047 & 0.001 & -0.031 & 0.008 & -0.004 & 0.016 \\
0.018 & 0.002 & 0.018 & -0.018 & -0.014 & 0.014 & 0.008 & -0.018 & -0.01 & -0.002 & 0.01 & -0.029 & 0.004 & 0.006 & 0.019 & -0.028 \\
0.012 & 0.007 & 0.007 & 0.004 & 0.005 & 0.023 & -0.003 & 0.01 & 0.006 & 0.004 & -0.005 & 0.004 & -0.1 & -0.005 & -0.002 & 0.009 \\
0.014 & -0.026 & 0.022 & 0.03 & 0.01 & 0.023 & 0.003 & 0.007 & 0.005 & -0.02 & 0.013 & -0.011 & -0.011 & -0.083 & 0 & 0.002 \\
0.009 & 0.02 & 0 & 0.004 & 0.007 & 0.024 & 0.004 & 0.01 & 0.002 & -0.002 & -0.003 & 0.003 & -0.025 & -0.01 & -0.087 & 0.022 \\
0.008 & 0.016 & 0.006 & 0.002 & -0.021 & 0.016 & 0.012 & 0.009 & 0.01 & 0.011 & 0.004 & -0.031 & -0.006 & -0.005 & 0.02 & -0.07
\end{bmatrix},
$$

$$
B_C = \begin{bmatrix}
0.046 & 0.016 & 0.046 & 0.006 & 0.046 & 0.006 & 0.006 & 0.016 & 0.046 & 0.006 & 0.006 & 0.016 & 0.006 & 0.006 & 0.016 & 0.006 \\
0.04 & 0.02 & 0.04 & 0.012 & 0.04 & 0.004 & 0.012 & 0.02 & 0.04 & 0.004 & 0.012 & 0.02 & 0.004 & 0.012 & 0.02 & 0.004 \\
0.028 & 0.017 & 0.028 & 0.015 & 0.028 & 0.008 & 0.015 & 0.017 & 0.028 & 0.008 & 0.015 & 0.017 & 0.008 & 0.015 & 0.017 & 0.008 \\
0.01 & 0.021 & 0.01 & 0.022 & 0.01 & 0.008 & 0.022 & 0.021 & 0.01 & 0.008 & 0.022 & 0.021 & 0.008 & 0.022 & 0.021 & 0.008 \\
0.05 & 0.013 & 0.05 & 0.001 & 0.05 & 0.021 & 0.001 & 0.013 & 0.05 & 0.021 & 0.001 & 0.013 & 0.021 & 0.001 & 0.013 & 0.021 \\
0.028 & 0.012 & 0.028 & 0.012 & 0.028 & 0.034 & 0.012 & 0.012 & 0.028 & 0.034 & 0.012 & 0.012 & 0.034 & 0.012 & 0.012 & 0.034 \\
0.014 & 0.018 & 0.014 & 0.021 & 0.014 & 0.017 & 0.021 & 0.018 & 0.014 & 0.017 & 0.021 & 0.018 & 0.017 & 0.021 & 0.018 & 0.017 \\
0.011 & 0.024 & 0.011 & 0.019 & 0.011 & 0.009 & 0.019 & 0.024 & 0.011 & 0.009 & 0.019 & 0.024 & 0.009 & 0.019 & 0.024 & 0.009 \\
0.042 & 0.005 & 0.042 & 0.007 & 0.042 & 0.032 & 0.007 & 0.005 & 0.042 & 0.032 & 0.007 & 0.005 & 0.032 & 0.007 & 0.005 & 0.032 \\
0.015 & 0.004 & 0.015 & 0.025 & 0.015 & 0.042 & 0.025 & 0.004 & 0.015 & 0.042 & 0.025 & 0.004 & 0.042 & 0.025 & 0.004 & 0.042 \\
0.004 & 0.011 & 0.004 & 0.026 & 0.004 & 0.028 & 0.026 & 0.011 & 0.004 & 0.028 & 0.026 & 0.011 & 0.028 & 0.026 & 0.011 & 0.028 \\
0.008 & 0.018 & 0.008 & 0.017 & 0.008 & 0.019 & 0.017 & 0.018 & 0.008 & 0.019 & 0.017 & 0.018 & 0.019 & 0.017 & 0.018 & 0.019 \\
0.01 & 0 & 0.01 & 0.019 & 0.01 & 0.039 & 0.019 & 0 & 0.01 & 0.039 & 0.019 & 0 & 0.039 & 0.019 & 0 & 0.039 \\
0.007 & 0.005 & 0.007 & 0.02 & 0.007 & 0.036 & 0.02 & 0.005 & 0.007 & 0.036 & 0.02 & 0.005 & 0.036 & 0.02 & 0.005 & 0.036 \\
0.001 & 0.003 & 0.001 & 0.023 & 0.001 & 0.032 & 0.023 & 0.003 & 0.001 & 0.032 & 0.023 & 0.003 & 0.032 & 0.023 & 0.003 & 0.032 \\
0.002 & 0.014 & 0.002 & 0.013 & 0.002 & 0.027 & 0.013 & 0.014 & 0.002 & 0.027 & 0.013 & 0.014 & 0.027 & 0.013 & 0.014 & 0.027
\end{bmatrix}.
$$